The Thesis Committee for Jacob Matthew Taylor
Certifies that this is the approved version of the following thesis:

Quantifying Thermally Driven Fracture Geometry during CO_2 Storage

APPROVED BY
SUPERVISING COMMITTEE:

Supervisor:

Steven L. Bryant

Mark W. McClure

Quantifying Thermally Driven Fracture Geometry during CO_2 Storage

By

Jacob Matthew Taylor, B.S.M.E.

Thesis

Presented to the Faculty of the Graduate School of

The University of Texas at Austin

in Partial Fulfillment

of the Requirements

for the Degree of

Master of Science in Engineering

The University of Texas at Austin

December 2014

Acknowledgements

I would like to thank the members of the Geological CO_2 Storage consortium who financially supported my research, and the UTBEG for providing CO_2 sequestration data.

This thesis is the single greatest piece of work I've ever created. This accomplishment was in no small part due to the high caliber of students and faculty at The University of Texas at Austin who motivated me to push the boundaries of my researching skills, and the boundaries of human knowledge. I would specifically like to acknowledge Dr. Steven Bryant for his guidance, brainstorming sessions, and inspiration for this project. He inspired me to strive for excellence and completeness in all aspects of my research, and ultimately this thesis. Thanks to him, no stone was left unturned.

I would also like to thank Dr. Mark McClure for his technical expertise in fracturing mechanics. The devil is in the details, and Dr. McClure made sure I didn't overlook any details.

Finally, I would like to thank my parents for their continual support of my educational endeavors.

Abstract

Quantifying Thermally Driven Fracture Geometry during CO_2 Storage

Jacob Matthew Taylor, M.S.E.

The University of Texas at Austin, 2014

Supervisor: Steven L. Bryant

The desired lifetime for CO_2 injection for sequestration is several decades at a high injection rate (up to 10 bbl/min or 2,400 tons/day per injector). Government regulations and geomechanical design constraints may impose a limit on the injection rate such that, for example, the bottomhole pressure remains less than 90% of the hydraulic fracture pressure. Despite injecting below the critical fracture pressure, fractures can nevertheless initiate and propagate due to a thermoelastic stress reduction caused by cool CO_2 encountering hot reservoir rock.

Here we develop a numerical model to calculate whether mechanical and thermal equilibrium between the injected CO_2 and the reservoir evolves, such that fracture growth ceases. When such a condition exists, the model predicts the corresponding fracture geometry and time to reach that state.

The critical pressure for fracture propagation depends on the thermoelastic stress, a function of rock properties and the temperature difference between the injected fluid

and the reservoir (ΔT). Fractures will propagate as long as the thermoelastic stress and the fluid pressure at the fracture tip exceed a threshold; we calculate the extent of a fracture such that the tip pressure falls below the thermoelastically modified fracture propagation pressure. Fracture growth is strongly dependent upon the formation permeability, the level of injection pressure above fracture propagation pressure, and ΔT.

Table of Contents

List of Tables

List of Figures

Chapter 1: *Introduction*

Anthropogenic carbon dioxide (CO_2) emissions have been studied extensively over the past few decades and have been increasing as the population of the planet grows and more societies industrialize, burning enormous quantities of fossil fuels [8,31]. The result of such a large emission of CO_2 is a widely accepted notion that Earth's climate is changing much more rapidly than natural forces would induce, and in order to preserve a pleasant and productive natural environment for the inhabitants of Earth measures should be taken to reduce the amount of CO_2 released into the atmosphere. One proposed solution is to inject anthropogenic CO_2 into geological formations wherein the CO_2 will become trapped through a variety of mechanisms: "geological (stratigraphic and structural) trapping in depleted oil and gas reservoirs, solubility trapping in reservoir oil and formation water, adsorption trapping in uneconomic coal beds, cavern trapping in salt structures, and by mineral immobilization" [2,6,8].

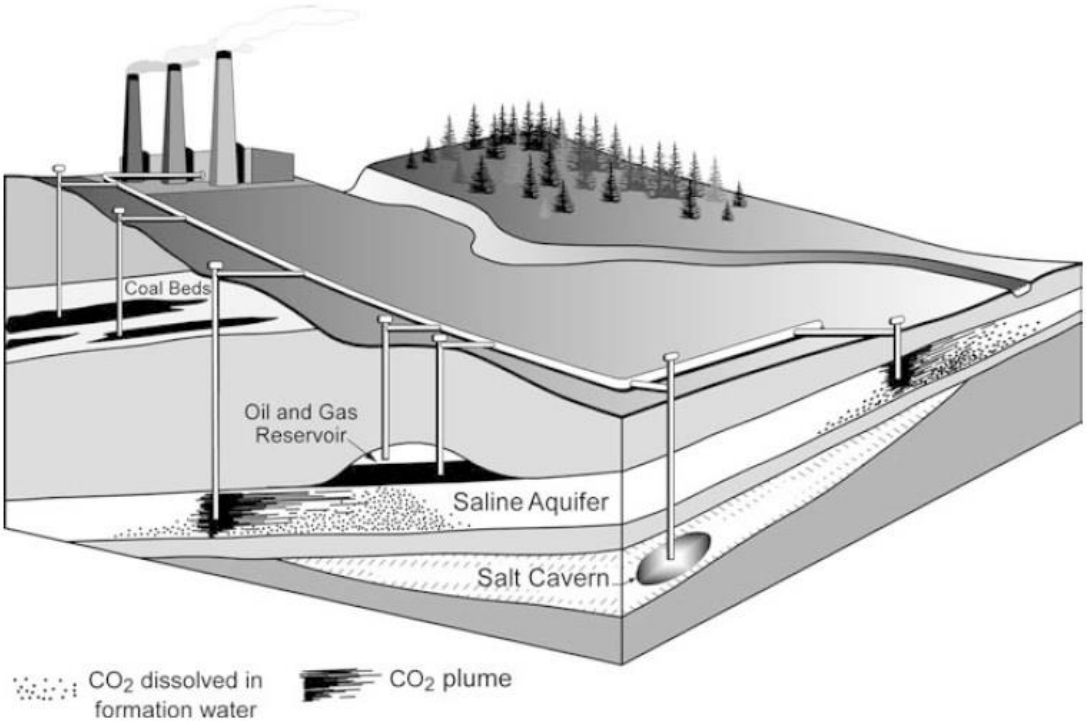

Figure 1: Various CO_2 storage sites and styles [2].

For over a century engineers and scientists within the petroleum industry have studied the geology and behavior of porous media that contain oil and gas with the intent to recover as much of it as possible. The result of this industry's efforts has been a growing familiarity with and ability to characterize subsurface formations and the mechanisms of fluid flow in and out of the sedimentary rocks containing oil, gas, brine, CO_2 and other substances. Given their depth of geologic knowledge, global reach, access to existing infrastructure, dealings in commodities that produce large amounts of CO_2, and technological expertise, geological storage of CO_2 has gained the attention of many within the industry. This attention has led to efforts to fully understand the capacity of

sedimentary basins around the world to act as potential sinks for CO_2, and the natural physical phenomena at work in trapping CO_2 [1,2,6,25]. Figure 1 depicts a variety of subsurface reservoirs that could be used to trap CO_2.

One component of geological CO_2 storage research is predicting and quantifying the geomechanical changes that occur when large volumes of relatively cold CO_2 are injected into hot reservoir rocks- specifically the creation and propagation of fractures and their impact on the containment and injectivity of CO_2 into a storage formation. The need for this research stems from a number of sources: regulatory requirements on safety and containment of CO_2 in reservoirs such that the risk of leakage is minimized, operational requirements that the most economical method of injection of CO_2 be undertaken, i.e. the smallest number of injection wells each having the largest possible injection rate, and geophysical requirements that dictate the suitability of certain rock formations to accept CO_2 at a certain rate and sequester CO_2 for a specified length of time.

The desired lifetime for CO_2 injection for sequestration is several decades at a high injection rate (as much as 10 bbl/min or a few thousand tons/day per injector) to minimize well construction costs. To avoid potential risks to CO_2 confinement, government regulations and geophysical design constraints may impose a limit on the injection pressure and thus on injection rate. For example, the bottomhole pressure may be required to remain less than a prescribed threshold of 90% of the hydraulic fracture pressure of the storage formation. The fracture pressure can be estimated from regional correlations or rules of thumb (e.g. 0.7 psi per foot of depth), or determined readily from

a suitable injection test. Even if this bottomhole pressure constraint is met, some researchers nevertheless expect fractures to initiate and propagate due to the thermoelastic stress reduction on the fracture propagation pressure caused by cool CO_2 encountering hot reservoir rock [26,33]. If this occurs, it is of great interest to know how far the induced fracture might propagate.

1.1 Research Objective

These concerns led to the objectives of this research: to investigate the thermodynamics and fluid mechanics that control injection-induced fracture lengths in rock formations, and then to quantify the thermally driven, two-dimensional geometry of a CO_2 injection-induced fracture where injection is begun below the nominal fracture pressure but above the thermoelastically lowered fracture pressure with the intent to store CO_2 underground (as opposed to well stimulation via hydraulic fracturing). Figure 2 depicts an injection well and the flow path of cold, supercritical CO_2 entering at the wellhead, flowing down the wellbore picking up heat from the Earth, entering the storage formation at the perforations a slightly warmer temperature, and then inducing a thermoelastic fracture because the fluid temperature is significantly lower than the formation temperature, a difference on the order of 40 Kelvin or more. CO_2 will then travel down the length of the fracture, flowing out into the reservoir from the faces of the fracture, causing convection of cold fluid into the reservoir while the geothermal energy conducts into the CO_2. The fracture propagates due to the induced thermoelastic stress reduction on the minimum horizontal Earth stress.

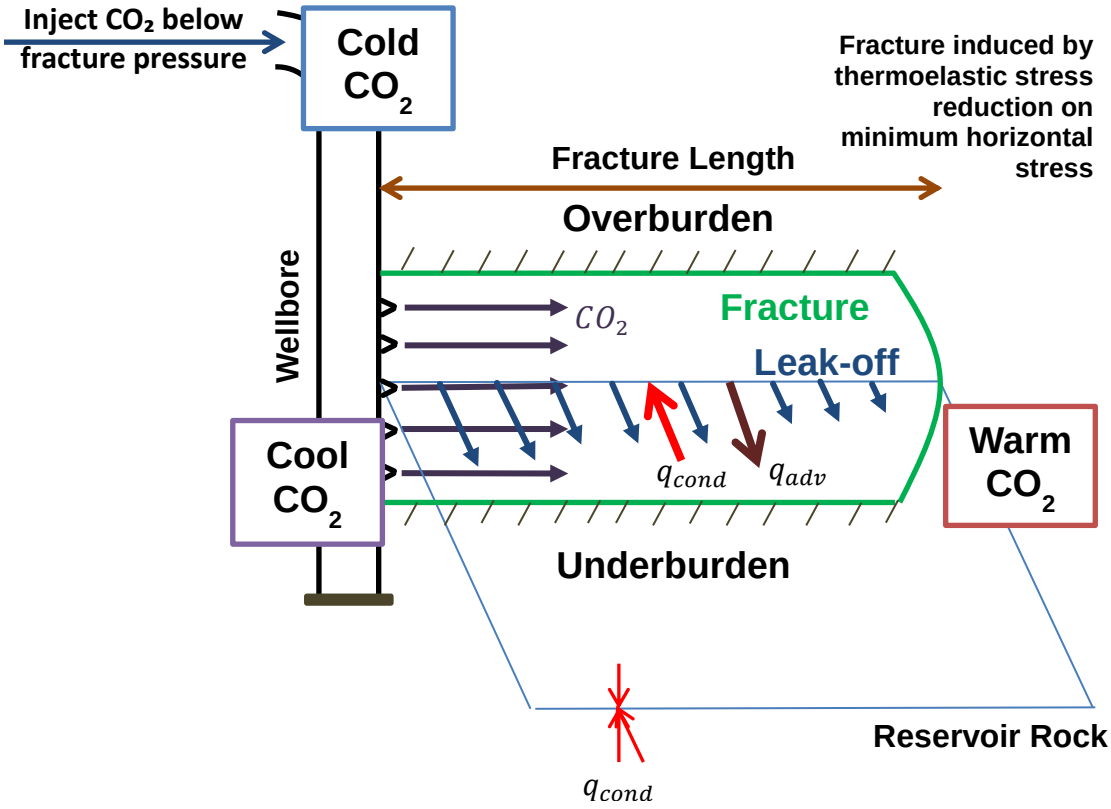

Figure 2: Diagram of injection scenario, with fracture growth mechanisms.

The induced thermoelastic stress is proportional to the difference in temperature (ΔT) between the CO_2 and the rock. The fracture may be self-limiting because of the warming of the CO_2 by conduction from the surrounding formation as it flows along an induced fracture, and the large but finite conductivity of such fractures which reduces the internal pressure. Knowing final fracture geometry is useful because:

- Fractures may intersect other existing wells in the formation resulting in additional potential escape routes for the CO_2,
- Fractures provide a relative "superhighway" for CO_2, influencing plume migration and storage efficiency, and
- Fractures increase the injectivity of the well, and hence influence the economics of the storage program.

In this thesis a numerical model was developed that will enable operators to calculate whether the injection-induced fracture stabilizes at mechanical and thermal equilibrium such that fracture growth ceases, and when such a condition exists, what the fracture geometry will be and how long it takes to reach that state. The model also enables operators to estimate injection pressures that would keep the induced fracture within a prescribed "area of review" around an injection well, and provides an estimate of the possible injection rate given the properties of the reservoir.

1.2 Details on Current and Historic CO_2 Storage Programs

Few true sequestration sites exist around the world, but some well-known CO_2 injection sites were developed to meet governmental emissions requirements associated with hydrocarbon production (Sleipner, Norway), as sequestration pilot programs (In Salah, Algeria; Cranfield, MS; Frio, TX; see Figures 3 and 4), to use in enhanced oil recovery (West Texas), or as a corollary to acid gas disposal (Alberta, Canada) [2,14,28]. Examples of overall injection rates by field are 2700 tons/day at Sleipner, 3500 tons/day at In Salah, 2700 tons/day at Cranfield, and a prospective 12300 tons/day in the Gorgon LNG project in Australia [28]. These and other long-term injection programs have proven the technology exists for CO_2 sequestration. Thinking ahead, some researchers have identified and characterized other reservoirs that have high potential to act as storage sites [2,6,25]. Key storage-reservoir parameters are permeability, porosity, depth and pore pressure, fluid in place, lithology and mineralogy, geometry, heterogeneity, and geomechanical properties of both the storage reservoir and the boundary layers. Risk assessment of CO_2 containment for each storage site needs to be performed on the

formations, the wells and well cement used to channel CO_2 into the formations. The long-term fate of the CO_2 as it travels through the reservoir needs further study to determine flow paths, reactions with minerals in the rocks, and possible dissolution in the formation oil, gas or brine.

Due to the economic feasibility of EOR programs and the current lack of government incentives to inject CO_2 purely for sequestration, injection will likely occur first (and historically has been) in depleted oil and gas reservoirs as a tertiary recovery mechanism before aquifers are targeted [14,25]. However, according to studies conducted by the IPCC in 2005, USDOE in 2007, Bradshaw et al. in 2007 and others, aquifers have some of the highest capacity for CO_2 storage. Aquifer storage however presents some unique challenges that require further study to maximize their potential capacity, namely scaling up pilot programs to multiwell, commercial-scale, many megatons per year of CO_2 injection [28]. Locations identified around the world for potential aquifer storage are depicted in Figure 3. With the objective to maximize rates and injected volumes for sequestration comes the risk of fracturing the reservoir rock, the mechanisms and result of which demands further investigation.

Figure 3: Map of saline aquifer and EOR CO_2 injection sites as of 2010 [28].

1.2.1 Reservoir Characteristics

The specific reservoir rock properties needed for geo-thermo-mechanical study include density, porosity, permeability, thermal conductivity, coefficient of thermal expansion, heat capacity, and the mechanical rock properties of Young's modulus, Poisson's ratio, coefficient of thermal expansion and the coefficient of poroelasticity of brine filled rocks [24,28,45,46]. The rock properties used in this work were based on generic, hypothetical sandstones, with some influence from the Cranfield Field CO_2 storage pilot program in an attempt to 1) predict the possibility of fracture growth in that specific field, and 2) determine realistic fracture sizes through the use of real rock and fluid properties. Typical storage reservoirs are expected to be on the order of 1 to 1000 mD permeability, 10 – 40 % porosity, 30 to 130 degrees Celsius, and 10 to 30 MPa of

pressure [2,24,28]. Figure 4 contains properties of different storage reservoirs around the world.

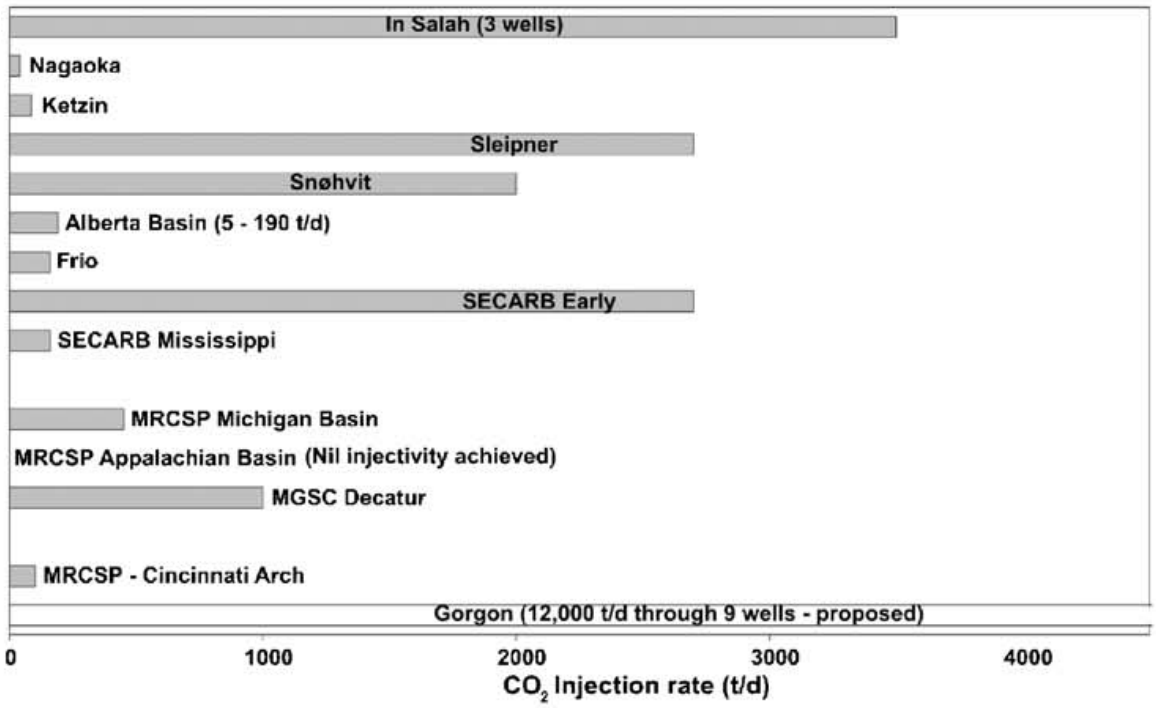

Figure 4

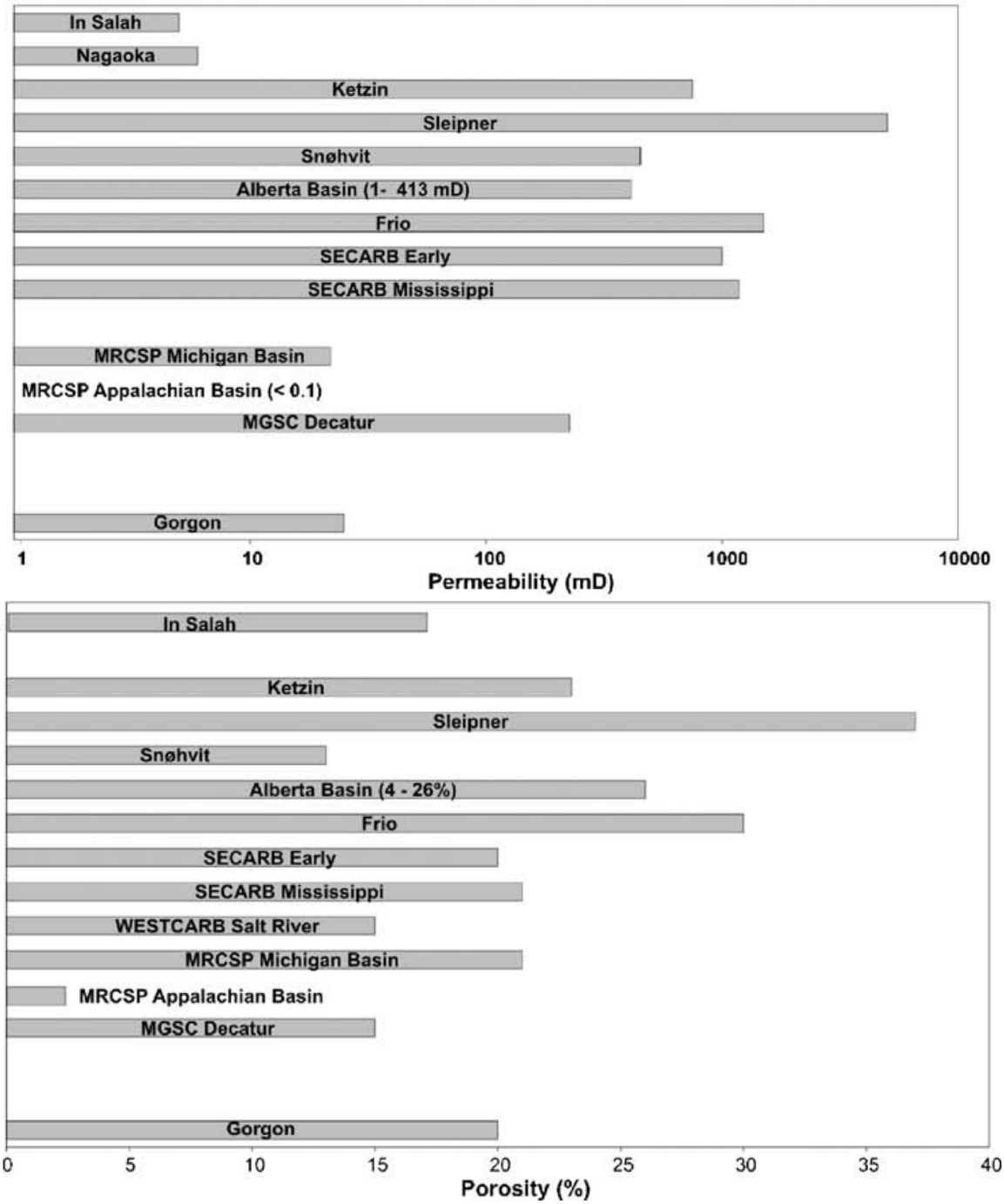

Figure 4, cont.: Characteristics of CO_2 geological storage operations in saline aquifers [2].

The thermal properties of storage reservoirs, which have typically been sandstones, are also highly important in CO_2 sequestration and in this work because they

affect the magnitude and longevity of the thermoelastic stress effect. The rate of geothermal conduction is also a function of these properties. Somerton's thermal experiments provided typical values of thermal conductivity, heat capacity, thermal diffusivity and coefficient of thermal expansion of sandstones, as shown in Figures 5 and 6.

TABLE 3—CALCULATED HEAT CAPACITIES OF FLUID-SATURATED ROCKS
(Heat Capacity at 620°F and Pressure Indicated—Btu/cu ft/°F)

	14.7 Psia			500 Psia		1,500 Psia		3,000 Psia	
Sample	Dry	Methane	Water	Methane	Water	Methane	Water	Methane	Water
1—Sandstone	34.0	34.0	34.0	34.1	34.1	34.3	34.9	34.6	45.9
2—Sandstone	32.9	32.9	32.9	33.0	33.0	33.3	34.0	33.7	47.6
3—Silty Sand	35.6	35.6	35.6	35.7	35.7	36.0	36.5	36.3	49.1
4—Silty Sand	33.5	33.5	33.5	33.5	33.6	33.9	34.5	34.3	48.3
5—Siltstone	32.0	32.0	32.0	32.1	32.1	32.5	33.2	32.9	48.7
6—Siltstone	33.6	33.6	33.6	33.7	33.7	34.0	34.6	34.3	47.7
7—Shale	39.6	39.6	39.6	39.6	39.6	39.7	40.0	39.9	40.1
8—Limestone	35.4	35.4	35.4	35.5	35.5	35.7	36.2	36.0	46.8

TABLE 4—MEASURED THERMAL CONDUCTIVITIES AT 90°F
(Thermal Conductivity—Btu/Hr sq ft °F/Ft)

Sample	Porosity	Air	Oil[1]	Water[2]	Oil and Water[3]
1—Sandstone	0.196	0.507	0.787	1.592	1.425
2—Sandstone[4]	0.40	0.285	0.577	1.050	.....
3—Silty Sand[4]	0.40	0.285	.....	.....	.....
4—Silty Sand[4]	0.43	0.261	0.625	1.110	.....
5—Siltstone[4]	0.36	0.338	0.553	1.036	.....
6—Siltstone	0.199	0.396		Core Damaged	
7—Shale	0.071	0.603	.....	0.975	.....
8—Limestone	0.186	0.983	1.245	2.050	1.690
9—Sand (Fine)	0.38	0.362	(0.80)	1.590	.....
Run 2	0.38	0.345	.....	.....	.....
10—Sand (Coarse)	0.34	0.322	0.950	1.775	.....
Run 2	0.34	0.323	.....	.....	.....

[1]Light lubricating oil, $k_2 = 0.077$
[2]Distilled water, $k_2 = 0.353$
[3]Approximately 35 per cent water—65 per cent oil
[4]Disaggregated samples

Figure 5: Thermal properties of various rock types [46].

TABLE 6—CALCULATED THERMAL DIFFUSIVITIES

Sample	Bulk Density (lb/cu ft)		Heat Capacity (Btu/lb/°F)		Thermal Conductivity (Btu/hr sq ft °F/ft)		Thermal Diffusivity (sq ft/hr)	
	Air	Water	Air	Water	Air	Water	Air	Water
1—Sandstone	130	142	0.183	0.252	0.507	1.592	0.0213	0.0445
2—Sandstone	90	115	0.200	0.374	0.285	1.050	0.0158	0.0244
(Original)	109	126	0.200	0.308	(0.34)*	(1.32)	(0.0156)	(0.0340)
3—Silty Sand	90	115	0.202	0.376	0.285	(1.05)	0.0157	(0.0242)
(Original)	119	132	0.202	0.288	(0.40)	(1.50)	(0.0167)	(0.0394)
4—Silty Sand	85	112	0.200	0.393	0.261	1.110	0.0153	0.0249
(Original)	116	130	0.200	0.286	(0.47)	(1.51)	(0.0202)	(0.0406)
5—Siltstone	96	118	0.202	0.351	0.338	1.036	0.0174	0.0250
(Original)	105	123	0.202	0.318	(0.44)	(1.29)	(0.0207)	(0.0329)
6—Siltstone	120	132	0.204	0.276	0.396	(1.51)	0.0162	(0.0414)
7—Shale	145	149	0.192	0.213	0.603	0.975	0.0216	0.0307
8—Limestone	137	149	0.202	0.266	0.983	2.050	0.0355	0.0517
9—Sand (Fine)	102	126	0.183	0.339	0.362	1.590	0.0194	0.0372
10—Sand (Coarse)	109	130	0.183	0.315	0.322	1.775	0.0161	0.0433

*Values in parentheses estimated

Figure 6: More thermal properties of various rock types [46].

The contribution from the geothermal heat flux that controls the temperature of static reservoirs, and that would apply heat to fluids injected into the subsurface, is another parameter that needs to be included in a geo-thermo-mechanical model. From Pollack et al.'s 1993 study of thousands of sites around the globe, the heat flux from the Earth's core spherically outward as measured very near the Earth's surface was found to be on the order of 0.1 W/m^2 [35]. Integrated across the entire surface of the Earth this geological heat flow is quite large, but on a local reservoir scale, as will be discussed in later chapters, advection of cold fluids flowing through a reservoir completely dominates this conduction such that its contribution is negligible to the scenarios studied herein. This is one important finding. If geothermal flux were large enough to warm the CO_2 appreciably as it flows along the fracture, then the heat flux could prevent the thermoelastic effect entirely and thereby suppress the risks associated with injection-induced fracture propagation. Heat transport may be convection dominated at sufficiently

high injection rates which then leads to the research question: does the fracture ever stop propagating since the cool injected fluid can flow through the fracture without being warmed by conduction?

1.2.2 Fluid Characteristics of CO_2 Storage

In order to inject CO_2 most economically, high injection rates transporting dense, supercritical CO_2 need to be maintained. Therefore understanding the phase behavior of CO_2 as it exists in a pipeline traveling to a wellhead, warming as it travels through a wellbore to the perforations, and then the phase changes occurring as it travels down a fracture and into a reservoir are important considerations when designing a sequestration program. Previous work has provided methods to calculate the bottomhole temperature of CO_2 or other injected fluid as it travels down the wellbore, provided data of the wellhead temperature and pressure, geothermal gradients, and heat transfer parameters of the well casing and surrounding Earth [18,26]. Figure 7 depicts two regions of interest in heat transfer study of injected fluids: prior work and the focus of this thesis.

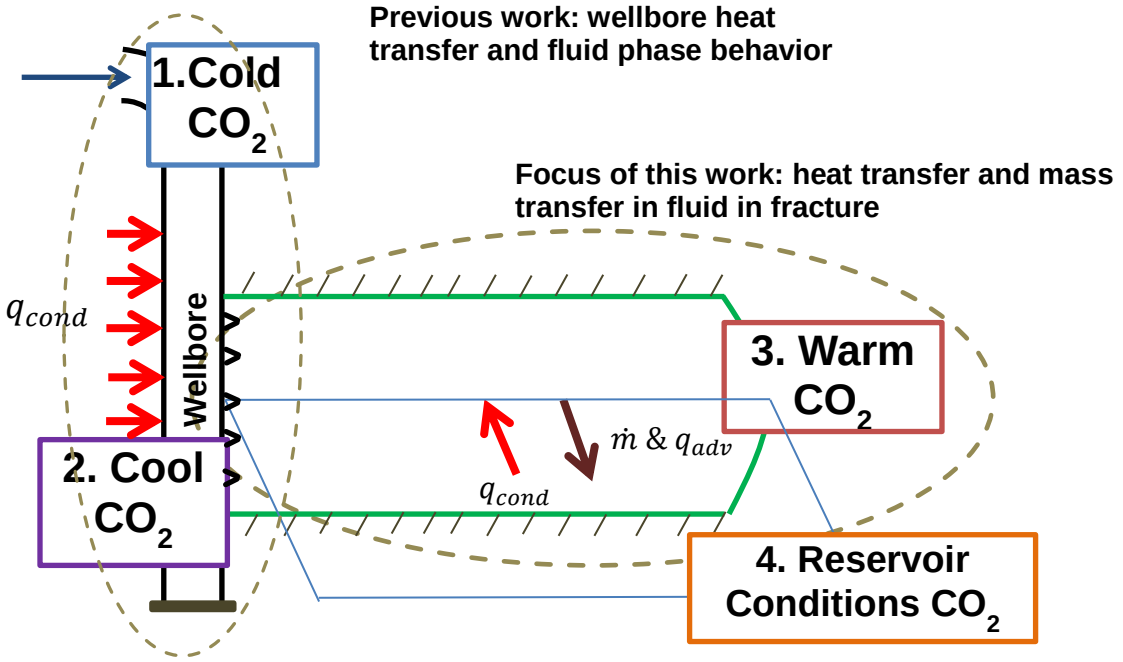

Figure 7: Diagram of two areas of focus in heat transfer research for thermoelastic fracture propagation: from point 1 to 2, and from point 2 to 3.

Other measured injection conditions from pilot storage programs provide typical wellhead and bottomhole temperature and pressure which can be used in modeling CO_2 injection. Due to the low heat capacity and high compressibility of CO_2, thermal expansion effects as the CO_2 warms as it travels along the fracture and out into the reservoir may have a significant impact on pressure gradients inside a fracture. The change in density of CO_2 is shown in Figure 8 from a typical state entering a storage reservoir at the perforations (point 2 in Figure 7) to the state at expected deep in the reservoir (point 4 in Figure 7). Heat transfer rates between a reservoir and the cold injected fluid will also be significant due to the large initial temperature difference. At least a 30% change in density is possible. Additionally, and what was discovered to have a larger impact on fracture length than the density change, the viscosity of injected CO_2

may also decrease by 30% or more from injection conditions to reservoir conditions. The intent of this thesis was to account for the phase behavior of the injected fluid and determine the contribution of viscosity and density changes to injection-induced fracture propagation.

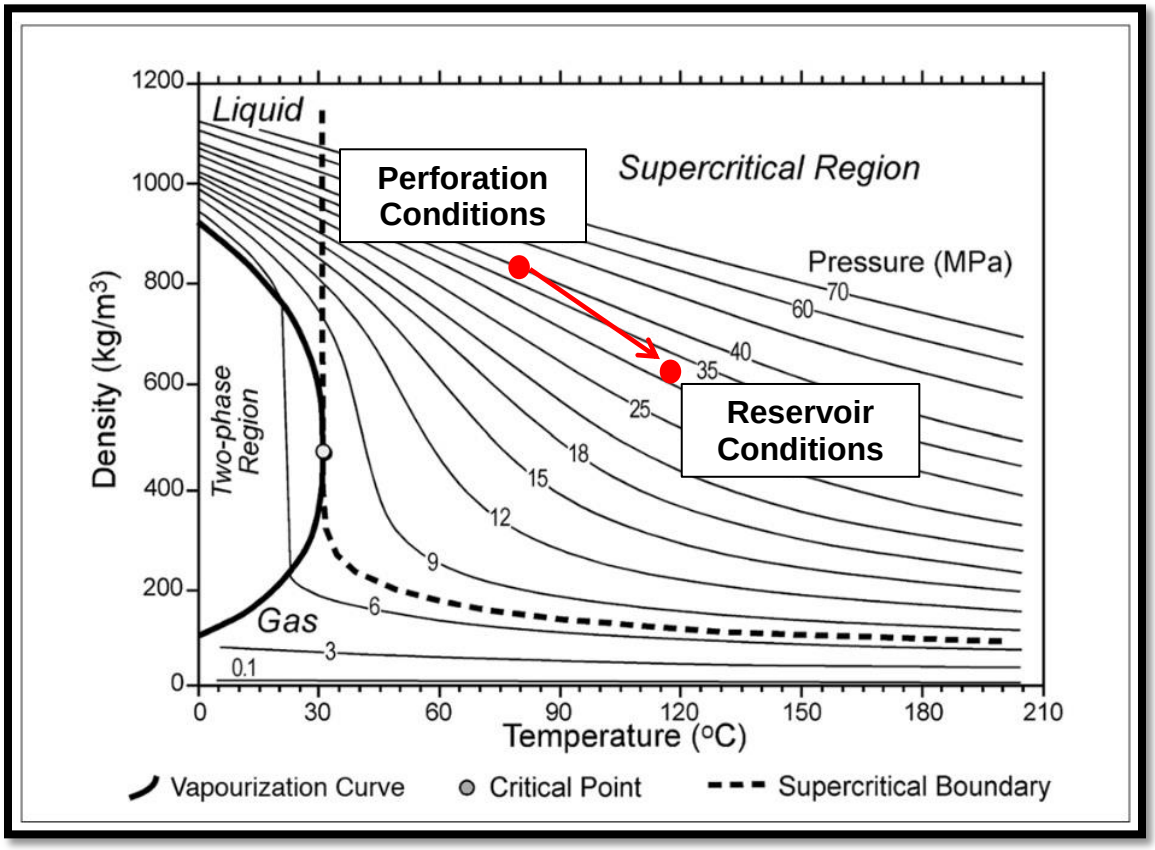

Figure 8: CO_2 phase behavior chart showing the change from typical injection to reservoir conditions. The injected fluid is expected to remain in the supercritical state from wellhead to reservoir conditions, but due to warming and depressurization the density change will be significant [2].

To date the geomechanical effects of supercritical CO_2 injected at over 1000 tons/day for many years into a saline aquifer have not been widely monitored or investigated. However an analogous problem that has garnered attention in industry and

the research community is secondary or tertiary recovery of oil in depleted reservoirs through waterflooding.

1.3 Evidence of Thermoelastic Fracture Propagation in Waterflooding of Oil Reservoirs

Anecdotal evidence from field studies of waterflooding has demonstrated the ability for fractures to be unintentionally initiated at injection wells (i.e. injection was managed so that injection pressures were held below nominal fracture pressures) and for to intersect production wells resulting in a dramatically early water breakthrough [9,11,20,29,49]. Some believe that nearly all waterflooded reservoirs have been fractured due to pore-plugging caused by particulates and oil drops carried by the injected water, poorly characterized geomechanical properties and Earth stresses in reservoirs, thermoelastic stresses, and the general lack of attention given to the science of geo-thermo-mechanics [49]. In all waterflooding scenarios, and of high likelihood in CO_2 sequestration scenarios, multiple injectors and producers will exist in a single continuous reservoir which leads to the risk of an induced fracture propagating from one well to another. Once these fractures are created, a high permeability pathway will link the two wells even if the injection pressure is reduced so the fractures close. This is due to the low likelihood the fracture walls reset against each other in exactly the same orientation as before fracturing. Instead, asperities on the surface of the fracture walls are likely to hold the walls apart and thereby maintain a conduit of higher permeability. Such fractures could ruin the sweep efficiency of the waterflood or the storage capacity of a sequestration reservoir due to the preferential flow path that exists in the fracture. The

nature and physics of the creation, propagation and ultimately the final geometry of thermoelastic fractures are thus important to engineers and operators of CO_2 sequestration sites, waterflooding sites, or any other site where fluids are injected into a reservoir of a different temperature.

Luo and Bryant (2013) developed a heat transfer model to determine the temperature of CO_2 at the perforations of an injector. With this model, they concluded there is a high likelihood of a thermoelastic stress effect to exist once the fluid enters the formation. The two options for operators concerned about fractures are: 1) pump at very low rates such that the fluid warms to close to reservoir temperature by the time it reaches the perforations eliminating the thermoelastic stress, or 2) allow fractures to form and attain much higher injection rates. The consequences of allowing fractures to form were studied, and their severities are a function of their geometry. Therefore, quantifying their geometry is crucial to understanding the risks they pose to CO_2 sequestration and is the focus of this thesis.

Chapter 2: *Porous Media Fracturing Principles*

2.1 Classical Hydraulic Fracturing Theory

Basic geomechanical theory states that all subsurface rock formations at any appreciable depth are in a state of compression as specified by three principal stress magnitudes and orientations [54]. Most often the vertical principal stress is the largest of the three and is equal to the summation of the forces exerted by all the layers of rock above a target formation. The two horizontal principal stresses are usually not equal due to a prevailing tectonic movement or anisotropic rock material properties. Tectonic forces do not allow for horizontally isotropic elastic deformation of the target formation, meaning the two horizontal principal stresses are most often not equal and fractures will propagate in the direction of maximum horizontal stress, i.e. they will open against the minimum horizontal stress. See Figure 9 for a diagram of the stress state.

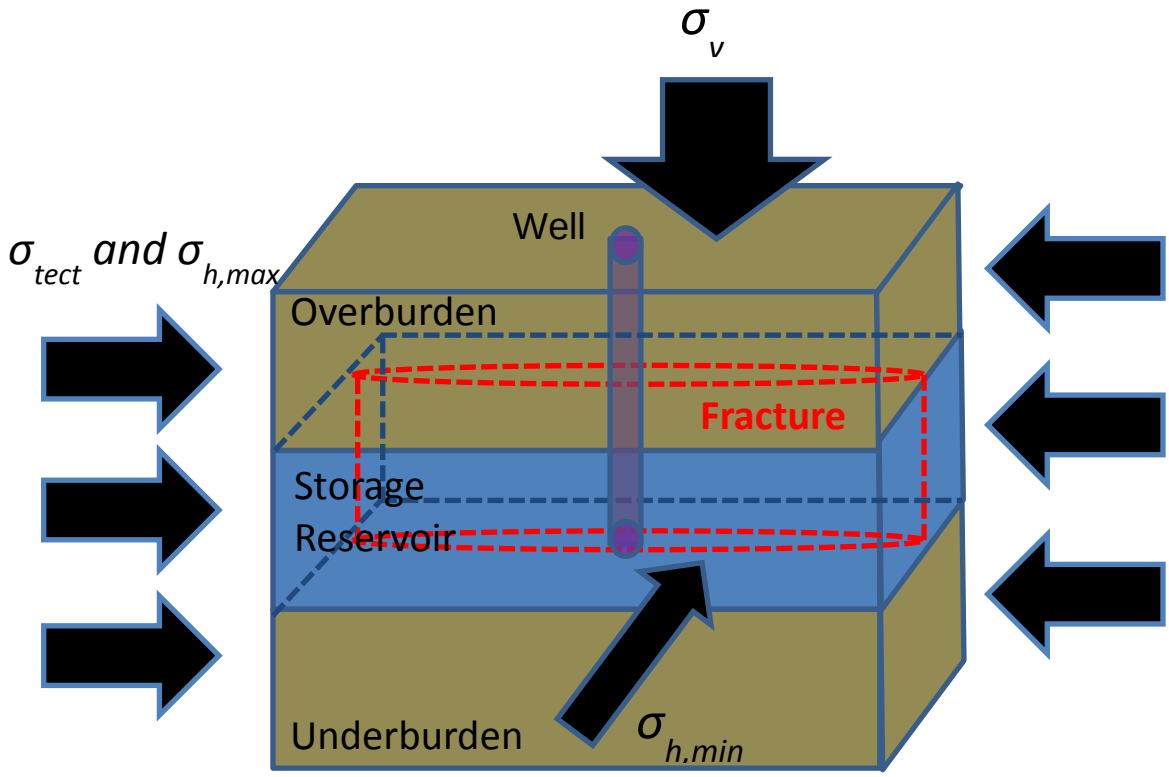

Figure 9: Diagram of the stress state in the subsurface. Fracture propagation is most often observed where the fracture opens against the minimum horizontal stress ($\sigma_{h,min}$) and propagates parallel to the maximum horizontal stress ($\sigma_{h,max}$). The vertical principal stress is typically the largest stress at any appreciable depth.

The industry-standard method for calculating the vertical principal stress (σ_v) is to integrate a density log (ρ, as function of depth) from the surface to the depth of interest, Z [5,23].

$$\sigma_v = \int_0^Z \rho g dZ \tag{1}$$

The minimum horizontal principal stress can be calculated from the following equation derived from linear poroelasticity theory [5,12,15]:

$$\sigma_{h,min} = \frac{\nu}{1-\nu}\left(\sigma_v - \alpha_p p\right) + \alpha_p p + \sigma_{tect} \tag{2}$$

Poisson's ratio, v, can be estimated from acoustic logs, p- the fluid pressure in the storage reservoir- must be measured with a bottomhole pressure gauge or estimated from a hydrostatic gradient, and α_p is the linear-elastic material property of the reservoir rock called Biot's coefficient of poroelasticity. It is usually unity but can vary from zero to one [12].

In certain tectonically neutral areas the σ_{tect} term may be zero, but a common oilfield practice is to perform an injection test to determine the actual minimum horizontal stress and then compare the poroelastic theoretical stress to the measured value to find the tectonic stress [5,27,53]. This provides a much more accurate quantification of the minimum principal stress. Equation 2 is critical for this work because it establishes the threshold fluid pressure p_{thresh} necessary to propagate a fracture, namely p_{thresh} equal to $\sigma_{h,min}$.

Poisson's ratio is defined as "the ratio of lateral expansion to longitudinal contraction for a rock under a uniaxial stress condition" [15]. It is common for vertically adjacent layers to exhibit different Poisson's ratios and therefore different minimum horizontal stress values. The difference in this linear-elastic material property is due to the microstructural and compositional variation between the rock layers. Stress contrasts from layer to layer can be as large as 1000 psi or 7 MPa (see Figure 10). This phenomenon is important in selecting storage reservoirs, and in predicting fracture height, as a minimum horizontal stress contrast between adjacent reservoirs can pose as a barrier to fracture height growth. Shales typically have a Poisson's ratio between 0.3 to 0.45 and sandstones have a value between 0.1 to 0.2. Higher Poisson's ratios result in

higher $\sigma_{h,min}$ (see Equation 2) meaning the fracture pressure in shale is typically higher than in sandstone storage reservoirs. Constant height fractures will be a simplifying assumption in calculating the geometry of thermoelastic fractures in this thesis, and is also a common assumption in classical hydraulic fracture theory which will be discussed in more detail later.

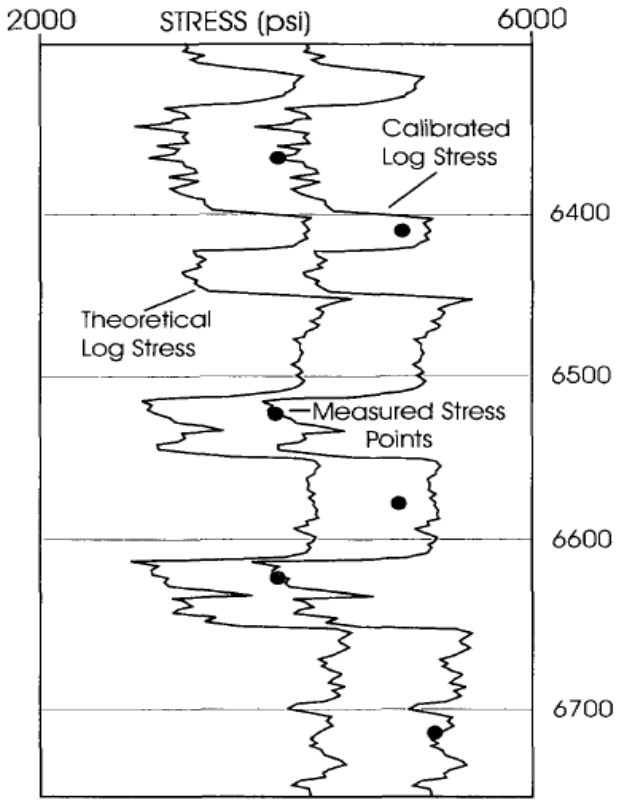

Figure 10: "Well log calculated stress profile from sonic and density data compared with stress-test measurement points. A calibrated curve is then obtained by shifting the theoretical curve to match stress tests" [21]. The shift corresponds to the addition of tectonic forces to the theoretical minimum horizontal stress calculated from Equation 2. This log highlights the value in obtaining real stress values from an injection test. The intervals of larger and smaller stress correspond to layers of shale and sandstone respectively.

Hydraulic fractures are able to initiate and propagate once the minimum horizontal principal stress is surpassed by injecting a fluid at high pressure into the rock matrix. Fracture initiation may require a higher injection pressure than fracture propagation due to the tensile strength of the rock. Once the fracture has grown more than one meter rock strength is negligible and a sufficient condition for fracture propagation is that the fluid pressure inside the fracture exceeds the minimum horizontal stress [17,30,34,54].

Once the trend of minimum horizontal stress versus depth is known (as in Figure 10, for example), fracture propagation can be predicted using the theory of a linearly elastic porous media. The classical theory of hydraulic fracturing has largely been divided into two methodologies based on two-dimensional (2D) assumptions: those developed by Perkins and Kern (1961) and then refined by Nordgren (1972) known as the PKN model, and the methods developed by Khristianovich and Zheltov (1955) later refined by Geertsma and de Klerk (1969) which is known as the KGD model. Both models seek to solve both the fluid flow problem in the fracture and the fracture mechanics problem of a porous elastic solid, but their main disagreement is the assumption regarding the direction of plane strain in the media resulting in different theoretical cross-sectional shape of the fracture. The PKN method assumes a vertical ellipse cross-section (Figure 11), and KGD assumes a horizontal ellipse cross-section (Figure 12). Both theories are based on the work done by Sneddon (1946) [43,44].

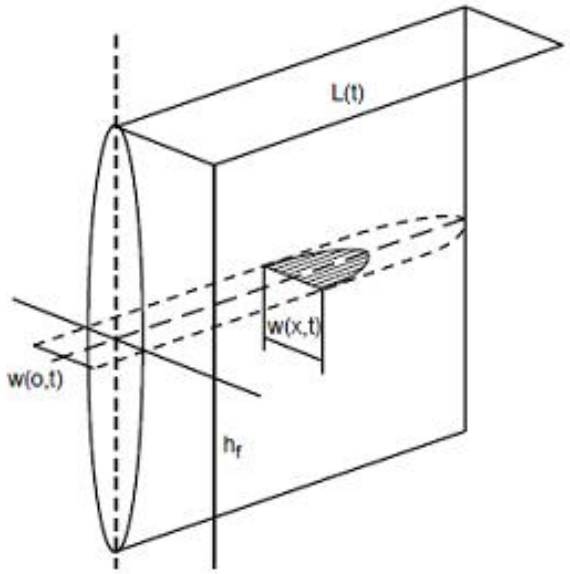

Figure 11: PKN-type fracture shape [13].

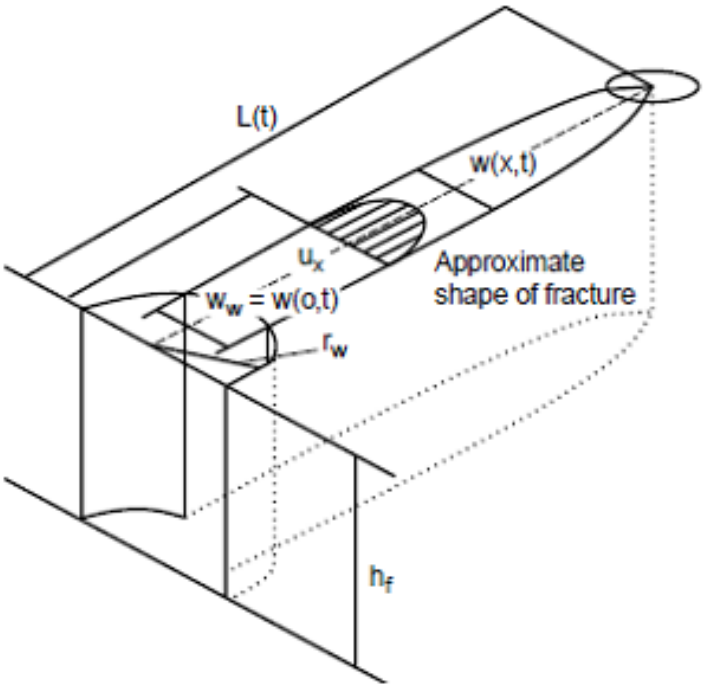

Figure 12: KGD-type fracture shape [13].

The PKN fracture methodology has widely been accepted as better at representing long, height-constrained fractures while the KGD model has been used to describe fractures where their height is much greater than length. These 2D fracture models are used in many numerical fracturing simulators, incorporating numerous tweaks and additions. Analytical solutions have been derived for fracture length and width with prescribed height and injection pressure. The main criterion for propagation is the tip pressure in the fracture must exceed $\sigma_{h,min}$, and the main components of final fracture geometry are length, width, height, and cross-sectional shape which can be estimated by the following equations from the PKN model [30,33]:

$$L(t) = \frac{q_i t^{0.5}}{\pi C h} \tag{3}$$

$$W(0,t) = 4\left[\frac{2(1-\nu)\mu q_i^2}{\pi^3 G C h}\right]^{0.25} t^{0.125} \tag{4.1}$$

$$w_y(z) = \frac{2(1-\nu)}{G}\Delta P h\left(1-\frac{z^2}{h^2}\right)^{1/2} \tag{4.2}$$

$$p_{frac} = \sigma_{h,min} + \sqrt{\frac{\pi U E}{(1-\nu^2)h}} \tag{5}$$

L is the fracture length at time t of pumping, q_i is a constant flow rate into a fracture, h is the height of the fracture, C is the fluid loss coefficient, μ is the fluid viscosity, ν is Poisson's ratio, G is the bulk shear modulus of the formation rock, U is the rock specific surface energy, E is Young's modulus, and W is the maximum fracture width at the wellbore (Equation 4.1). In Equation 4.2, h is the half-height of the fracture, z is the position from the fracture center to the top of the fracture (from zero to h), ΔP is the net pressure (pressure inside the fracture minus $\sigma_{h,min}$), and w_y is the half-width of the fracture

as a function of the position *z*. One sees that length and width are then coupled and vary with pumping time. The PKN model assumes an elliptical cross-sectional shape as seen in Figure 11, and constant, prescribed height.

Equation 4.2 is the analytical solution for the relative normal displacement distribution along a crack (i.e. the half-width of an elliptical cross-section crack of half-height *h*) which is the Sneddon solution for a crack in an infinitely sized elastic material. ΔP is the net pressure between the internal crack pressure and opposing stress and *z* is the vertical position within the crack. Both the PKN and KGD models were built on this solution, but the direction of the ellipse aperture was chosen perpendicular to one another based on assumptions these researchers used. In this work, the PKN method was used, but fracture width was assumed constant; this allows restricting the mathematical domain to two dimensions. Therefore, a representative width can be calculated from Equation 4.2. Work in three dimensions would require a model with varying fracture aperture as a function of height and length.

One final characteristic of a hydraulic fracture of great interest to oilfield operators is the permeability, transmissivity, or conductivity of the conduit. One industry method of estimating a fracture's permeability via a parallel plate-type approximation is to use Equation 6 [5,13,15]. Estimating the width of a fracture via Equation 4.2 and assuming that an injection-induced fracture would have walls completely out of contact, a reasonable estimate of fracture permeability can be obtained via Equation 6.

$$k_f = \frac{w^2}{12} \tag{6}$$

Prats (1961) developed a correlation for dimensionless fracture conductivity (what he called the *"relative capacity*", *a*) relating the formation permeability *k*, length X_f of one wing of a bi-wing fracture, fracture permeability k_f, and fracture width *w*:

$$a = \frac{\pi k X_f}{2 k_f w} \tag{7}$$

Thus, with knowledge of the fracture geometry and a pressure transient test of the target reservoir providing formation and fracture permeability, it is possible to determine *relative capacity*, and therefore the dimensionless conductivity of the fracture [22,36].

The *relative capacity* of a fracture approaches zero for an infinitely conductive fracture and infinity for a reservoir with a very small fracture (width goes to zero and fracture permeability approaches formation permeability). Infinitely conductive fractures are assumed to have uniform pressure everywhere within the fracture. Finitely conductive fractures have a pressure gradient that is thus a function of the formation permeability and fracture permeability, which Prats demonstrated, as shown in Figure 13. The work described in this thesis will test the accuracy of this correlation for high permeability fractures in high permeability reservoirs, i.e. reservoirs likely to be used for geologic CO_2 storage.

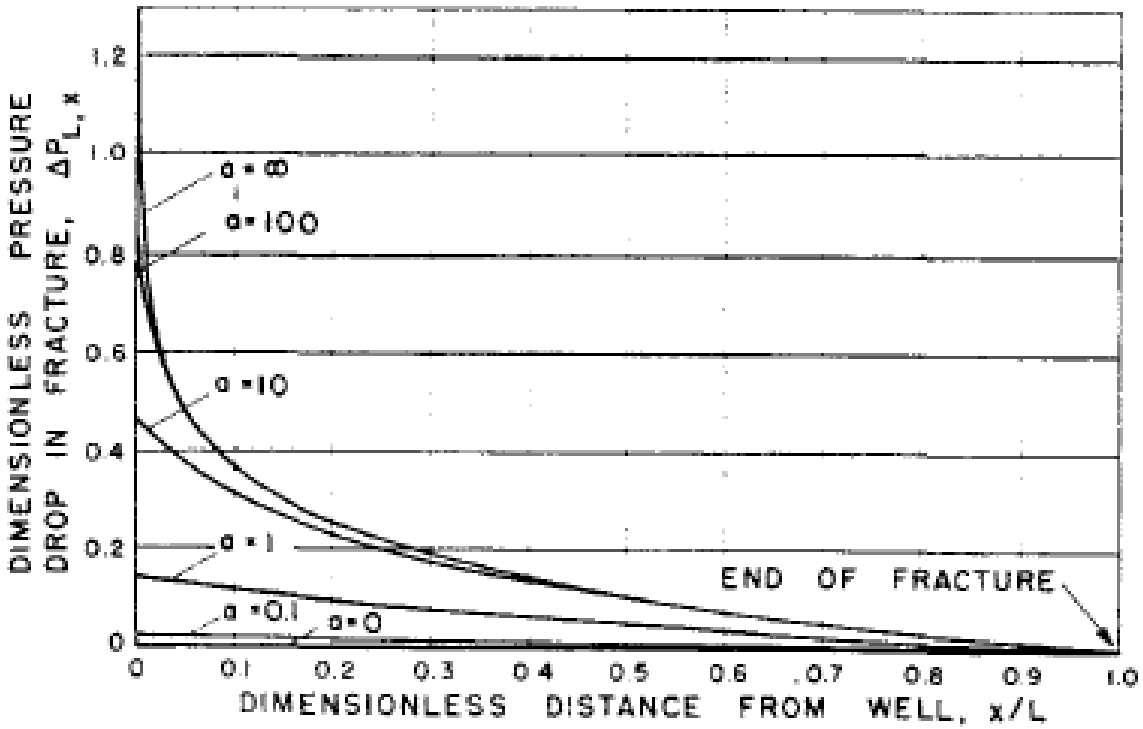

Figure 13: Graph of the dimensionless pressure-drop distribution in a fracture as function of dimensionless distance from the well. The dimensionless pressure drop is the pressure at a point along the fracture minus the tip pressure, normalized by the difference in pressure between wellbore and tip. Here the dimensionless pressure-drop is plotted for a variety of relative capacities, *a* [36]. When the relative capacity is very low, the pressure along the fracture is nearly uniform.

Other major assumptions of the PKN model are constant Earth stresses acting upon the fracture, incompressible, constant-property fluids, one-dimensional (1D) flow down the fracture with no pressure variance in the vertical direction (nor in the horizontal direction transverse to flow), and a constant leak-off coefficient that describes fluid loss from a fracture into the formation, independent of the changing internal pressure.

The leak-off coefficient model to describe fluid loss from a fracture face as it propagates was introduced by Howard and Fast in 1957 [19]. In this work, Carter derived

a correlation between the net pressure (difference between the pressure in the fracture and initial reservoir pressure), porosity, permeability, and viscosity and the linear rate of fluid loss from a fracture face. The three components of the Carter leak-off coefficient describe three layers of resistance to flow: a viscous bank (C_I), reservoir fluid flow and compressibility (C_{II}), and filtercake (C_{III}).

$$C_I\left(\frac{ft}{\sqrt{min}}\right) = 0.0015\sqrt{\frac{k_r \Delta P \emptyset}{\mu_f}} \tag{8}$$

$$C_{II}\left(\frac{ft}{\sqrt{min}}\right) = 0.0012\Delta P\sqrt{\frac{k c_t \emptyset}{\mu}} \tag{9}$$

C_{III} must be determined through laboratory experimentation with expected filtercake properties built-up inside a fracture. The variables are φ for porosity, k_r for relative permeability of the formation to the invading fluid, k for permeability of the formation to in-situ fluids, ΔP for the net pressure, μ for the viscosity of the in-situ fluid and μ_f for the viscosity of the invading fluid [19,42]. These leak-off coefficients are usually determined through field injection tests performed prior to hydraulic stimulation. To calculate the total leak-off rate from a fracture for use in estimating final fracture geometry, these three coefficients are summed (to C_T) and total leak-off rate (Q_l) is calculated at time t of a propagating fracture by [19,51]:

$$Q_l(t) = 4h * C_T \int_0^{L(t)} \frac{dx}{\sqrt{t-\tau(x)}} \tag{10}$$

wherein h is fracture height, L is the half-length of the fracture, $\tau(x)$ is the time of exposure position x has to the injected fluid. While this theory works well for hydraulic fracturing, this relation only works if the fracture propagation rate is much larger than the

leak-off rate, the fracture is infinitely conductive, and the leak-off rate is not primarily dominated by reservoir flow [27,42,51]. None of these conditions apply in the case of long term injection of low viscosity fluid (e.g. CO_2) into high permeability reservoirs [42,51]. In other words, classical leak-off models are unlikely to be applicable to injection-induced fractures in geological CO_2 storage.

Given the known limitations of the Carter leak-off model, others have attempted to derive formulae for 2D, nonlinear, elliptical, radial, transient or other variations of fracture fluid loss [16,40,50]. Due to the transient nature of pressure gradients in propagating fractures, closed-form solutions are not readily available or are cumbersome to use, thus numerical solutions appear to be the best solution to calculate true Darcy-style rates of flow into reservoirs from injection-induced fractures.

2.2 Addition of Thermoelastic Fracture Theory

Many hydraulic fracturing simulators have been built using the theory outlined above, and have worked well for operators seeking to model reservoir stimulation through the injection of high-viscosity, proppant-laden fluids. However, because the primary driver of these fractures is high pressure, high rate injection of a high-viscosity fluid, thermal effects on the injected fluid and on the reservoir stress regime are typically neglected. Cognizant of these limitations, a few notable investigators (primarily Perkins and Gonzalez 1985) have laid the groundwork for the theory of thermal effects on fracture propagation through the study of cold water injection by waterflooding of oil reservoirs [11,33,39,52], that is, the study of injection-induced fractures.

The three main components of thermoelastic fracture theory of interest in this work, induced when a relatively cold fluid is injected into a hot reservoir, are 1) the modification of the principal Earth stresses, 2) heat transfer rates between the formation fluids, reservoir matrix, and injected fluid, and 3) resulting thermodynamic changes in the injected fluid. These principles were first investigated by Perkins and Gonzalez in 1985, from which they concluded,

> Assume rock is a linear elastic material, therefore stress changes caused by thermoelastic and poroelastic effects can be treated separately and simply superimposed to provide the modified stress distributions.

Simply put, fractures will propagate if the pressure in the fracture tip exceeds the minimum horizontal principal Earth stress. They found that the difference in temperature between the injected fluid and reservoir rock reduces the principal Earth stresses if the injected fluid is colder than the reservoir, making it possible to fracture the rock at a pressure $p_{thermal}$ lower than the nominal fracture propagation pressure $p_{nominal}$ (recall from Equation 2 $p_{nominal}$ equals $\sigma_{h,min}$). Additionally, they determined increasing the average pore pressure in the reservoir increased the principal stresses. The formulae they derived for such alterations were:

$$\Delta\sigma_T = S_f \frac{E\alpha_T \Delta T}{1-\nu} \tag{11}$$

$$\Delta\sigma_P = S_f \frac{EJ\Delta P}{1-\nu} \tag{12}$$

S_f is a geometric factor for the shape of the cooled region of reservoir rock, α_T is the coefficient of thermal expansion of the rock, J is the coefficient of pore pressure expansion (as defined by Perkins and Gonzalez 1985 paper), $\Delta\sigma_T$ and $\Delta\sigma_P$ are the

thermoelastic and poroelastic stress modifications respectively, $\Delta T = T - T_R$ injected fluid temperature minus the initial reservoir temperature, $\Delta P = P - P_R$ new reservoir pore pressure minus the original reservoir pore pressure, and E is Young's modulus.

$$S_{f,1} = \frac{b_0/a_0}{1+(b_0/a_0)} \tag{13}$$

$$S_{f,2} = \frac{1}{1+(b_0/a_0)} \tag{14}$$

Two different shape factors are used in Equations 11 and 12 to calculate the thermoelastic stress reduction on the minimum horizontal principal stress (Equation 13) and the major horizontal principal stress (Equation 14). The shape factors are functions of the ellipse dimensions shown in Figure 14. The side view of their proposed fracture is shown in Figure 15. When the thermal front is circular and a_0 equals b_0 the shape factor is ½ as calculated by Equations 13 and 14. When the thermal front ellipse is very flat ($a_0 >> b_0$) the thermoelastic effect on the minimum horizontal stress is zero because the shape factor goes to zero (from Equation 13) while at the same time the shape factor in the maximum horizontal stress direction goes to unity (from Equation 14).

Perkins and Gonzalez proposed the modified minimum horizontal principal stress as follows:

$$\sigma_{mod,h,min} = \sigma_{h,min} + \Delta\sigma_T + \Delta\sigma_P \tag{15}$$

This is the actual opposing stress that pressure in the fracture tip must then overcome in order to continue to break rock.

They proposed a set of ellipses for the cooled region and flooded region confocal with the fracture that would flatten or become more circular depending on the length of

the fracture. The dimensions of the regions were calculated as a function of the fracture length and volume of fluid injected. Within the cooled region of rock the principal Earth stresses would be reduced as described by Equation 11. Perkins and Gonzalez developed an algorithm in which the pressure at the tip of the fracture can be calculated to determine if it is larger than the modified minimum horizontal principal stress, and if so the fracture would propagate. The algorithm would then iterate until a pressure drop in the fracture caused the tip pressure to fall below the $\sigma_{mod,h,min}$ at which point the fracture would stop growing, theoretically.

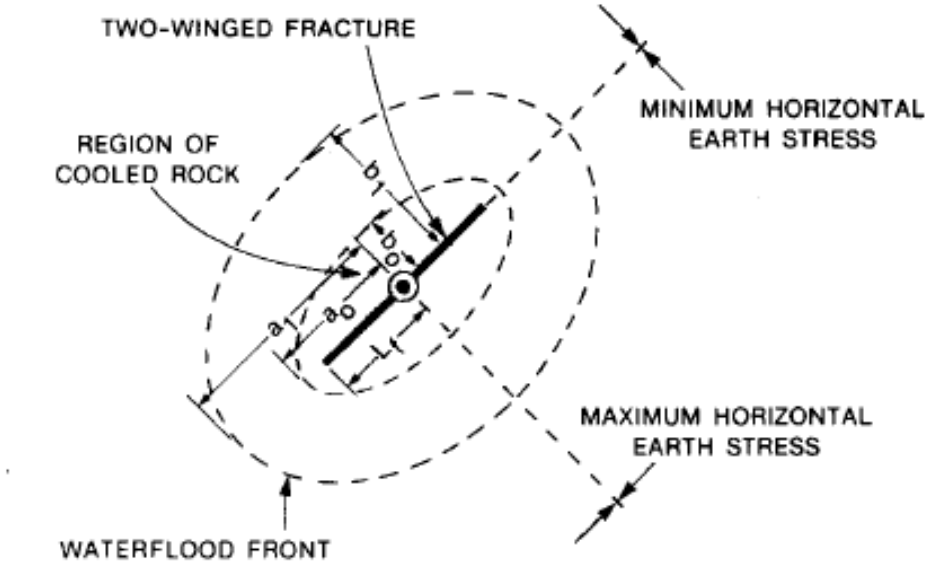

Figure 14: Plan-view showing a two-winged vertical fracture oriented parallel to the plane of maximum horizontal principal stress, and elliptical regions of cooled rock and flood front extent [33].

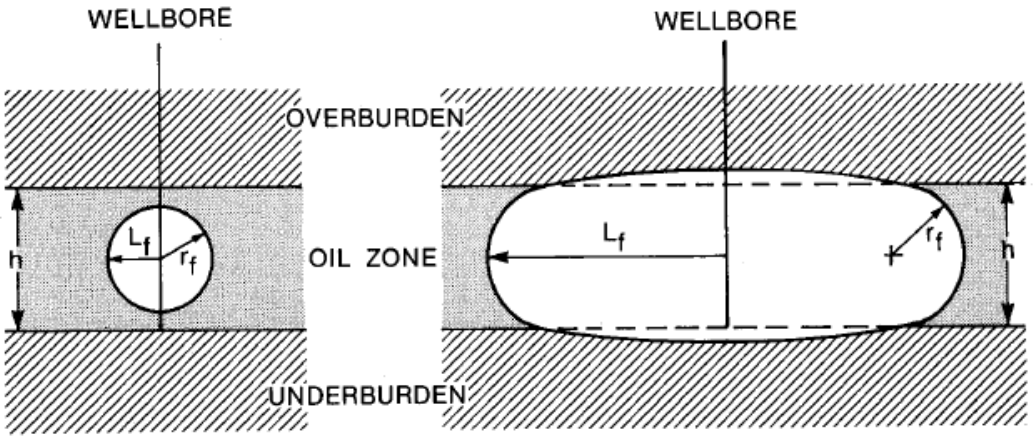

Figure 15: Side-view of a vertical two-winged fracture shortly after initiation, and later after becoming confined vertically and extending laterally [33].

2.3 Pressure Equations for Injection-Induced Fractures

The difference between a hydraulic fracture, which is deliberately implemented to increase the production of hydrocarbons from a well, and an injection-induced fracture is that the latter is simply a consequence (as opposed to an intended outcome) of long term injection of a fluid into a reservoir that will not be recovered later. The bottomhole pressure (BHP) or injection pressure during hydraulic fracturing is always greater than the nominal fracture pressure of the reservoir, $\sigma_{h,min}$. The BHP that results in an injection-induced fracture is typically less than $\sigma_{h,min}$. Nevertheless, fractures can still be induced due to other physical phenomena (viz. thermoelastic stress) as described above.

In order to determine whether a CO_2 injection-induced fracture will propagate or stop growing, it is necessary to calculate the pressure in a propagating fracture for a single component compressible fluid. The literature to date largely focuses on incompressible fluids, and the work conducted on compressible fluids is limited to

hydraulic fracturing [37,51]. Van den Hoek (2000) derived a fully transient solution of the elliptical leak-off of fluid for a propagating fracture of infinite conductivity in a reservoir of constant far-field pressure, based on work by Gringarten (1996). He sought to overcome the limitations of the Carter leak-off model for formations of high permeability containing a growing fracture. Perkins and Gonzalez (1985) also developed a method to calculate the BHP in a well used in waterflooding that induces a thermoelastic fracture. Their pressure model involved a series of resistances to flow, or pressure drops, beginning with the far field reservoir pressure, through the waterflood front, through the hot/cold front in the reservoir, into the fracture, up the fracture, through the perforations, and ultimately allowed an operator to estimate the BHP that resulted in a fracture.

In a CO_2 storage scenario, the BHP will most likely be regulated to prevent fracture propagation from the injection well, and the maximum achievable injection rate will then be a function of the allowed BHP. The pressure drop from the wellbore to the fracture tip is thus an important value to estimate in order to determine final fracture length. The Perkins-Gonzalez model estimates this pressure drop in the following fashion:

$$\Delta P_f = 1.26 \left[\frac{q\mu L E^3}{(1-\nu^2)^3 h^4}\right]^{0.25} \quad (16)$$

However, one critical assumption in this model was that the pressure drop in the fracture be dependent on a uniform leak-off rate (q) from the fracture faces. For very long, thin thermoelastic fractures filled with a low viscosity fluid that flows into a high

permeability reservoir, the assumptions of infinitely conductive fractures, uniform leak-off rates, and constant property fluids are poor [27,42,51]. No analytical, closed-form, or easily programmable solution to the conservation of mass (pressure equation) was found in a literature review that could describe the variable pressure profile in a fracture, indicating a numerical method was needed to evaluate the conservation of mass in a fractured system. Section 3.3 will further describe the constitutive equations used in the numerical model to evaluate the pressure and flow equations.

2.4 Heat Transport Equations for Injection-Induced Fractures

Thermoelastic stress effects depend on the presence of cold fluid in the reservoir rock surrounding the fracture; therefore it is important to calculate the temperature of the fluid in the fracture and out into the reservoir. Heat conduction from the Earth will warm the fluid in the fracture, but conduction of heat through rock is so low that convection will be the primary method of heat transfer in the reservoir. Heat flux from geothermal conduction, $k_{rock}dT/dx$, is typically around 0.1 W/m^2 while convective heat flux $uC_p/\Delta T/\rho$ is typically 10-20 W/m^2 for the conditions used in this thesis, as will be discussed in Chapter 5 [35,45,46]. Convection of fluid from the fracture into the reservoir- which corresponds to leak-off in hydraulic fracturing- will reduce the quantity and velocity of CO_2 traveling down the fracture to the tip. This has a primary influence on the pressure drop in the fracture and heat transfer of the whole system.

Most hydraulic fracturing software and analysis use the 1D Carter model to describe leak-off from a fracture. The failure of the Carter leak-off formula to accurately describe fluid flow from long fractures of non-constant internal pressure drives the need

to develop a better model based on the actual modified Darcy flow of fluid traveling through a porous media.

Historically, most investigation into convection-diffusion problems with fluid flow through a reservoir has been focused on characterizing tracer concentration movement (versus time and distance from the injection point). A good overview with the appropriate constitutive equations can be found in the *Water Resources Monograph* prepared by the American Geophysical Union (Javandel, 2013). Of interest in this work was the analogous temperature profile equation that can be used to calculate the temperature gradient movement from an injected fluid versus time and distance from the injection point. This subject is briefly outlined in the user guide to the PHREEQC program developed by the United States Geological Survey, and the constitutive partial differential equation that expresses the transient 1D temperature profile is [32]:

$$(\emptyset\rho_w c_w)\frac{\partial T}{\partial t} + (1-\emptyset)\rho_s c_s \frac{\partial T}{\partial t} + (\emptyset\rho_w c_w)u\frac{\partial T}{\partial x} - \kappa\frac{\partial^2 T}{\partial x^2} = 0 \qquad (17)$$

where T is the temperature, $\emptyset$ is the porosity of the rock, u is the fluid flow velocity through the porous media, ρ is the density of the solid (s) and the fluid (w), c is the specific heat, k is the thermal conductivity of the solid and fluid, and κ is a term that encompasses thermal dispersion by convective flow and heat conductivity (or thermal diffusion) in the reservoir.

Dividing Equation 17 by $(\emptyset\rho_w c_w)$ gives:

$$R_T\frac{\partial T}{\partial t} + u\frac{\partial T}{\partial x} - \kappa_L\frac{\partial^2 T}{\partial x^2} = 0 \qquad (18)$$

where;

$$R_T = 1 + \frac{(1-\emptyset)\rho_s c_s}{\emptyset \rho_w c_w} \quad (19)$$

is the temperature retardation factor and;

$$\kappa_L = \frac{\kappa}{\emptyset \rho_w c_w} = \frac{\emptyset k_w + (1-\emptyset) k_s}{\emptyset \rho_w c_w + (1-\emptyset)\rho_s c_s} + \beta_L u \quad (20)$$

is the thermal dispersion coefficient. The retardation factor is greater than unity, implying the CO_2 flood front will propagate into the reservoir faster than the temperature front. The thermal dispersion coefficient contains a component for pure diffusion, and a component for dispersion due to advection: $\kappa_L = \kappa_e + \beta_L u$ where β_L is the thermal dispersivity, and κ_e is the thermal diffusion coefficient, and u is the velocity of the fluid front [32]. Flow down a fracture, or in this work a highly permeable duct bounded by porous media, is not simply described by one partial differential equation due to the nearly line-source variable pressure gradient induced in the fracture. For this reason, the solution of the combined pressure profiles, leak-off rates and temperature fronts in the fracture and reservoir are best found using numerical methods.

The result of the injected fluid flowing into a reservoir from a fracture is a fluid flood front and a cold front that grow into the reservoir in a circular-to-elliptical shape confocal to the fracture wings (see Figure 16) [33]. The following sections will discuss the numerical methods used to calculate these flood and temperature fronts.

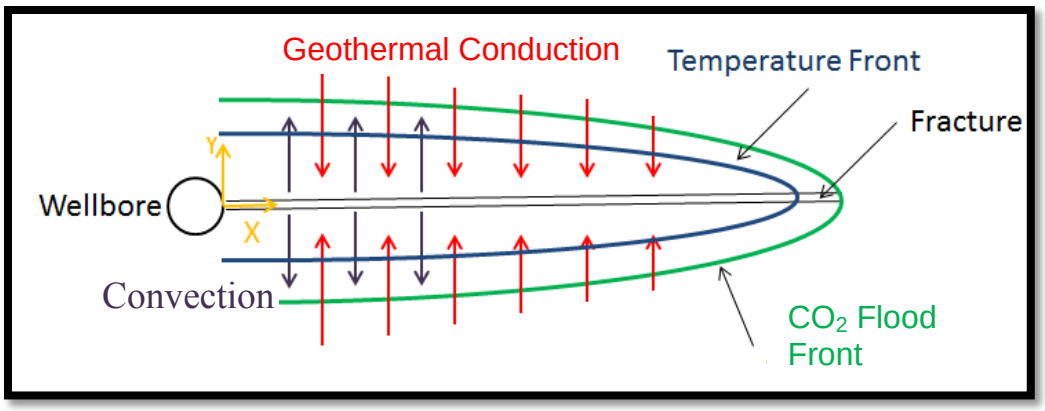

Figure 16: Plan-view diagram of flood fronts, temperature fronts, and heat transfer mechanisms of convection and conduction.

2.5 Coupled Nature of Thermoelastic Fracture Propagation Forces

From the above discussion and review of formation fracturing theory, it is apparent that calculations of fracture propagation, fluid flow and final geometry result in a transient, highly coupled problem, especially when considering the phase changes CO_2 will undergo due to depressurization and warming from its condition at the wellbore to its final resting place deep in the reservoir. To determine the impact each of the key variables of a fractured reservoir have on the final thermoelastic injection-induced fracture length, numerical simulation is the fastest and cheapest way to study the interaction of these variables:

- Formation permeability
- Fracture permeability
- Injection pressure vs. reservoir pressure
- Injection temperature vs. reservoir temperature
- Thermophysical fluid properties:
    - Viscosity
    - Density
    - Heat capacity and thermal conductivity

The solution approach used in this work is discussed in detail in the following chapters.

Chapter 3: *Modeling of Injection-Induced Fractures*

3.1 Existing Fracture Simulators and Efforts

Advances in computing power have led to the development of highly sophisticated fracture propagation software that can be used to simulate, 1) fully compositional, three-dimensional fractures, such as EFRAC-3D [37], or 2) waterflooding-induced fractures including the poroelastic and thermoelastic effects, such as UTWID [49]. UTWID is a 2D fracture propagation simulator that is essentially the Perkins-Gonzalez algorithm in easy-to-use software form. Each of these software packages could be used to estimate the final fracture length of a CO_2 injection-induced fracture. However, they were designed to simulate processes other than long-term CO_2 injection and as such neglected physical phenomena that are unique to CO_2. For example, EFRAC-3D does not include changing Earth stress due to thermoelastic or poroelastic effects, uses the 1D Carter leak-off model and is designed for hydraulic stimulation with pumping times of a few hours. UTWID does not have pressure dependent Darcy flow out of the fracture nor calculate the phase changes of the injected fluid; it uses a uniform leak-off rate of an isothermal and incompressible fluid across the entire fracture face. These are significant factors that need to be considered when modeling CO_2 injection, and therefore a new numerical simulator was built to handle these phenomena.

Other researchers have developed their own algorithms and computer code to estimate fracture geometry through the coupling of numerical reservoir simulators and geomechanical equations. These include analytical models by Detienne et al. (1998), half-analytical, half-numerical models by Hustedt et al. (2008) and van den Hoek et al.

(1996), a 3D numerical simulation by Settari (1994), and others. The physical and computational complexity of modeling the geomechanical changes in the rock coupled with reservoir fluid flows demands simplifying assumptions be made to create a tractable environment in which to study the geo-thermo-mechanical and thermodynamic issues of injection-induced fractures.

3.2 Modeling Approach

The modeling approach of this thesis involved simplifying the geomechanical calculations of actual rock cracking. The following assumptions were made to investigate specifically the thermal and fluid flow impacts on fracture growth:

1. The reservoir domain and fracture domain are homogeneous, isotropic, and have constant properties (porosity, permeability, density, thermal conductivity, and heat capacity).
2. The domain is two-dimensional, allowing fluid flow and heat transfer in only 2D.
3. The fracture is vertical due to the vertical stress being the largest of the three principal stresses.
4. No poroelastic stress effects were allowed to influence the minimum horizontal stress, or the boundary pressure.
5. The fracture has a constant, prescribed width along its entire length.
6. A large stress barrier at the interfaces of the storage reservoir and the over- and underburden constrains the height of the fracture, and so it is a PKN-type fracture.
7. The fracture is a single bi-winged feature due to a large stress contrast between the minimum and maximum horizontal stresses. No stress reorientation happens due to fracture growth or fracture branching.
8. Symmetry conditions (as shown in the Figure 21) allow the model to focus on only ¼ of a bi-wing fracture.
9. No heat is conducted from the over- and underburden layers, only from the edges of the 2D domain.
10. The injected fluid contains no particulates and is single component.
11. No crack propagation equations were solved via linear elastic porous media theory. The condition of growth was that the maximum thermoelastic stress (via

largest ΔT) applied in the fracture and the pressure in the fracture tip be larger than the modified minimum horizontal principal stress (Equation 15).

Additionally, the prescription of constant injection pressure and far-field boundary pressure led to the hypothesis that thermoelastic fractures will reach an equilibrium length. In hydraulic stimulation, fractures stop growing because the operator stops pumping. Injection pressure is sustained well above the $\sigma_{h,min}$ and the high net pressure results in highly conductive fractures during pumping. In CO_2 sequestration, the injection pressure will likely be regulated below the nominal fracture pressure, or in-situ $\sigma_{h,min}$, of the storage reservoir and held constant. Therefore, the presence of cold fluid sufficiently beneath the reservoir temperature is needed to enable fracture propagation. If the temperature of the fluid in the fracture tip rises above this threshold temperature, the thermoelastic stress reduction will be too small for the fracture to propagate. However, with the maximum thermoelastic stress reduction, the value of $\sigma_{mod,h,min}$ may fall below the injection pressure such that a fracture initiates and grows as long as the pressure in the fracture tip is higher than $\sigma_{mod,h,min}$ and as long as the fracture does not propagate beyond the temperature front, beyond which the thermoelastic stress reduction no longer applies. We will see that the latter condition is always met for the conditions expected in geologic CO_2 storage. In short, temperature effects start the fracture and the pressure decline in the fracture limits its growth.

Initially, system parameters were chosen that would result in limiting cases of fracture growth in isolation from poroelastic effects. Fracture length would be greatest when the fracture is infinitely conductive (meaning no pressure drop in the fracture) and

the surrounding matrix has zero permeability. In that scenario, the fracture would stop growing once the fluid in the fracture warmed enough to eliminate the thermoelastic stress effect. However, this scenario is extremely unlikely because the intent of CO_2 sequestration is to trap CO_2 underground, and an impermeable storage reservoir would be a poor choice. It is also instructive to consider the conditions that would lead to a very short fracture. The shortest fracture would be no fracture, and injecting below $\sigma_{mod,h,min}$ would eliminate the possibility of fracturing the reservoir. If the injection pressure is above that value, the parameters that establish the shortest fracture would be a highly permeable storage reservoir with a low permeability fracture. The pressure gradient in the fracture would then be very large, so the injection pressure would fall to $\sigma_{mod,h,min}$ in a short distance. In this thesis we explored the space between these two limits and demonstrate the system properties that cause a thermoelastic fracture to approach these limits.

For example, if the in-situ minimum horizontal stress is 42.5 MPa, the injection temperature is 355 K, the formation temperature is 400 K, and the mechanical rock properties are α_T equal to 10^{-5} 1/K, E is 17.5 GPa, ν is 0.15, then the thermoelastic stress using Equation 11 is 4.5 MPa and the smallest possible value of the modified minimum horizontal stress is 38 MPa (assuming the shape factor is ½). If the injection pressure is 39 MPa then the fracture will be initiated. The fracture will continue to propagate until the friction loss due to flow along the fracture causes the tip pressure to decline to 38 MPa. At this point the geo-thermo-mechanical equilibrium condition is satisfied, i.e. the

fluid temperature at the tip is the injected temperature and the tip pressure equals $\sigma_{mod,h,min}$. Figure 17 shows this scenario and the relationship between the stresses and ΔT.

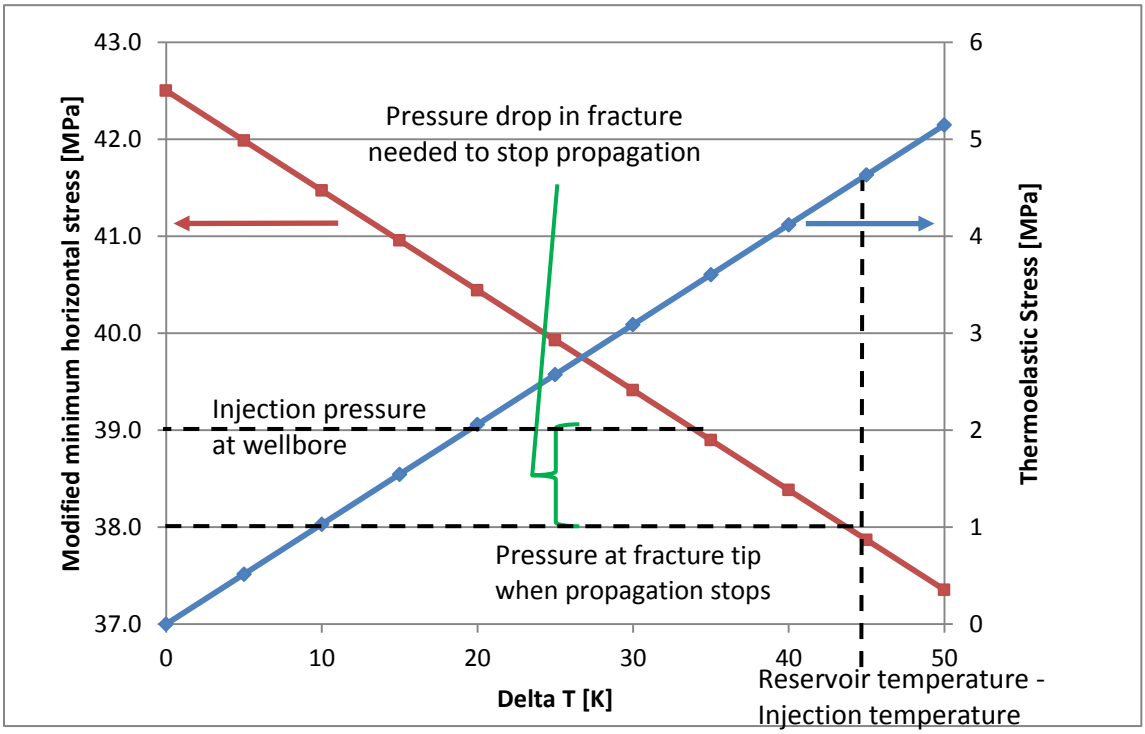

Figure 17: Thermoelastic stress (blue) and resulting $\sigma_{mod,h,min}$ (red) in the reservoir as a function of the temperature difference (Delta T) between the injected fluid and the reservoir. From the example in the text, the injection pressure is a constant 39 MPa and $\sigma_{mod,h,min}$ is 38 MPa at the ΔT of 45 K. When the fluid pressure in the fracture tip equals $\sigma_{mod,h,min}$ after a drop of 1 MPa from the wellbore to the tip, the fracture will stop propagating.

The shape of the thermal front as described by Perkins-Gonzalez (Figure 14) surrounding the bi-wing fracture controls the magnitude of the thermoelastic stress in addition to the ΔT. The maximum S_f is ½ when the front is circular, i.e. when a_0 equals b_0. For very long injection times, as would be the case in CO_2 sequestration, in a very large reservoir such that the flood and temperature fronts are allowed to grow unimpeded, an injection-induced fracture will grow in tandem with the change in temperature front

shape. At the start of injection the fronts will be perfectly circular, but then the thermoelastic stress effect will cause a fracture to grow out to the point where the fronts will be somewhat elliptical, reducing S_f and therefore reducing the thermoelastic stress such that fracture growth is no longer possible given the constant injection pressure. As time passes the front will then become more circular thereby increasing the thermoelastic stress allowing the fracture to grow. The evolving shape of the thermal front will determine the speed of fracture growth.

The pressure decline in the fracture then becomes important because along long fractures in high-permeability formations significant pressure gradients will exist. At the extreme, a long fracture will exist surrounded by a circular thermal front providing the maximum thermoelastic stress at the fracture tip, but friction in the fracture and leak-off will cause the tip pressure to decline proportional to length, such that any net pressure ($P_{fracture\ tip} - \sigma_{mod,h,min}$) must fall to zero. At that point, equilibrium is established regardless of any further growth of a temperature front into the formation.

The purpose of the simulation was thus to 1) calculate the advance of the thermal fronts in a fracture to determine how quickly the thermoelastic stress is applied to the rock at the fracture tip, 2) to calculate the pressure gradient in the fracture to determine at what fracture length the pressure at the tip equals $\sigma_{mod,h,min}$ (net pressure falls to zero), and 3) to determine the sensitivity of the fracture equilibrium to the variables mentioned in Section 2.4. Finally iterative tests were performed to find the fracture length that resulted

in a tip pressure equal to $\sigma_{mod,h,min}$ as long as a maximum $\Delta\sigma_T$ was present given the hypothetical case parameters selected.

The figures below illustrate the three possible pressure profiles in the fracture that would indicate the fracture is too short (Figure 18) and not at equilibrium, too long (Figure 19) and therefore not physically possible, or at a static equilibrium wherein the pressure at the tip of the fracture equals $\sigma_{mod,h,min}$ (Figure 20).

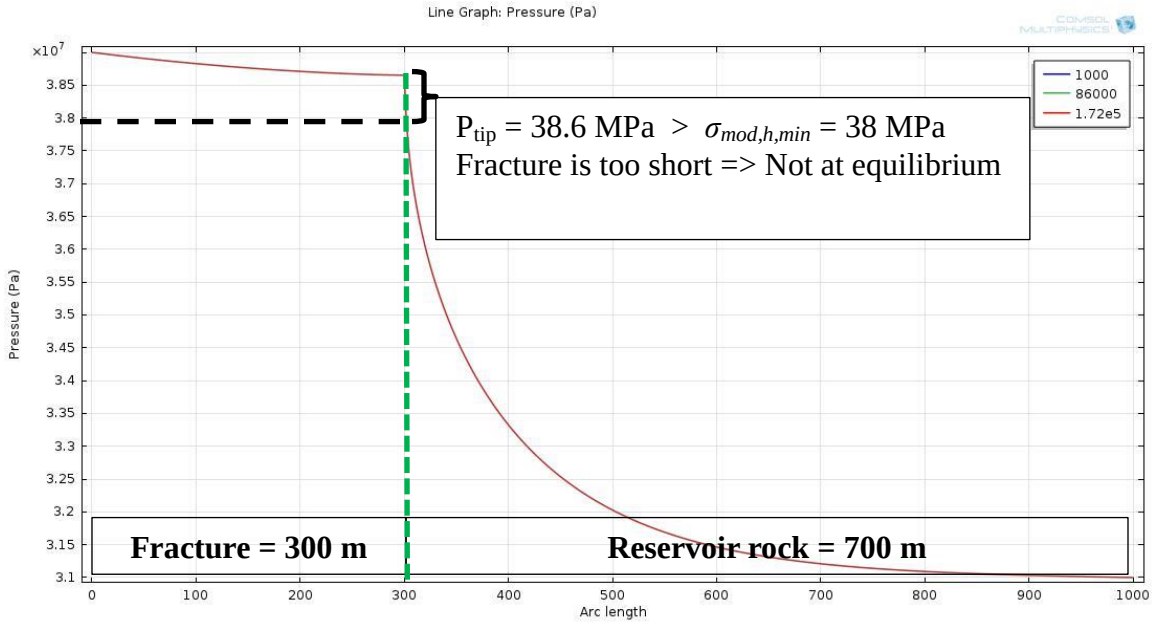

Figure 18: Pressure inside the fracture at the centerline (y = 0, 0 < x < 300 m) and in the reservoir (y = 0, 300 < x < 1000) at the conditions of Run 1 (see Table 6) when fracture length is assumed to be 300 m. The legend indicates the elapsed time during the simulation. This plot demonstrates one step in the iterative process for determining fracture length; here the fracture is not at equilibrium because it is too short, resulting in a tip pressure above the $\sigma_{mod,h,min}$. A longer fracture is needed.

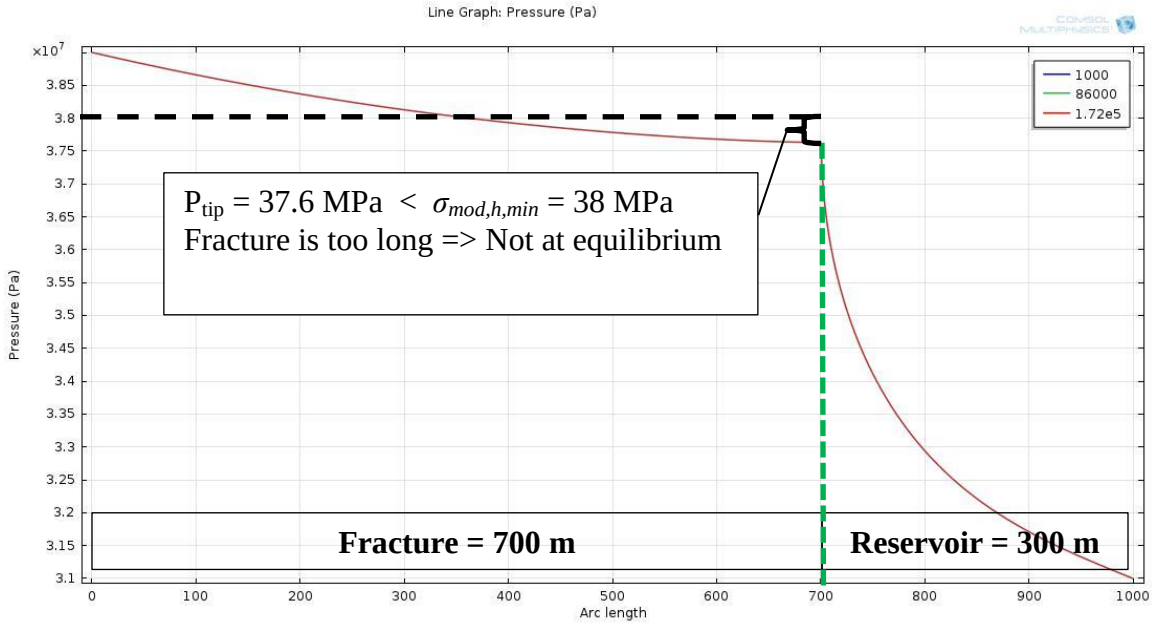

Figure 19: Pressure inside the fracture at the centerline (y = 0, 0 < x < 700 m) and in the reservoir (y = 0, 700 < x < 1000 m) at the conditions of Run 1 (see Table 6) when the fracture length is assumed to be 700 m. The legend indicates the elapsed time during the simulation. This plot also demonstrates one step in the iterative process: here the fracture is too long and therefore not physically possible because the tip pressure is less than $\sigma_{mod,h,min}$. A shorter fracture is needed.

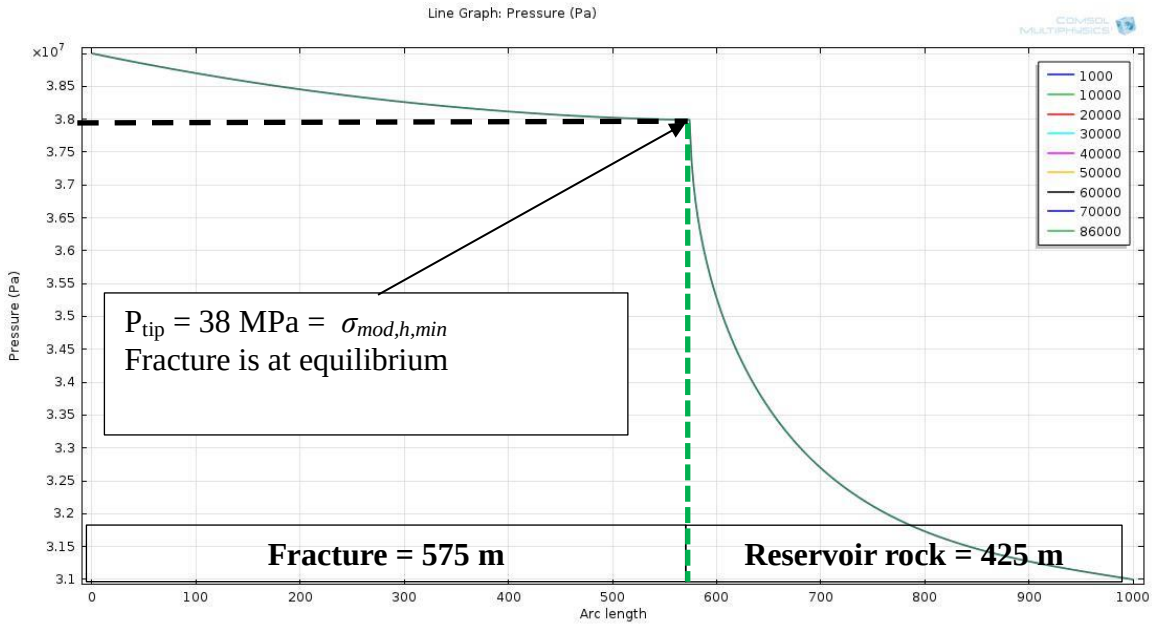

Figure 20: Pressure inside the fracture at the centerline (y = 0, 0 < x < 575 m) and in the reservoir (y = 0, 575 < x < 1000 m) at the conditions of Run 1 (see Table 6) when the fracture length is assumed to be 575 m. The legend shows the elapsed time during the simulation. This plot demonstrates the final step of the iterative process where the fracture tip pressure is equal to $\sigma_{mod,h,min}$ so the fracture would stop growing at this length.

3.3 Suitability of COMSOL Multiphysics Software

The commercial software used in this thesis to solve the coupled physical processes was COMSOL Multiphysics 4.3b. It uses a finite-element discretization coupled with a Newton-method solver for the partial differential equations describing convection-diffusion heat transfer with the continuity equation and Darcy's Law for flow through the fracture and porous media.

In order to achieve convergence of a solution, the fracture and the reservoir were both defined as porous media. COMSOL was able to quickly find a solution when all fluid flow in the system was calculated using Darcy's Law instead of coupling the Navier-Stokes equation for free flow through a duct with Darcy's Law for flow through

porous media. In reality a fracture held open by a high net pressure may act like a vacant duct of aperture a few centimeters (equivalent to permeability of hundreds of thousands of Darcys) which may be better described by the Navier-Stokes equation. With a low net pressure the aperture may be a few millimeters (equivalent to permeability on the order of thousands Darcys). Specifying the fracture as a highly porous, highly permeable channel should not detract from the accuracy of the simulation results due to the variety of possible net pressures in geological CO_2 storage and the ability to vary the permeability of the fracture even though it is of constant width. With this specification, only one governing equation for fluid flow was needed for every element in the simulator domain, Equation 21, enabling the simulator to rapidly converge on a solution.

$$Q_m = \frac{\partial}{\partial t}(\rho\varphi) + \nabla \cdot \rho[\frac{k}{\mu}(\nabla P)] \qquad (21)$$

Q_m is the mass source term, ρ and μ are the density and viscosity of the fluid that can be either constant or calculated from an equation of state, k is the permeability and φ is the porosity. The domain was only in two horizontal dimensions so there is no gravity term in the equation, and no convection currents inside a vertical fracture were involved.

The built-in equation of state in COMSOL did not calculate the viscosity and density correctly, when compared to the property data from the NIST Thermophysical Webbook. Consequently, an EOS for density and viscosity as a function of temperature and pressure was derived from a multivariate-regression on data accessed through the NIST Thermophysical Webbook. It was a set of polynomials wherein viscosity (in Pa-s)

was only a function of temperature (T, in Kelvin) and density (in kg/m^3) a function of temperature and pressure (P, in Pascals).

$$\mu = 2.84424 * 10^{-9}T^2 - 2.56038 * 10^{-6}T + 6.23346 * 10^{-6} \quad (22)$$

$$\rho = 1675.5796 - 3.490909T + 9.69737 * 10^{-6}P \quad (23)$$

Thus it was possible to run simulations with variable fluid properties to demonstrate their relative strength in limiting the equilibrium fracture length.

Chapter 4: *Setup of Model in COMSOL*

4.1 Geometry of System

The hypothetical PKN-type fracture has two wings and is symmetrical along two axes: one through the centerline of the fracture and the second is perpendicular and cuts through the wellbore. Taking advantage of the symmetry one quarter of this system was modeled as shown in Figure 21 below.

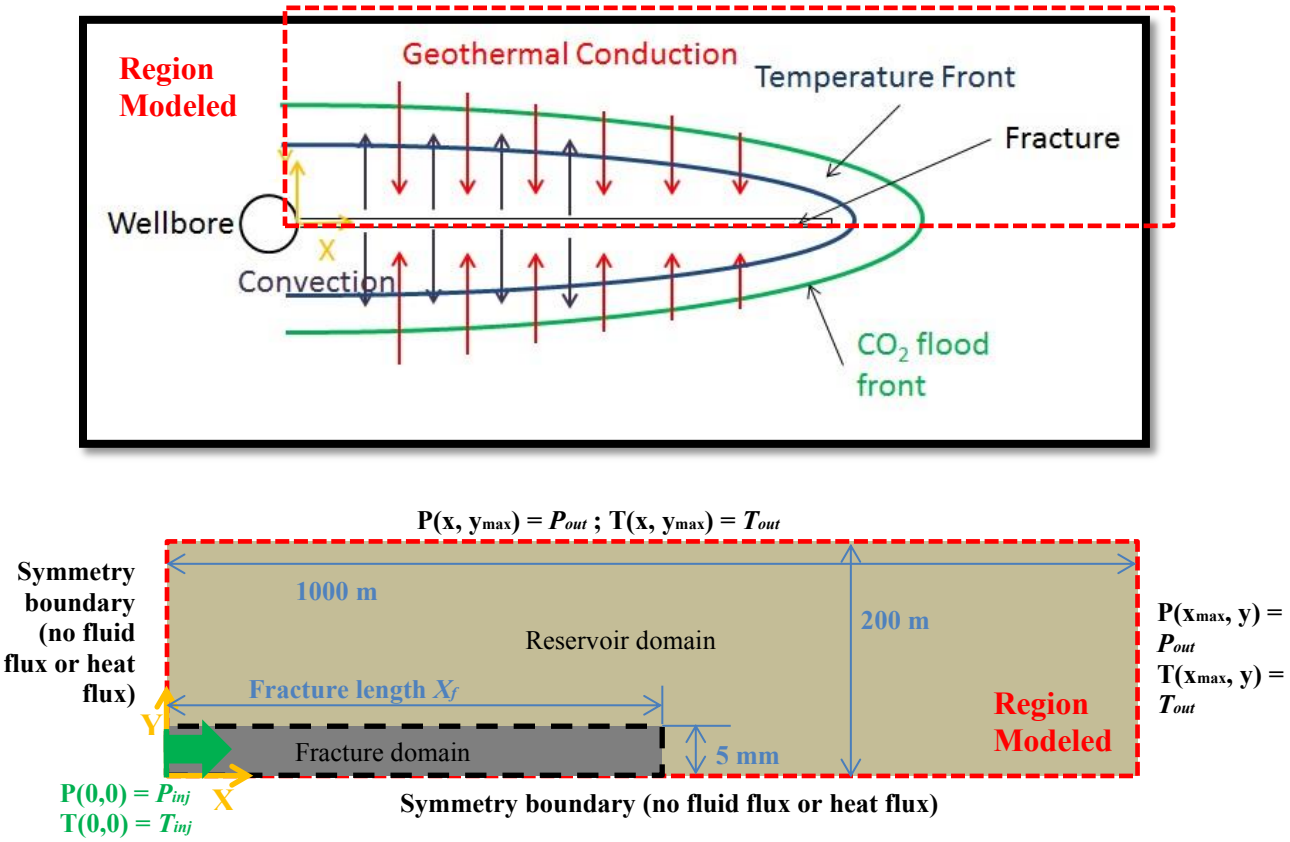

Figure 21: Upper panel shows temperature and flood fronts extending into a reservoir from a fracture, and the heat transfer mechanisms of convection and conduction. The lower panel delineates the region modeled in COMSOL (red dashed rectangle) and the mathematical boundary conditions and geometry of the fracture and reservoir domains. Expanded domain properties are in Section 4.2-4.4. The lower symmetry boundary cuts through the center of the fracture, so only ½ of its width was modeled in COMSOL. The green vertical line at the left side of the fracture domain is the inlet to the system with the conditions in green font below.

The reservoir domain was rectangular of constant dimensions for all runs: 1000 meters long by 200 meters wide (see Figure 23). The fracture was directly adjacent to the reservoir rock with no special coupling functions or boundary specification at that wall between the two porous domains. The fracture subdomain was a rectangle with a five millimeter uniform width, and a variable length that was lengthened or shortened to find the equilibrium fracture length depending on the other properties of each run.

The choice of fracture width merits discussion. The width of the fracture was calculated from Equation 4.2 for a crack opening in an infinitely sized elastic medium (see Figure 22). Given hypothetical reservoir properties of 0.15 Poisson's ratio, Young's modulus of 17.5 GPa, shear modulus of 20 GPa, a net pressure of 1 MPa, and a fracture height of 100 meters, the maximum width of a PKN elliptical fracture (as shown in Figure 11) is about 8.5 mm. If the hypothetical fracture were 50 m tall, the estimated width from the Sneddon solution (Equation 4.2) would only be 4.2 mm with the same shear modulus, Young's modulus, Poisson's ratio and net pressure from before. If the net pressure were increased to 4 MPa in the 50 m tall fracture, the width would be 17 mm. Physically then it is conceivable the injection-induced fractures could be around one cm in width.

Computational considerations also influence the choice of fracture width in this study. Solver limitations in COMSOL could not handle a feature thinner than 5 mm while in the same system as a 200 m by 1000 m feature. Therefore given the range of fracture widths possible in CO_2 storage fields and the solver limitations, 1 cm total width was used, so a 5 mm half-width was specified in the quarter-domain the simulations.

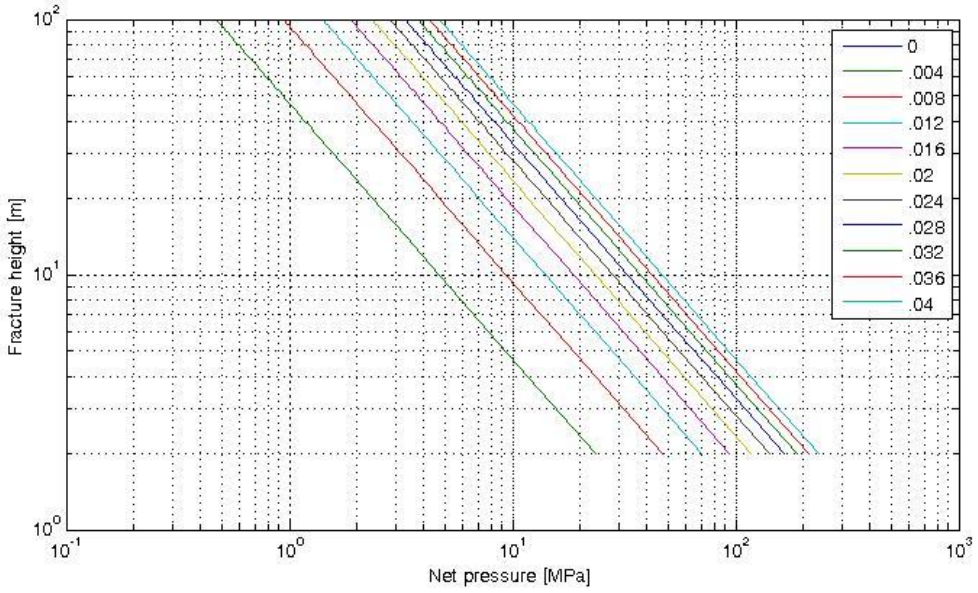

Figure 22: Fracture width (in m as listed in the legend) versus net pressure on the x-axis and fracture height on the y-axis. This plot was generated using the Sneddon solution for the crack width in an infinitely large elastic medium, as in Equation 4.2.

Depending on the net pressure and rock mechanical properties of a true CO_2 storage reservoir, a fracture may be wider or thinner than this value. In order to achieve solver convergence and provide consistency to compare the different runs, the width of the fracture was held constant across all runs. To emulate a variable fracture width which is the primary driver of its permeability as per Equation 6, and to determine how this affects the fracture length, the permeability of the fracture was varied instead.

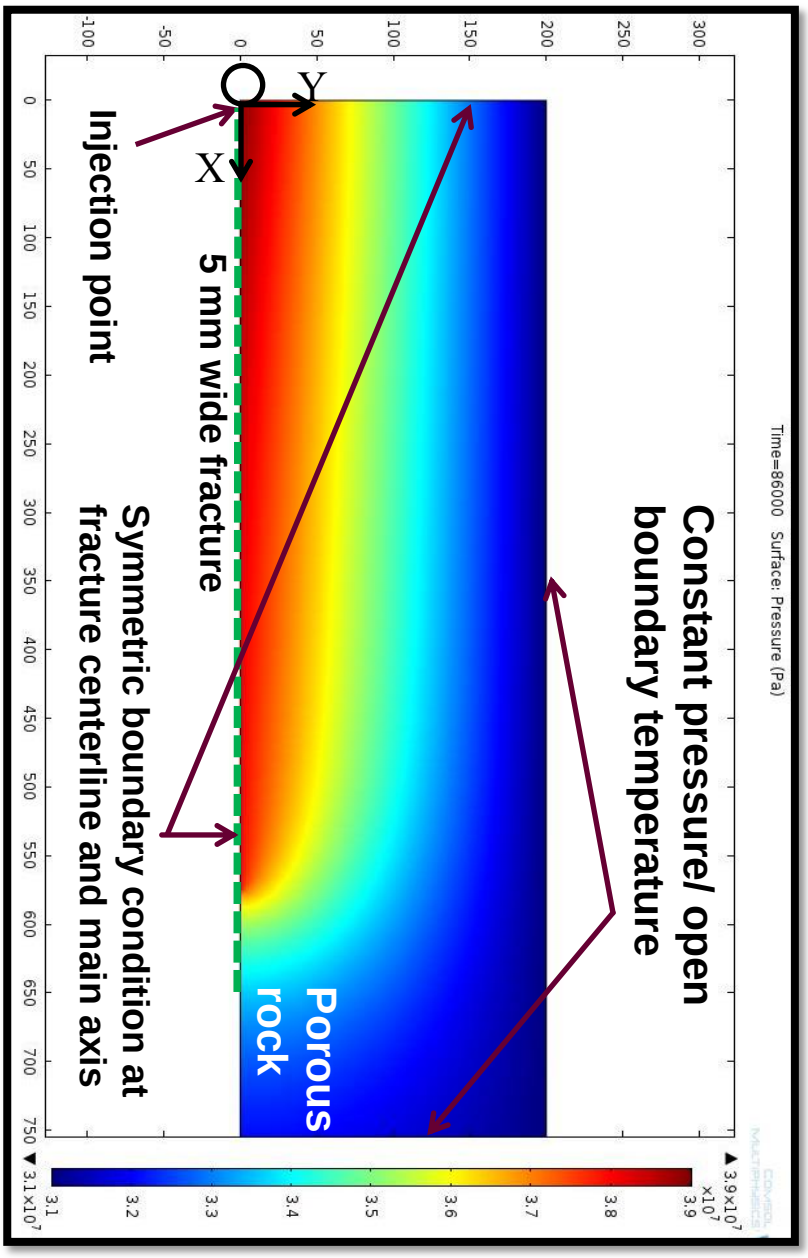

Figure 23: Diagram of the reservoir and fracture domains in COMSOL with pressure and temperature boundary conditions. This diagram also shows the typical pressure observed during a run. The x-axis is parallel to the $\sigma_{h,max}$ and is the direction of fracture propagation, and the y-axis extends into the reservoir parallel to $\sigma_{h,min}$.

4.2 Example Reservoir Rock Properties and Injection Conditions

The reservoir conditions were selected based on field data from the Cranfield CO_2 pilot storage site [24]. Injection data for a well in the Cranfield Field, as shown in Figure 24, provided the reservoir pressure, injection BHP, injection BHT, and reservoir temperature. Consequently, the inlet point of the model was set to a constant pressure of 39 MPa and temperature of 355 K. The open boundaries of the domain were set to a constant pressure as well (31 MPa as per the reservoir pressure measured in the Cranfield storage site), and an open temperature boundary allowing heat flux across the boundary with a far field temperature of 400 K. These boundary conditions are illustrated in Figure 23.

The 31 MPa reservoir pressured measured at Cranfield was a far-field pressure. It would remain constant only at very long distances from the well during injection (at a kilometer or more away from the injection well). The simulations in this thesis specified the 31 MPa boundary pressure only 200 m away from the injection point. This induced a much larger pressure gradient from the wellbore to the boundary, which would result in very large injection rates, much larger than were observed in the field. The simulation results will be discussed more in Chapter 5, but in order to more accurately capture the pressure gradients induced in the field, and to determine the effect the pressure gradient has on equilibrium fracture length, multiple runs were made at various boundary pressures, all set 200 m away from the injection point.

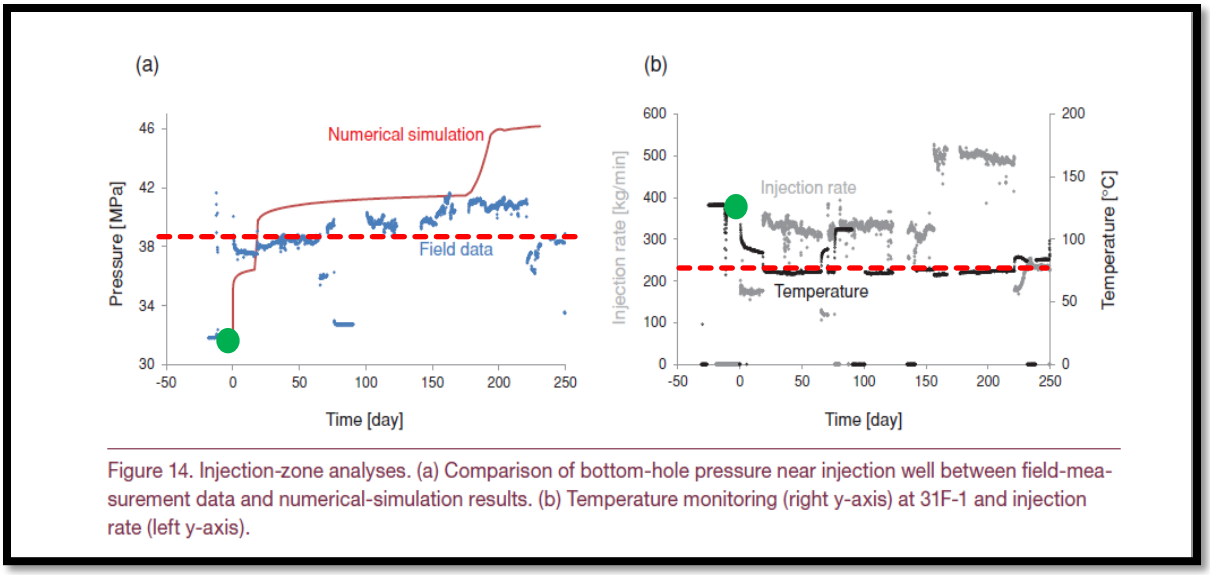

Figure 24: Recorded bottomhole pressure (left panel) and temperature (right panel) in a Cranfield CO_2 injection well [24]. The numerical simulation refers to work performed by researchers at the UTBEG. The green dots represent the initial conditions in the reservoir before any injection, and the red dashed lines represent the bottomhole injection conditions used in this thesis.

The rock properties used in the Earth stress calculations were also pulled from the Cranfield storage reservoir data (shown in Table 1). The minimum horizontal stress correlation used in the absence of actual injection test data (Equation 2 neglecting tectonic stresses) implied $\sigma_{h,min}$ was about 42.5 MPa. The thermoelastic stress (Equation 11) was about 4.5 MPa and consequently the modified minimum horizontal stress (Equation 15) $\sigma_{mod,h,min}$, was about 38 MPa when in contact with the fluid at 355 K. Table 2 shows the range of thermoelastic stresses as a function of the temperature difference between the reservoir and injected fluid.

Coefficient of thermal expansion	**10^{-5}**	**1/K**
Young's Modulus	**17.5**	**GPa**
Poisson's ratio	**0.15**	
Shear modulus	**20**	**GPa**
Vertical Earth stress	**53.5**	**MPa**

Table 1: Mechanical rock properties from the Cranfield storage site [24].

ΔT [C]	$\Delta\sigma_T$ [Pa]
5	$5.15*10^5$
10	$1.03*10^6$
15	$1.54*10^6$
20	$2.06*10^6$
25	$2.57*10^6$
30	$3.09*10^6$
35	$3.60*10^6$
40	$4.12*10^6$
45	$4.63*10^6$
50	$5.15*10^6$

Table 2: Thermoelastic stress reductions across a range of temperatures using the Cranfield conditions mechanical properties from Table 1.

The rectangular reservoir rock domain had constant properties in each run that were representative of generic sandstone reservoirs that could possibly be used for CO_2 storage, similar to those shown in Figures 4-6 [24,45,46]. The rock properties used in this thesis can be found in Table 3. Permeability was constant in each run but to test the sensitivity of the equilibrium fracture length to reservoir permeability multiple runs were made at different permeabilities (64 mD and 1000 mD). The bulk thermal properties of a fluid saturated rock are a function of the bulk volumes of fluids and grains, and the individual material properties. Heat capacity and thermal conductivity values for CO_2-saturated rock were calculated from the average of the water-saturated and air-saturated

sandstone values collected by Sommerton (as shown in Samples 1 and 2 of Figure 6) because CO_2 has a thermal conductivity and heat capacity between water and air at the conditions of the reservoir used in the simulator (355 K and 31 MPa).

Grain Density	**2650**	**kg/m^3**
Heat Capacity at Const. Pressure	**910**	**J/kg-K**
Permeability	**64 and 1000**	**mD**
Porosity	**0.25**	
Thermal Conductivity	**1.82**	**W/m-K**

Table 3: CO_2-saturated reservoir rock properties used in the COMSOL models. Grain density, heat capacity, porosity and thermal conductivity are representative of generic sandstone reservoirs [24,45,46]. The two values of permeability were based on the Cranfield storage reservoir and a higher value to test the fracture length sensitivity to reservoir permeability.

4.3 Fracture Properties

The rectangular fracture was also represented as a porous medium similar to the reservoir but with much higher permeability and porosity. In reality an injection-induced fracture may be closer to an empty duct than a porous medium. For the reasons described in Section 3.3 however, the computational difficulty of solving the Navier-Stokes equation in a duct and coupling that solution to Darcy flow in the reservoir drove the choice of representing a porous medium. In an attempt to represent the flow field in the fracture domain, the porosity and permeability were specified as much larger values than in the reservoir rock, and the thermal conductivity, heat capacity and density were set to match the fluid properties. Multiple runs were made at different permeabilities to

determine the sensitivity of the fracture length to the fracture permeability. The fracture properties are described in Table 4.

Grain Density	**720**	**kg/m^3**
Heat Capacity at Constant Pressure	**1850**	**J/kg-K**
Permeability	**100,000 and 10,000**	**D**
Porosity	**0.8**	
Thermal Conductivity	**0.083**	**W/m-K**

Table 4: Fracture domain properties. Different runs were made using the two permeabilities to test the sensitivity of the fracture length to the permeability. All other properties were consistent for the simulation runs, set equal to the average CO_2 values of density, heat capacity and thermal conductivity for the reasons described in the text.

4.4 Fluid Properties

Some simulations were run with a constant property CO_2 fluid for computational simplicity and to test the accuracy of the results, i.e. were they within engineering reason. The properties shown in Table 5 were chosen based on an average temperature and pressure of the system, with pressure bounds of 31 and 39 MPa, and temperature bounds of 355 and 400 K. The fluid properties were calculated from values in the NIST Thermophysical Webbook and were used in the Run 1 base case to which the other runs were compared with other fluid and rock property variations.

Dynamic Viscosity	**$6.36*10^{-5}$**	**Pa-s**
Density	**720**	**kg/m^3**
Heat Capacity at Const. Pressure	**1850**	**J/kg-K**
Thermal Conductivity	**0.083**	**W/m-K**

Table 5: CO_2 properties used in constant-property simulation runs. Other runs were made that allowed the fluid density and viscosity to change with temperature and pressure. The EOS used in those runs is presented in Section 3.3.

The constant property cases assumed the fluid occupying the reservoir matrix had the same properties as the fluids being injected. The intent was to determine only the pressure gradients in the fracture and reservoir, and the progress of thermal fronts in the fracture and reservoir. Sensitivity analysis on the fluid density and viscosity was then performed, varying each property individually to test their impact on the equilibrium fracture length, but held constant in each run.

The simulation constraints were then loosened and the impact of compressibility and variable viscosity (viscosity as a function of temperature and pressure such that the viscosity of the fluid in the reservoir matrix was different from that in the injected fluid and in the fracture) within one run was determined through the use of the EOS described in Section 3.3. The effect of relative mobility was also investigated, as the low pressure, high temperature reservoir rock would have lower viscosity CO_2 resulting in a higher mobility than the higher pressure, lower temperature CO_2 flowing into the reservoir from the fracture. In other words, given the same pressure gradient in the direction perpendicular to the fracture (*dP/dy*), the initially present fluid would flow at a higher rate than the injected fluid. Conversely at a given flow rate, the backpressure applied by a

low viscosity fluid in the reservoir would be smaller, enhancing the flow rate out of the fracture, resulting in a shorter fracture. If the viscosity of the injected fluid is the same as the viscosity of the fluid in the reservoir, the fracture would be longer. If the viscosity of the fluid in the reservoir were larger than the injected fluid, the fracture would be longer still.

From analysis of waterflooding, the common industry correlation describing the mobility of a displacing fluid to an in-situ fluid (commonly water, fluid 1, displacing oil, fluid 2 in Figure 25) is the mobility ratio M where the permeabilities k_1 and k_2 are relative permeabilities of the fluids moving through the rock and μ is the viscosity. If M is unity the two fluids will flow at the same rate through a porous medium under a constant pressure gradient. If M is less than unity fluid 1 will flow at a lower rate through a reservoir than fluid 2 under the same pressure gradient, and vice versa.

$$M = \frac{k_1/\mu_1}{k_2/\mu_2} \tag{24}$$

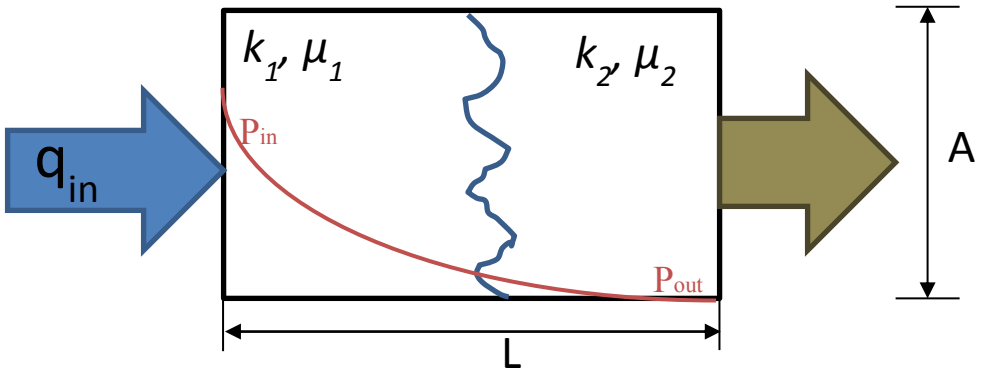

Figure 25: Schematic of an injected fluid displacing an in-situ fluid of different viscosity.

Another correlation used to describe the ease of injecting fluids into a reservoir is through the injectivity function. The injectivity of the formation is a function of the

pressure differential (between BHP and reservoir pressure) and the fluid viscosity, as represented by Equation 25 for the case of linear flow. More analysis of these factors will be presented in Chapter 5 and used to compare the results of runs using different viscosities.

$$I = \frac{q}{\Delta P} = \frac{kA}{L\mu(P,T)} \tag{25}$$

Other possible sequestration scenarios are CO_2 dissolved in brine, injected into a brine-filled reservoir, pure CO_2 injected into a brine-filled reservoir (whereby the reservoir fluid would have a higher viscosity and density than the CO_2), CO_2 injected into an oil bearing reservoir, or water injected into an oil-filled reservoir. These scenarios are discussed in later sections. The relative permeability effects of CO_2 and other fluids present in the reservoir and competing with each other were not captured as they flow through pore space were not captured.

Chapter 5: *Results and Discussion*

The purpose of the simulations described in Chapter 4 was to find the fracture length that led to thermo-mechanical equilibrium at the fracture tip. In all the scenarios a fracture reached equilibrium when the tip pressure equaled 38 MPa and the tip temperature was equal to the inlet temperature, 355 K, applying the full thermoelastic stress reduction to the minimum horizontal stress in the formation, i.e. $\sigma_{mod,h,min}$ equals 38 MPa. As discussed in Chapter 4, these equilibrium values are particular to the choice of boundary conditions, fluid properties and rock properties chosen to illustrate a typical storage reservoir. Furthermore, the intent was to identify the competition between 1) the rate of convective heat transport in the fluid and rate of conduction from the Earth as a heat source, and 2) between heat transfer (controlling the thermoelastic stress magnitude) and momentum transfer (controlling the pressure in the fracture). The sensitivity of these rates to the material properties of the fracture, reservoir rock, and fluid were investigated to determine the quantitative change in fracture equilibrium length. A summary of all the runs performed is presented in Table 6.

The three important outputs from each run were 1) the pressure profile in the fracture, 2) the speed of the temperature front in the fracture, and 3) the injection rate into the reservoir system. Runs 1 through 9 were representative of late time injection behavior in a storage reservoir, and the calculated pressure profiles in the fracture and reservoir would only exist at the time at which the fracture is at its equilibrium length, meaning they are static. At late time the thermal and CO_2 flood fronts have extended deep into the reservoir such that the fluid properties in the near-fracture area (which is the domain

modeled in this work; recall it extends 1000 m in the direction of the fracture and 200 m in the direction perpendicular to the fracture) are constant, as is the case in Run 1 through 9.

The geometry of the temperature fronts expanding into the reservoir calculated by COMSOL in these runs are not representative of the true geometry of temperature fronts that would exist in real storage scenarios. This is because each run began with a prescribed fracture of constant geometry instead of calculating fracture propagation as the temperature front expanded into the reservoir. True temperature front geometry changes are described in Section 3.2. However, the heat transfer calculations by COMSOL provided a quantitative answer to the rate of temperature front travel down the fracture, largely indicating temperature fronts move very quickly to the tip of the fracture. The final output of interest from the simulations was the injection rate. Because the simulated pressure gradients are much larger than in the field, the injection rates calculated by COMSOL were not representative of truly attainable rates in the field, but they enabled quantitative comparison of the effects individual system parameters have on the injection rate. The rates relative to one another provided the basis for drawing conclusions about the injection rate's dependency on the system parameters.

Finally, Runs 10 and 11 delivered the three key outputs for early time injection. That is the time at which the flood front has extended into the storage reservoir confocal to the fracture, but the temperature front is lagging behind. In these runs the fluid properties were calculated through the EOS (Equations 22 and 23), displaying the effect of the mobility ratio (Equation 24) and variable density (due to pressure and temperature

varying with time and position) on fracture equilibrium length, the rate of temperature front travel and injection rate. Those two runs also provide qualitative results that could be extrapolated to how a brine-filled reservoir at virgin conditions would impact fracture growth of a CO_2 injection induced fracture, neglecting relative permeability effects, mixing, and any chemical reactions.

INPUT								OUTPUT
Run	**Reason for change**	**Boundary pressure [MPa]**	**Rock perm. [mD]**	**Fracture perm. [D]**	**Fluid viscosity [Pa-s]**	**Fluid density [kg/m^3]**	**Rock spec. heat [J/kg-K]**	**Frac. length [m]**
1	Base case	31	64	100,000	$6.36*10^{-5}$	725	1850	**575**
2	Viscosity sensitivity	31	64	100,000	$2.91*10^{-4}$	725	1850	**575**
3	Viscosity sensitivity	31	64	100,000	$1.00*10^{-3}$	725	1850	**575**
4	Density sensitivity	31	64	100,000	$6.36*10^{-5}$	970	1850	**575**
5	Heat capacity sensitivity	31	64	100,000	$6.36*10^{-5}$	725	4142	**575**
6	Reservoir permeability	31	1000	100,000	$6.36*10^{-5}$	725	1850	**150**
7	Fracture permeability	31	64	10,000	$6.36*10^{-5}$	725	1850	**160**
8	Boundary pressure	35	64	100,000	$6.36*10^{-5}$	725	1850	**880**
9	Boundary sensitivity	37	64	100,000	$6.36*10^{-5}$	725	1850	**>1000**
10	Variable fluid properties	31	64	100,000	Variable	Variable	1850	**480**
11	Permeability and variable fluid property sensitivity	31	1000	100,000	Variable	Variable	1850	**135**

Table 6

Table 6, cont.: Summary of simulation cases. Italicized input indicates a variable change from a previous case. Note Run 9 would result in a fracture length outside the domain, but for consistency across results the domain size was kept constant for all runs. Runs 1-9 had constant fluid properties across the whole system (same properties for the injected fluid in the fracture and for the original fluid in the reservoir) representing the situation at late time in CO_2 storage. Runs 10 and 11 involved injecting a fluid of higher viscosity and density (in the fracture) while a lower viscosity and density is flowing in the reservoir, but the heat capacity and thermal conductivity were constant across the whole system for these runs. This situation represents the situation very early in the CO_2 storage process.

5.1 Run 1: Base Case

The first run established a base case to which all other runs were compared. In a reservoir of 64 mD and static reservoir properties as listed in Table 3, a fluid of constant density, viscosity, heat capacity and thermal conductivity (Table 5) was injected at 39 MPa and 355 K. The fluid in the reservoir had the same constant properties as the fluid injected. The fracture permeability was set to 100,000 D (other properties Table 4) and the boundary conditions were 31 MPa and a 400 K external temperature.

The fracture equilibrium length was found to be about 575 m and the cold front in the injected fluid reached the fracture tip within two days of injection. Figure 26 shows the pressure profile along the fracture at the centerline and extending into the reservoir ahead of the tip. Figures 18-20 demonstrated the iterative process used in this thesis wherein a fracture length was prescribed in COMSOL, then the simulator run to determine if the prescribed length was too short or too long such that the tip pressure was not equal to $\sigma_{mod,h,min}$. Other fracture lengths were then tried until the pressure equilibrium condition was found.

Figure 27 shows the temperature profile in the fracture at the centerline as a function of time, plotted at the elapsed time shown in the legend. Relative to the lifetime of an injection well, which could be 10 years or longer, the thermal front reached the fracture tip almost immediately. This means that for practical purposes the maximum temperature differential (i.e. reservoir temperature less injected fluid temperature) will be applied to the fracture tip at all times of injection. The fracture will grow as rapidly as the radial temperature front progresses into the reservoir, as described in Section 3.2,

providing the shape factor of ½ resulting in the application of the maximum thermoelastic stress reduction. As the fracture propagates, flow into the reservoir will reduce the pressure within the fracture, and ultimately the tip pressure is not large enough to overcome $\sigma_{mod,h,min}$ and the fracture ceases growing regardless of the $\Delta\sigma_T$.

The injection rate in this case was calculated to be 0.0225 m²/s (which is 1543 tons per day per meter of fracture height) or in a hypothetical 100 m tall fracture 2.25 m³/s (154,300 tons per day). Achievable rates in the field are smaller than these simulated values because the pressure gradients applied in the simulation are much larger than those in the field, and relative permeability effects which are ignored in the simulation can reduce the overall mobility by a factor of three to five. Run 8 demonstrated the effect of a smaller pressure gradient, which is indicative of the fracture lengths expected in true storage reservoirs. However, as will be discussed later, comparing the injection rates between other runs and this base case will demonstrate the effects of certain system properties on the injection rate.

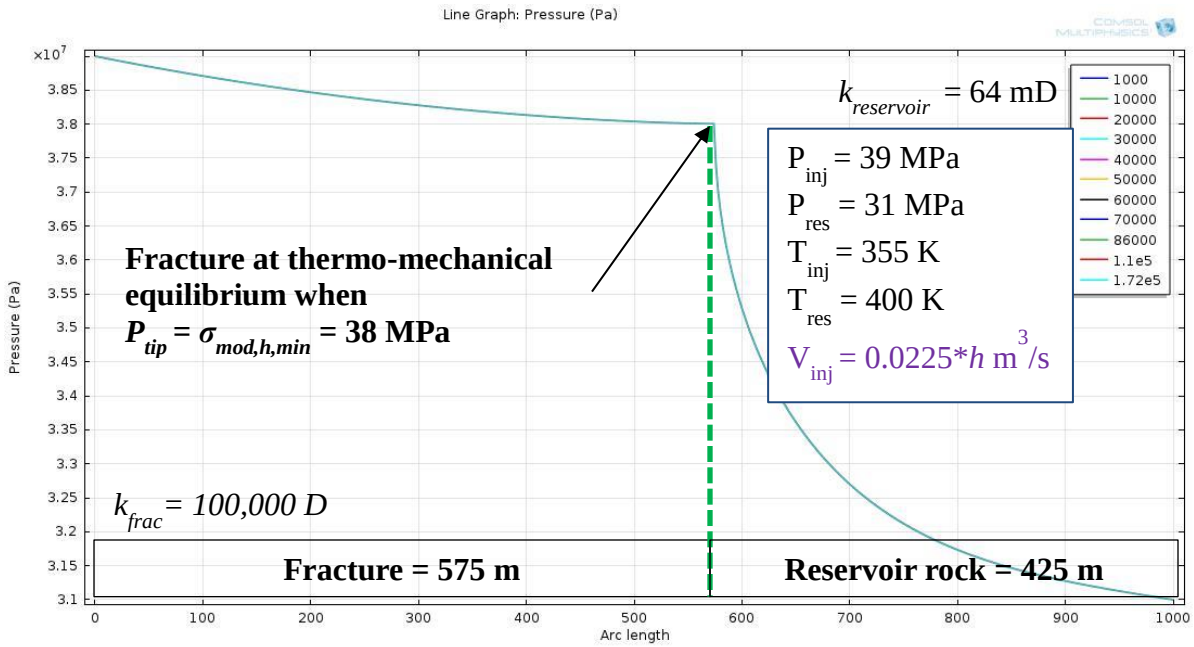

Figure 26: Pressure inside the fracture at the centerline and in the reservoir rock beyond the fracture tip in the same plane as the fracture, at the conditions of Run 1 (see Table 6). The legend indicates the elapsed time in seconds, up to two days of injection; notice the steady-state nature of the pressure (all profiles are essentially the same) due to the static reservoir properties and boundary conditions (P_{inj} = 39 MPa and $\sigma_{mod,h,min}$ = 38 MPa at the fracture tip). The calculated injection rate was 0.0225*h m^3/s, where h is the fracture height.

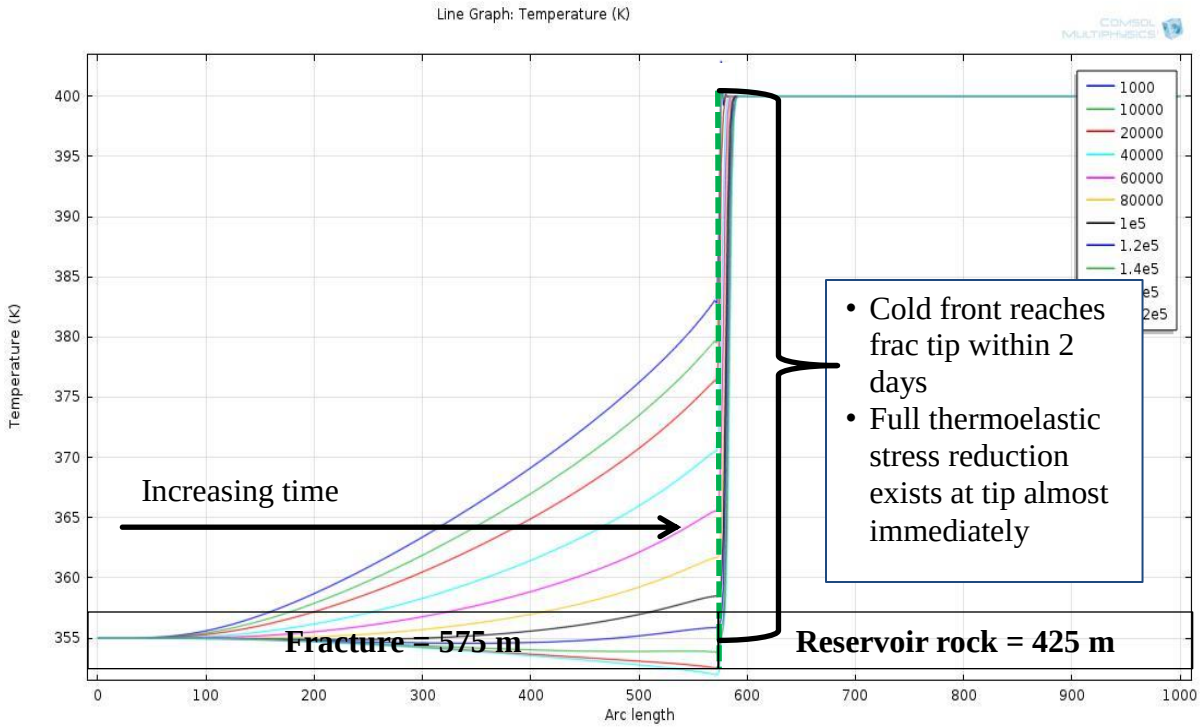

Figure 27: Temperature inside the fracture at the centerline propagates to the tip of the fracture within two days at the conditions of Run 1 (see Table 6); perpendicular propagation into the 64 mD reservoir (not shown) is much slower. The legend indicates the elapsed time in seconds.

The resulting pressure profile in the reservoir in this run is portrayed in Figure 28. The fracture equilibrium length is sensitive to the prescribed pressure boundary condition and its distance from the fracture, i.e. to the pressure gradient (*dP/dy*) in the reservoir. For example, setting a far field reservoir pressure at 31 MPa 200 m away perpendicular to the fracture (as done in this case) results in an equilibrium fracture length (575 m) that is shorter than the equilibrium fracture length when the boundary is set one kilometer away at the same pressure. If the reservoir pressure boundary is at one kilometer instead of 200 m, *dP/dy* is 80% smaller, and the equilibrium fracture length is 223% longer (1303 m versus 575 m). This analysis used plausible boundary conditions (constant 31 MPa

pressure and 400 K external temperature), but the model described herein can be used with other boundary conditions possible in real storage reservoirs. To understand the effect of the pressure boundary conditions (which govern *dP/dy*) on the pressure gradient in the fracture (*dP/dx*) and therefore the equilibrium fracture length, further runs were made at different boundary pressures: Runs 8 and 9, discussed later in this chapter.

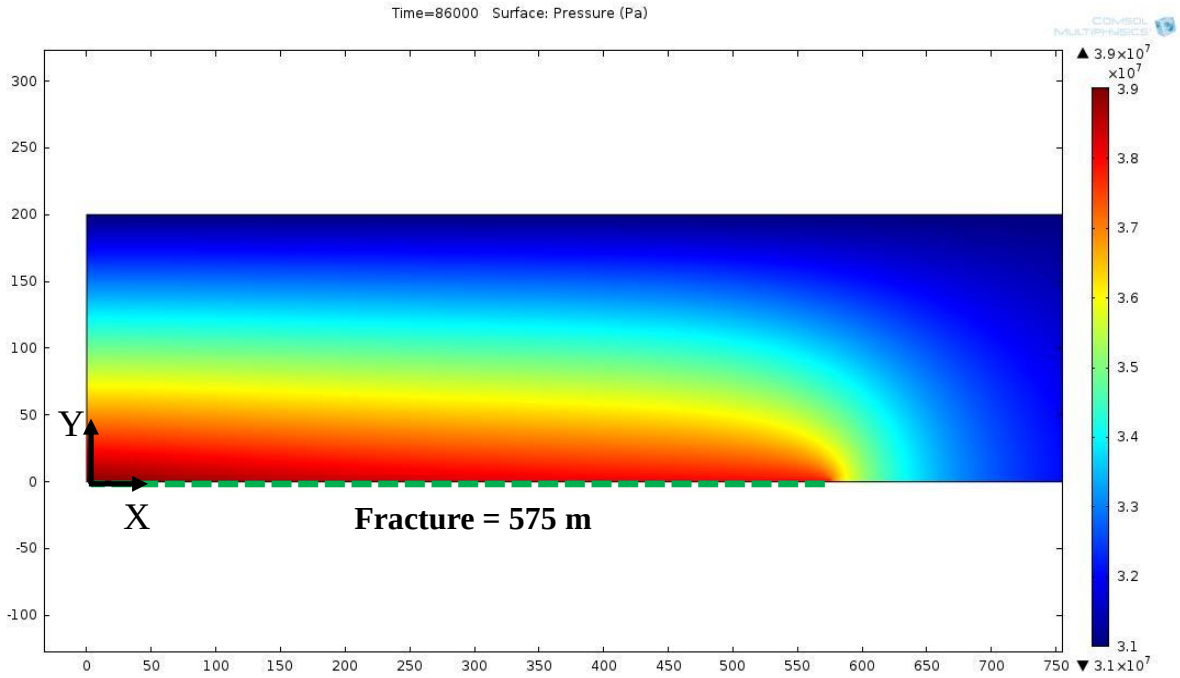

Figure 28: Pressure profile in reservoir at the conditions of Run 1 (see Table 6), typical of all the runs with the same boundary conditions and with constant fluid density and viscosity.

The temperature profiles in Figure 27 show a dip below 355 K once the temperature front reaches the tip of the fracture at 575 m (at times $1.4*10^5$, $1.6*10^5$ and $1.72*10^5$ s). That result is not physically possible and is caused by numerical instability in the COMSOL solver due to the very thin fracture. To demonstrate the validity of the solver regardless of this instability, the fracture width was increased to 5 m. The resulting

temperature profile in the fracture is show in Figure 29. COMSOL was able to accurately calculate the temperature profiles in the larger fracture geometry, with no numerical instability, validating the underlying setup of the system and numerical solver.

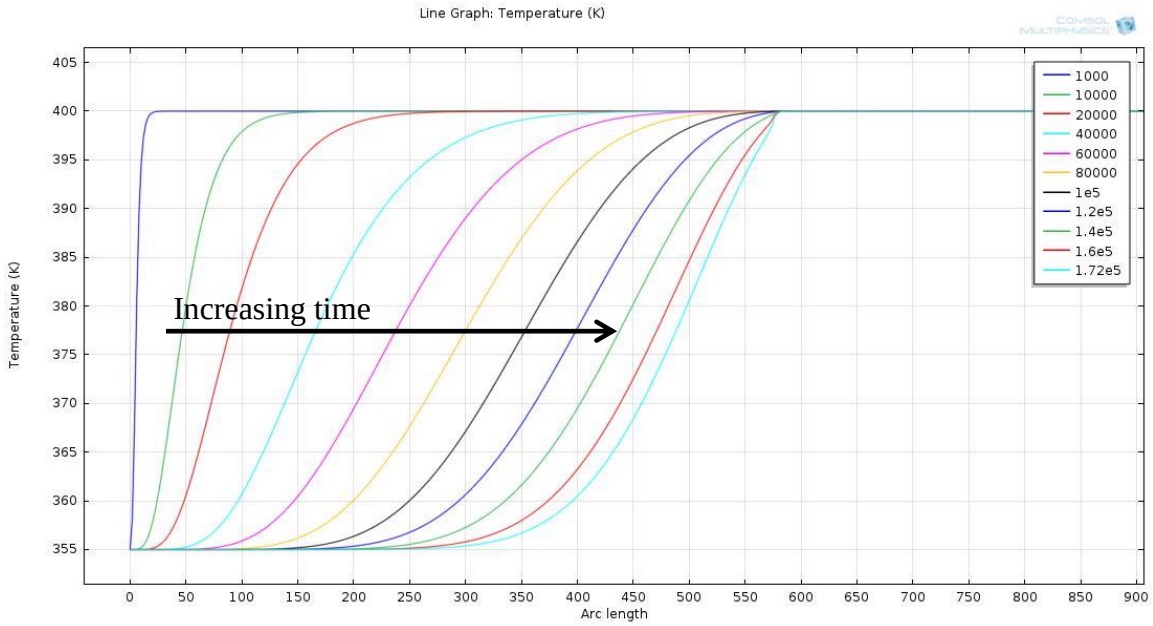

Figure 29: Temperature profile at the elapsed times shown in the legend, in the fracture at the centerline at the conditions of Run 1. The model has a 5 m wide fracture instead of 0.005 m; other properties are as in the Run 1 base case. This graph demonstrates the accuracy of the numerical solver in COMSOL (which was in doubt due to the solution plotted in Figure 26), and its stability when the fracture is not extremely thin relative to the reservoir domain, which is 200 m wide.

5.2 Run 2: System Fluid with a Viscosity of Water

The second run used all the same conditions as the first, except with the single adjustment to the viscosity of the fluid in the system (the injected and in-situ reservoir fluids were identical and had constant properties regardless of temperature and pressure variations as stated in Table 6). In Run 1 the fluid viscosity was $6.36*10^{-5}$ Pa-s throughout the system, mimicking CO_2 at the average pressure and temperature of the system. In Run 2 the fluid viscosity was $2.9*10^{-4}$ Pa-s, approximately the viscosity of

water at the average temperature and pressure of the system. There was no effect on the fracture equilibrium length, as shown in Figure 30. The only difference as compared to the first run was the calculated injection rate of 0.0049 m^3/s per meter of fracture height, which was smaller than in Run 1. For fixed pressure boundaries and incompressible fluid, fluid viscosity does not affect the fracture length as long as it is constant everywhere in the system. Darcy's Law indicates the injection rate is inversely proportional to the viscosity as confirmed by comparing V_{inj} for Runs 1 and 2.

The lower injection rate also resulted in a slower temperature front in the fluid in the fracture as depicted in Figure 31. At two days of injection, the ΔT of 45 K (where the thermoelastic stress is greatest) reaches only about 100 m down the fracture. At the lower injection rate the fracture would propagate proportionately more slowly than in the base case. The thermal front would take about 11.5 days to reach the equilibrium length. Relative to the lifetime of the injection well this is rapid, and thus rapid fracture propagation to the equilibrium length would occur.

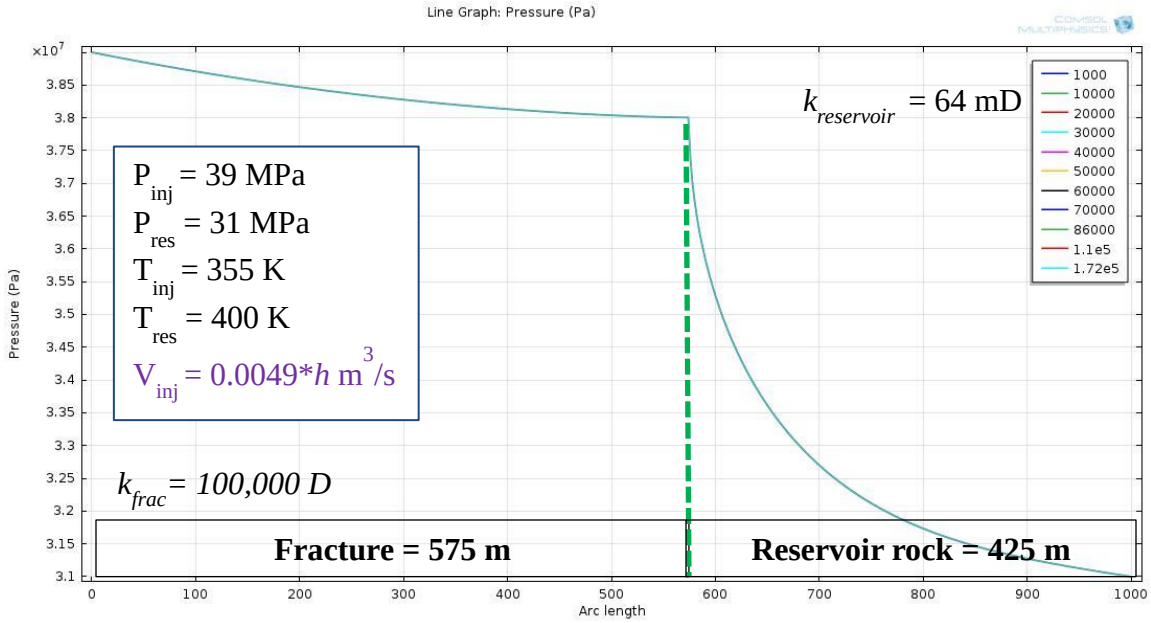

Figure 30: Pressure inside the fracture at the centerline and in the reservoir rock beyond the fracture tip in the same plane as the fracture, at the conditions of Run 2 (see Table 6). The legend indicates the elapsed time in seconds, up to two days of injection. The calculated volumetric injection rate is 0.0049 m^3/s per meter of fracture height *h*.

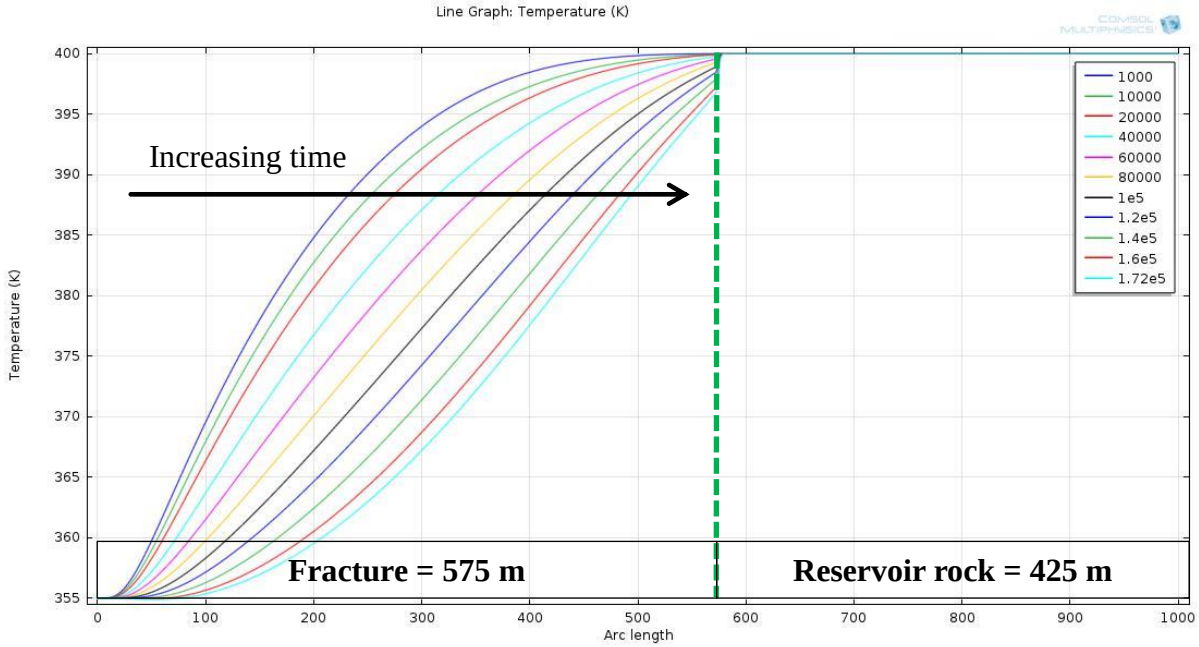

Figure 31: Temperature profile in the fracture at the centerline at the conditions of Run 2 (see Table 6). Notice the velocity of the temperature front is much slower when high viscosity ($2.9*10^{-4}$ Pa-s) fluid is injected than in the base case (Figure 26) reaching only about 100 m down the fracture at two days of injection.

5.3 Run 3: Further Fluid Viscosity Sensitivity

Run 3 tested another value of fluid viscosity $1*10^{-3}$ Pa-s in the system (an identical and constant property in the injected fluid in the fracture and in the fluid originally in the reservoir) and its effect on fracture equilibrium length and injection rate. All other properties were the same as in Run 1 (see Table 6). As in the previous run the fracture length was unchanged and the injection rate decreased from 0.0049 to 0.0014 m^3/s per meter of fracture height as portrayed in Figure 32. The temperature front in the fracture shown in Figure 33 therefore only traveled about 20 m at two days of injection, meaning the fracture propagation rate would be smaller than in Runs 1 and 2. Even so, the temperature front will reach the equilibrium length within a few weeks, and the equilibrium length is thus expected to be a good approximation of the actual length. This run confirmed the temperature front speed in the fracture is heavily dependent on injection rate, and therefore fluid viscosity. Figure 34 shows the relationship between viscosity and injection rate of this system where all geometric, fluid, and boundary parameters are constant.

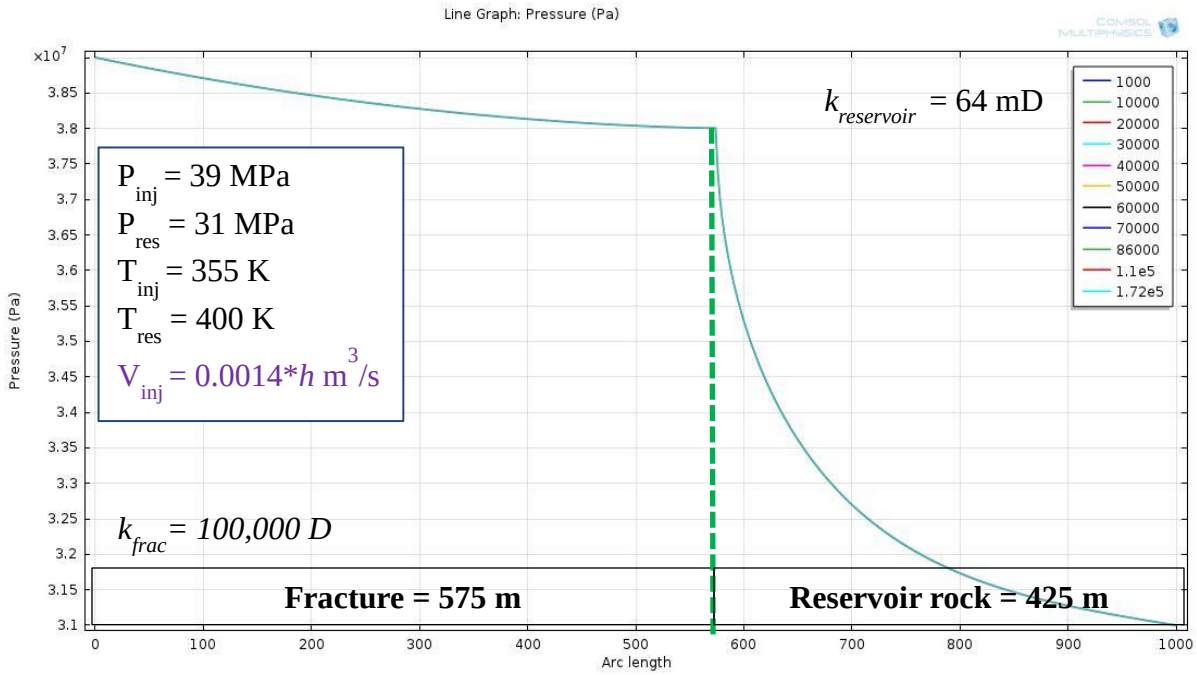

Figure 32: Pressure inside the fracture at the centerline and in the reservoir rock beyond the fracture tip in the same plane as the fracture, at the conditions of Run 3 (see Table 6). The legend indicates elapsed time in seconds, up to two days of injection. The volumetric injection rate is 0.0014 m^3/s per meter of fracture height *h*.

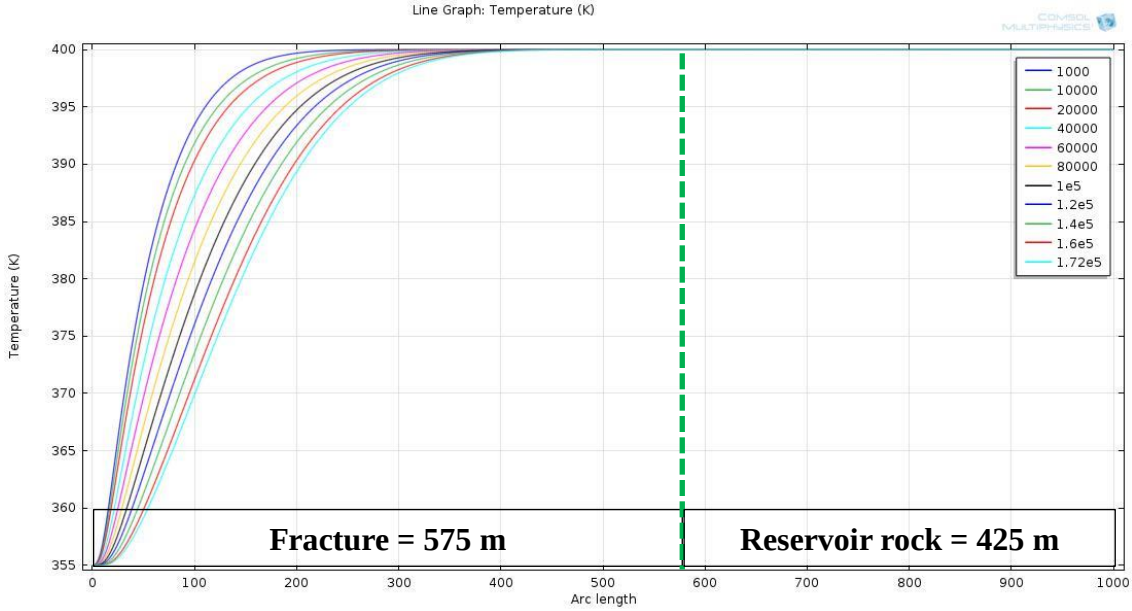

Figure 33: Temperature profile in the fracture at the centerline after two days of injection at the conditions of Run 3 (see Table 6). Notice at the lower injection rate in this run of 0.0014 m^2/s versus 0.0225 m^2/s in the base case causes the temperature front to only travel about 20 m down the fracture after two days.

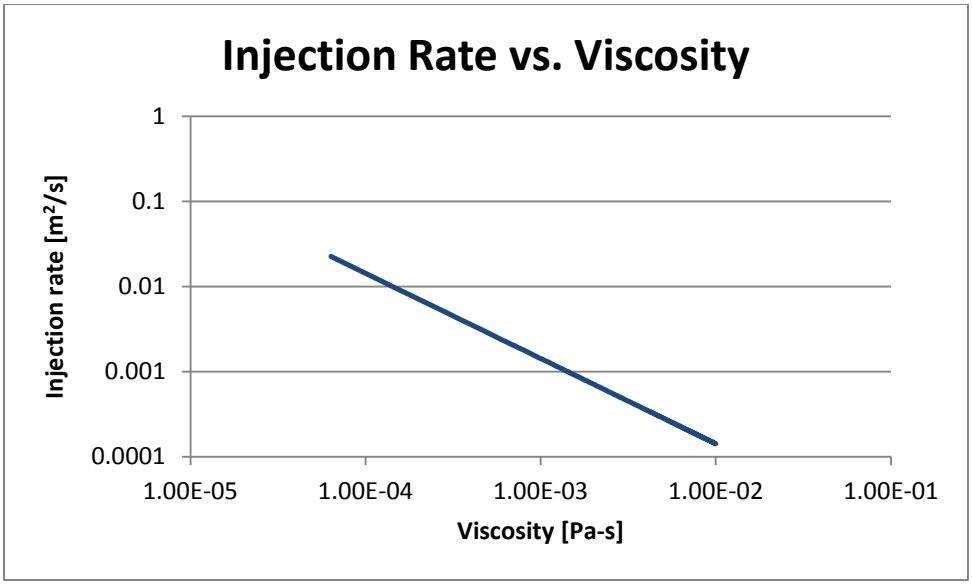

Figure 34: Injection rate into the fractured reservoir versus the viscosity of the fluid (assumed the same for injected and the in-situ reservoir fluid) for Runs 1, 2, 3 and another not shown here. The trend confirms that for fixed pressure boundaries and constant fluid properties in the domain, viscosity determines the flow rate but has no effect on the equilibrium fracture length.

5.4 Run 4: System Fluid with a Density of Water

Run 4 tested the sensitivity of the fracture length to the density of the fluid, 970 kg/m³ instead of 720 kg/m³ in Run 1. The fluid density was the same in the reservoir as in the fluid injected into the fracture. All other parameters were the same as in Run 1 (see Table 6). The fluid density affects the rate of heat transfer between the fluid and reservoir and thus could affect the temperature profile and the thermoelastic stress. However, the simulation showed only a small change in the temperature profile in Figure 36 and no change in the fracture equilibrium length in Figure 35.

Since the fluid density had no effect on equilibrium fracture length, it did not affect the injection rate of the reservoir since the boundary conditions and system

geometry did not change. This is because Darcy's Law indicates flow rate is independent of the fluid density, and if the fluid is incompressible the pressure gradients (*dP/dy* and *dP/dx*) are also independent of the fluid density. Given the high velocity of the fluid in the fracture, and the low heat conduction rate from the reservoir, the temperature profile in the fracture is only slightly changed from Run 1, i.e. this system is thermally convection dominated. The injection rate would have to be very low, or the heat capacity very low, for the fluid to warm significantly before reaching the fracture tip. Even at realistic injection rates (i.e. 550 kg/min or 0.0127 m^3/s as in the Cranfield pilot storage program [24]), as described by the thermal Peclet number of $230*10^6$ for the Cranfield injection rate and field conditions, the temperature front movement is convection dominated. The full thermoelastic stress reduction would thus be continuously applied to the tip of the fracture during injection. Therefore the fracture lengths calculated by COMSOL are realistic despite the relatively larger injection rates than could be achieved in the field.

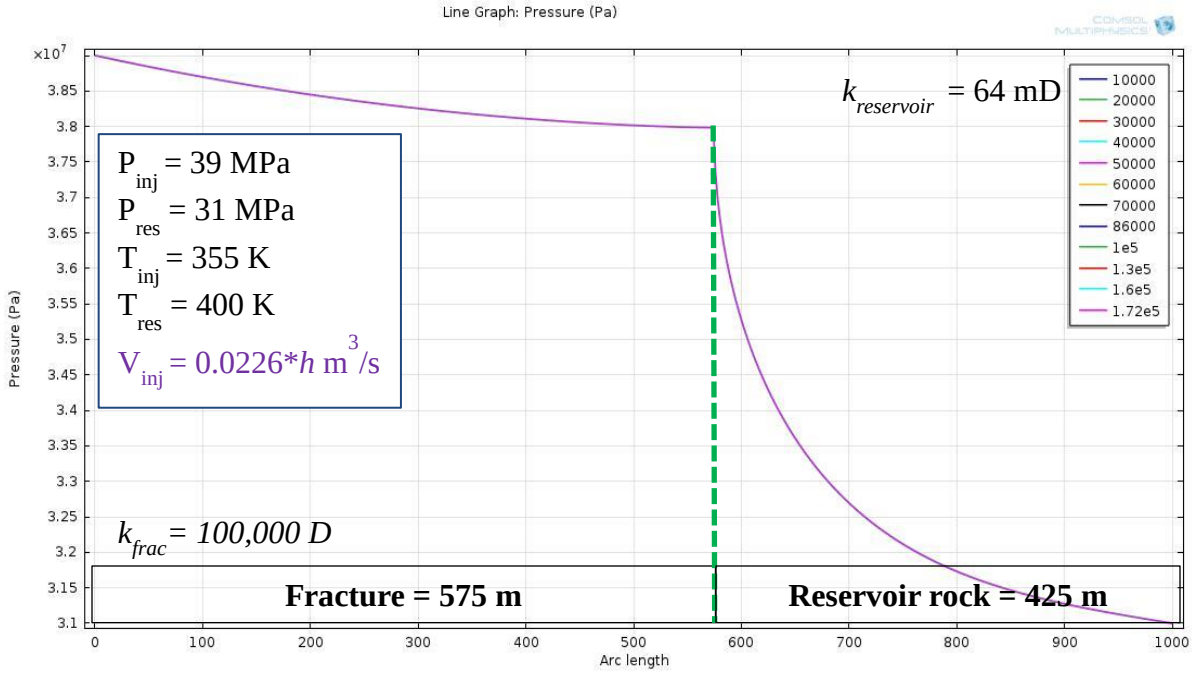

Figure 35: Pressure inside the fracture at the centerline and in the reservoir rock beyond the fracture tip in the same plane as the fracture, at the conditions of Run 4 (see Table 6). The legend indicates the elapsed time in seconds, up to two days of injection. Notice the pressure profile and injection rate are equal to those in Run 1 as the density change (720 kg/m^3 to 970 kg/m^3) had no effect with the fixed pressure boundaries.

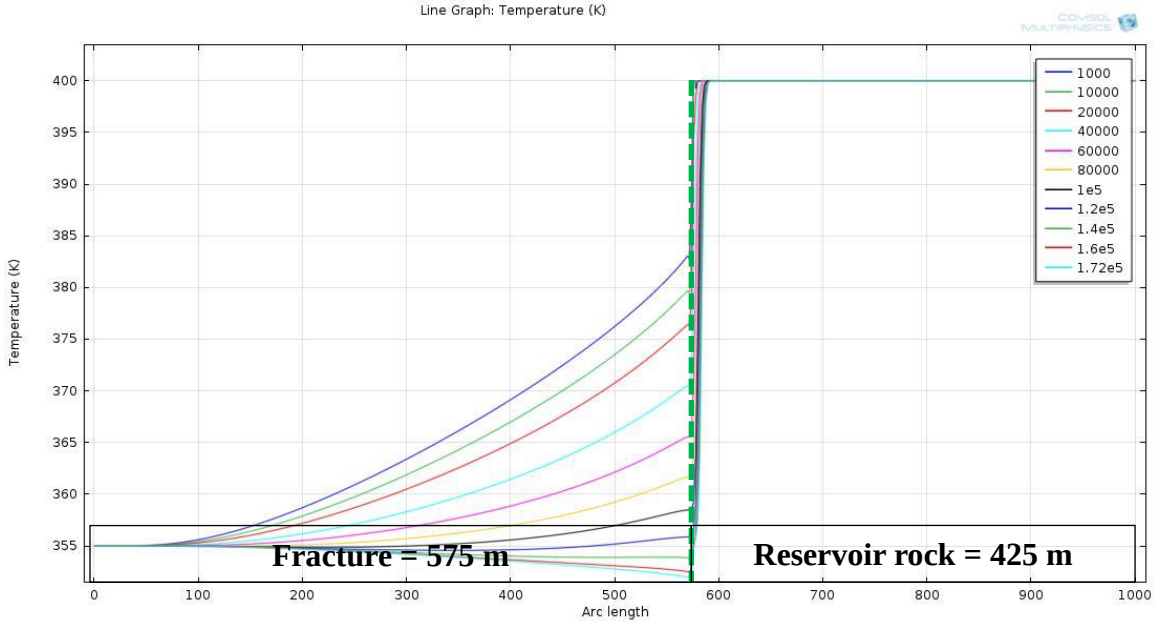

Figure 36: Temperature profile in the fracture at the centerline at the conditions of Run 4 (see Table 6). The injection rate is the same as in Run 1, and the inlet fluid temperature also arrives at the fracture tip within two days for the reasons discussed in the text.

5.5 Run 5: System Fluid with a Heat Capacity of Water

Run 5 tested the sensitivity of the thermal front velocity to the heat capacity of the fluid used in the system which was constant and identical in the injected fluid and in the fluid originally in reservoir. In this run the heat capacity was raised to 4142 J/kg-K (compared to the value of 1850 J/kg-K from Run 1), similar to water at these temperatures and pressures. All other variables were the same as in Run 1 (see Table 6). The result of these conditions was a fracture of equivalent length of 575 m as in Run 1 because the pressure gradients are independent of heat capacity (see Figure 37); however the thermal front reached the tip of the fracture in $6*10^4$ s instead of $1.2*10^5$ s (see Figure 38), in half the time of the Run 1. This was expected as this heat capacity is about double that in Run 1, so applying the same amount of heat flux to the fluid results in only half the increase in temperature. Conversely if the heat capacity were halved, the temperature front would reach the fracture tip in twice the time of Run 1. Injectivity was unchanged as this too is independent of heat capacity for fixed pressure conditions.

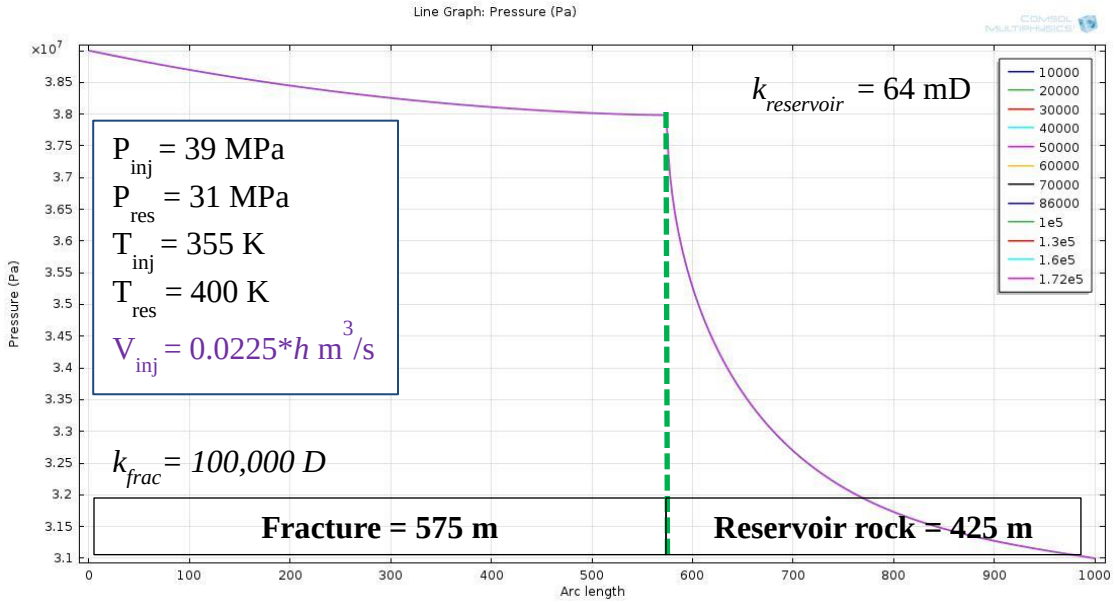

Figure 37: Pressure inside the fracture at the centerline and in the reservoir rock beyond the fracture tip in the same plane as the fracture - conditions of Run 5 (see Table 6). The legend indicates the elapsed time in seconds, up to two days of injection. The heat capacity has no effect on the pressure profile in the fracture resulting in a fracture equilibrium length identical to Run 1.

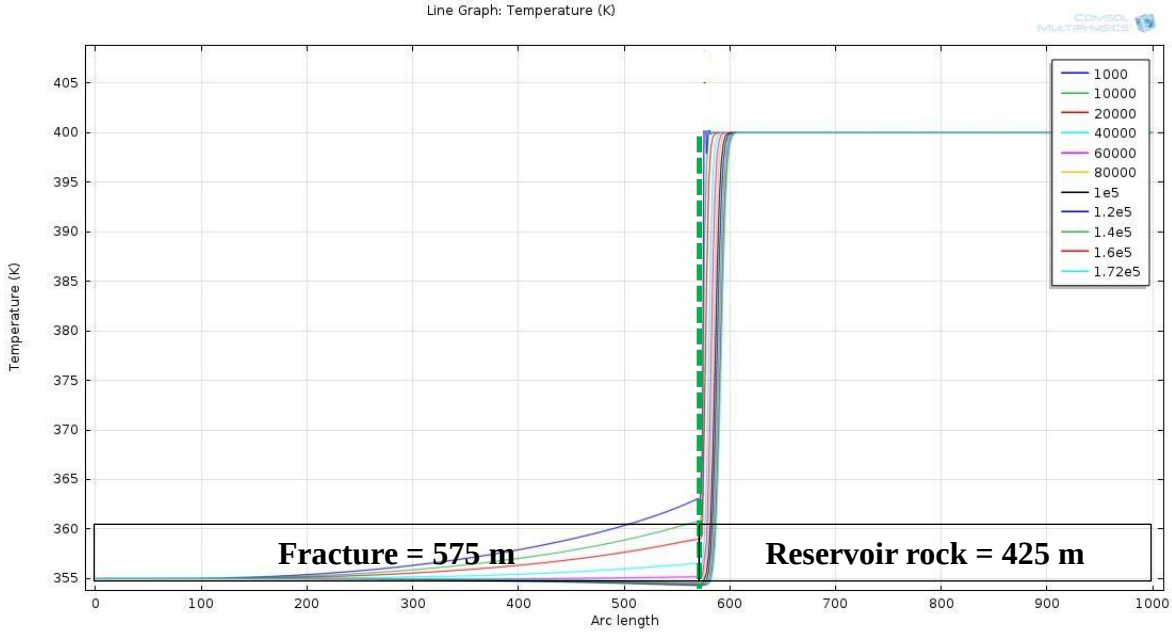

Figure 38: Temperature profile in the fracture at the centerline at the conditions of Run 5 (see Table 6). Notice the thermal front reaches the fracture tip within one day of injection when the heat capacity is 4142 J/kg-K instead of the two days seen of Run 1 where the heat capacity of the fluid was 1850 J/kg-K.

5.6 Run 6: Reservoir Permeability of 1000 mD

Run 6 involved injecting the same constant-property fluid as in Run 1 into a reservoir of higher permeability of 1000 mD instead of 64 mD (see Table 6). All other properties were equivalent to those in Run 1. The higher permeability reservoir enhanced flow into the reservoir from the fracture, thereby increasing the pressure gradient in the fracture (*dP/dx*) resulting in a shorter equilibrium length as shown in Figure 40 (150 m versus 575 m). The larger permeability reservoir also resulted in a larger injection rate: 0.13 m^3/s versus 0.0225 m^3/s per meter of fracture height. This confirmed Prats' correlation, Equation 7 and Figure 12. Runs 1 and 6 have the same geometry and boundary conditions, and from Darcy's Law wherein flow rate is proportional to permeability of the porous media, the injectivity of the reservoir was expectedly larger. However, the flow rate does not increase in proportion to the reservoir permeability. This is because the injectivity of the formation is a strong function of fracture length as well as reservoir permeability, not reservoir permeability alone.

Given the higher injection rate and shorter fracture than in Run 1, the temperature front of cold fluid arrives at the fracture tip in less than 10000 s (see Figure 41). The cold front extending into the reservoir as shown in Figure 39 due to convection also reduced conductive heat flux into the fluid in the fracture, effectively insulating the fracture fluid more than in the low permeability case where less cold fluid invaded the reservoir. Fractures growing in high permeability reservoirs are thus expected to grow faster as the cold front geometry is closer to radial at all times and travels faster through the reservoir, as is depicted in Figure 39 for this run. The more radial geometry holds the $\Delta\sigma_T$

(Equation 11) near its maximum instead of a lower value induced by a front between elliptical and radial geometries, as seen in the low permeability cases.

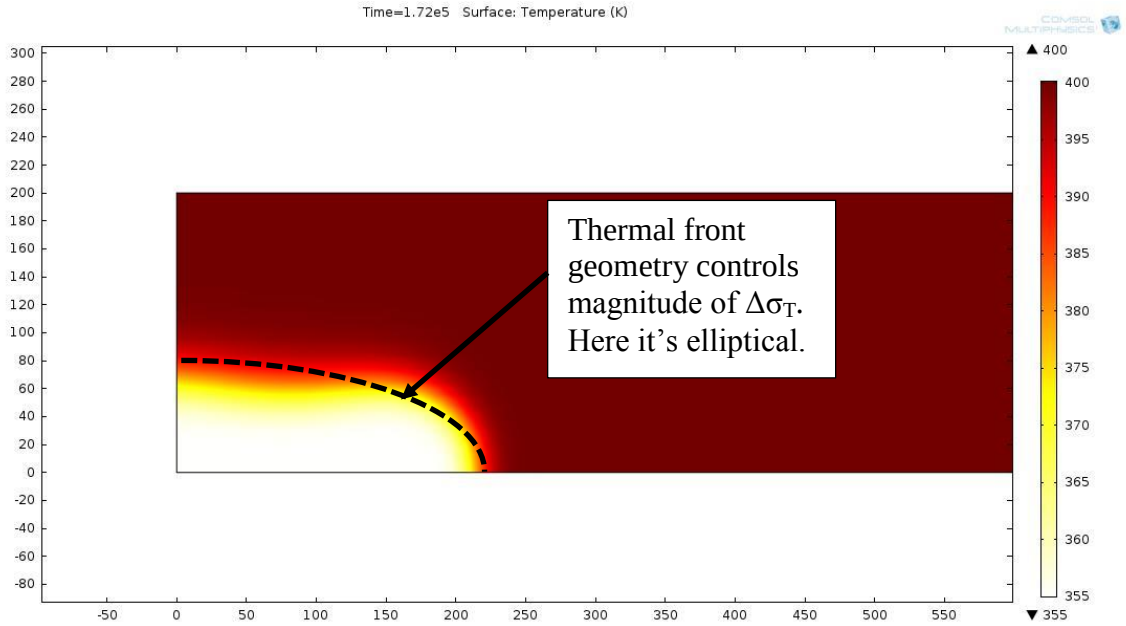

Figure 39: Temperature front extending into the reservoir at two days of injection for Run 6. The temperature front geometry is elliptical, but more radial, in the high permeability case (Run 6) producing a larger $\Delta\sigma_T$ than in the low permeability case (Run 1) due to the shape factor component of the $\Delta\sigma_T$ as described by Equation 11. This would result in faster fracture propagation.

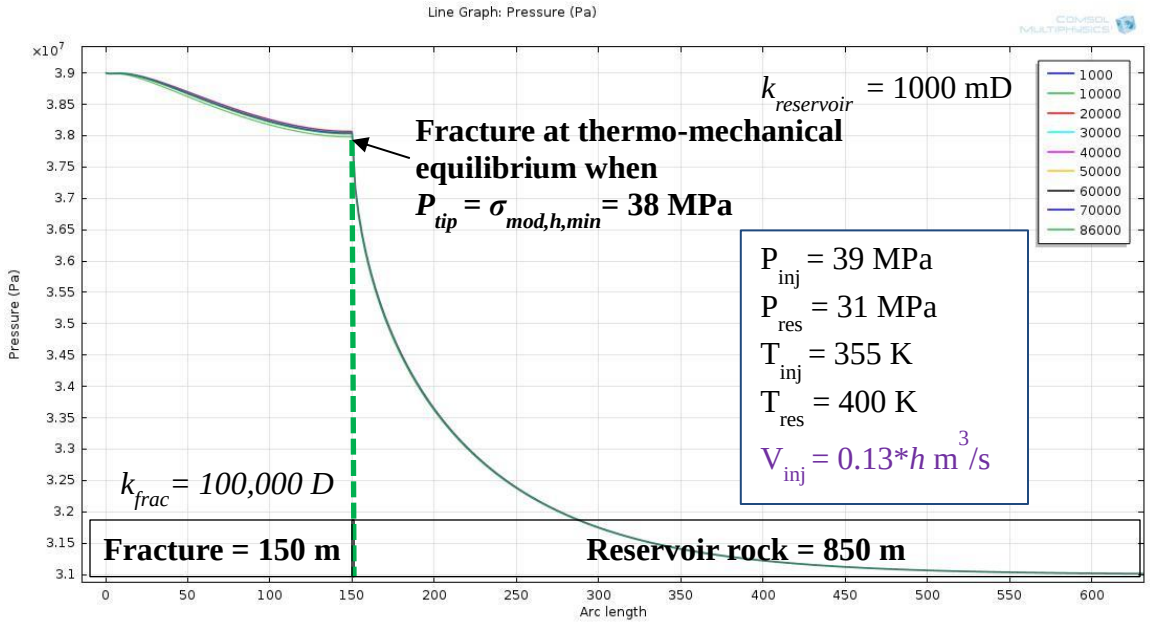

Figure 40: Pressure inside the fracture at the centerline and in the reservoir rock beyond the fracture tip in the same plane as the fracture, at the conditions of Run 6 (see Table 6). The legend indicates the elapsed time in seconds. The higher permeability reservoir in this case (1000 mD versus 64 mD in Run 1) increased the injection rate from 0.0225 m^3/s to 0.13 m^3/s per meter of fracture height.

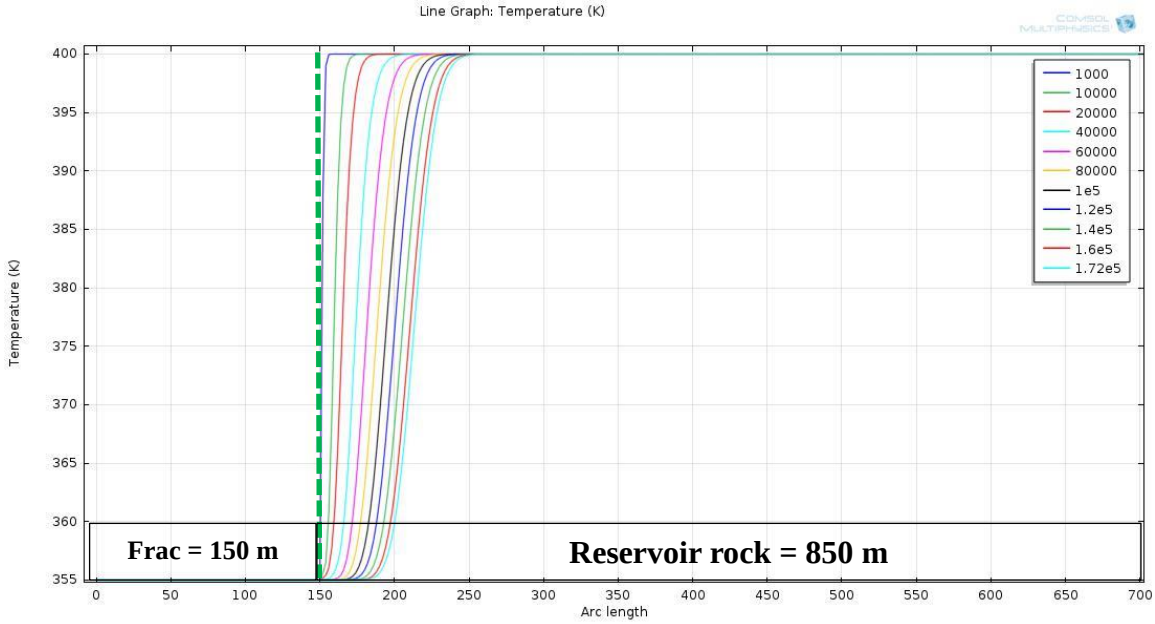

Figure 41: Temperature profile in the fracture at the centerline at the conditions of Run 6. In this high permeability case the thermal front extends almost 50 m ahead of the fracture tip within two days of injection, as compared to Run 1 where the temperature front reached the fracture tip in 1.2*10^5 s.

5.7 Run 7: Fracture Permeability of 10,000 D

Run 7 illustrated the impact of fracture permeability on fracture equilibrium length. Fracture permeability is proportional to its width and thus is heavily dependent on the net pressure in the fracture and the mechanical rock properties. This parameter is extremely difficult to determine in the field especially at any appreciable depth into the reservoir. The PKN derivation for fracture width describes a fracture cross-section in the horizontal plane. The width is a maximum at the wellbore and zero at the tip. Typically in the petroleum industry a fracture of tapering width is described by a single value of average permeability, a method that was used in this thesis. However, assuming a constant width for the entire length of the fracture (and thus constant permeability) will lead to an overestimation of equilibrium fracture length because the pressure gradient *dP/dx* is constant, instead of increasing toward the tip of a tapering fracture. In this thesis a constant width fracture was prescribed for computational simplicity, but multiple runs were made at different permeabilities to determine that parameter's influence on equilibrium fracture length.

This run used a fracture of 10,000 D, resulting in a shorter fracture (160 m; see Figure 42) than the 100,000 D case from Run 1 (575 m). All other system parameters were the same as in Run 1 (see Table 6). Lower fracture permeability causes the fracture pressure gradient (*dP/dx*) to increase due to the increased resistance to flow, also predicted by Prats' correlation. The flow resistance also decreased the injection rate by two-thirds as compared to Run 1 (0.008 m^3/s per meter of fracture height as compared to 0.0225 m^3/s). Building on the results from Run 6, Run 7 indicated the injection rate is a

function of the reservoir permeability, fracture permeability and fracture length. The lower injection rate caused the thermal front to reach the fracture tip in a little over one day of injection, a velocity of about 160 m/day, as opposed to the velocity of the front in Run 1 which was about 290 m/day (see Figure 43).

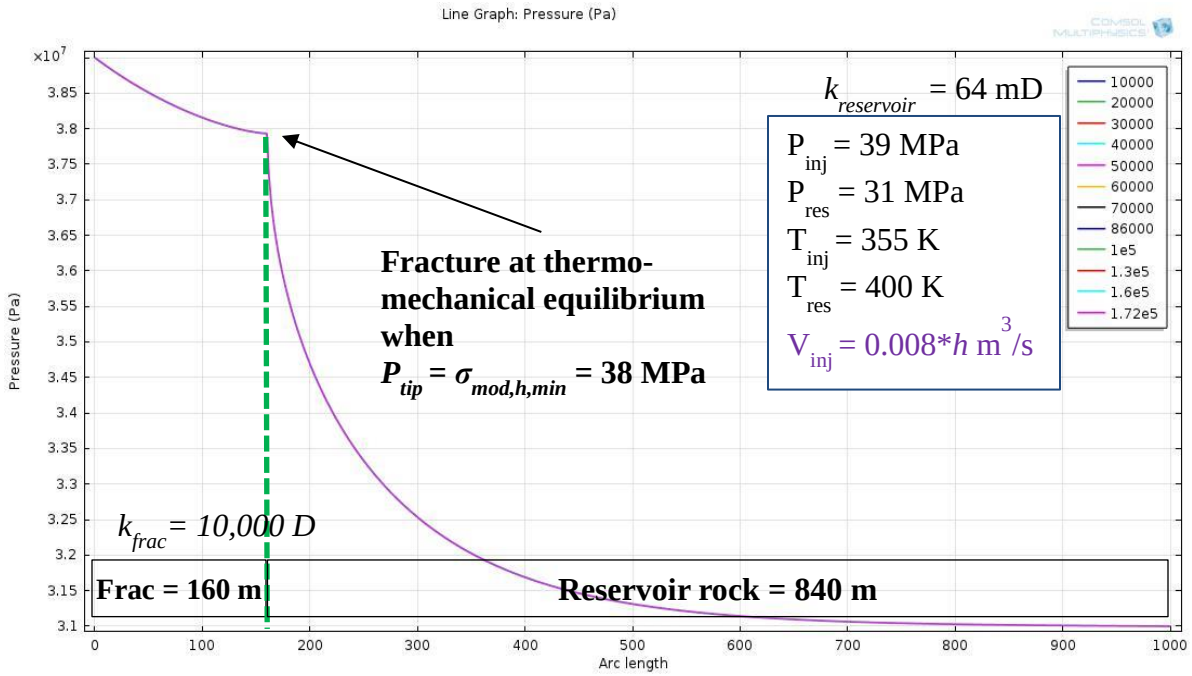

Figure 42: Pressure inside the fracture at the centerline and in the reservoir rock beyond the fracture tip in the same plane as the fracture, at the conditions of Run 7 (see Table 6). The legend indicates the elapsed time in seconds, up to two days of injection. Due to the lower permeability fracture (10,000 D in this run instead of 100,000 in Run 1) the fracture equilibrium length is 160 m instead of 575 m- reasons further discussed in the text. The injection rate also decreased from 0.0225 m^2/s in Run 1 to 0.008 m^2/s in Run 7.

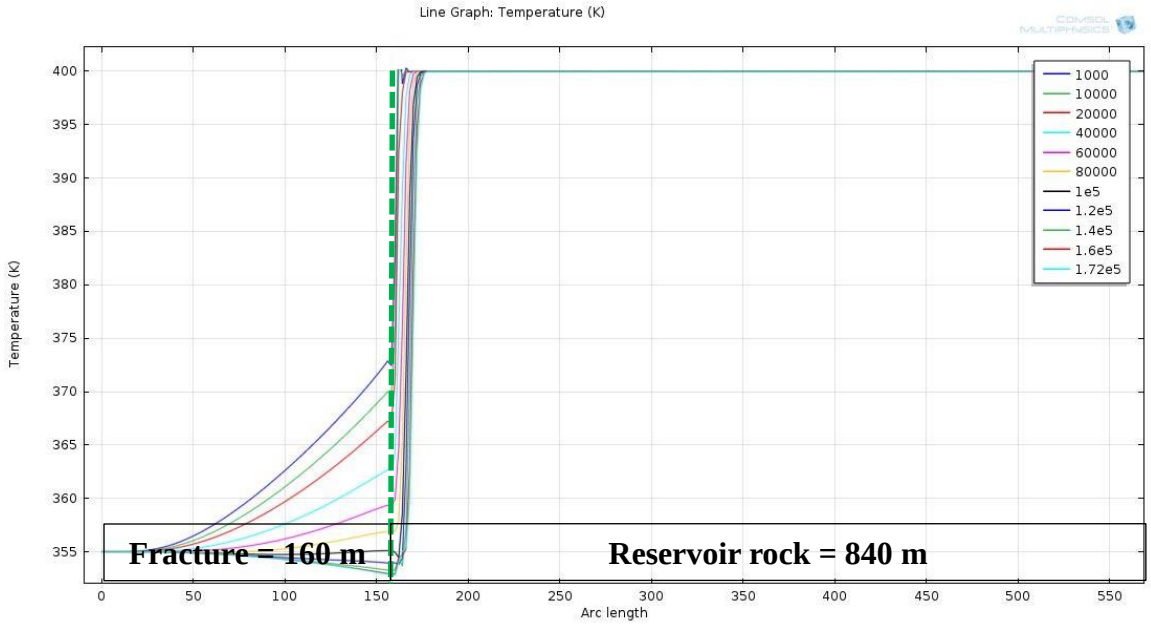

Figure 43: Temperature inside the fracture at the centerline and in the reservoir rock beyond the fracture tip in the same plane as the fracture, at the conditions of Run 7 (see Table 6). The lower injection rate and increased flow resistance of the lower permeability fracture (10,000 D in this run versus 100,000 D in Run 1) caused the thermal front to reach the tip in about 95000 s, despite the shorter length.

5.8 Run 8: 35 MPa Boundary

The purpose of Run 8 was to explore the effect of the boundary pressure on fracture length. All system parameters were the same as in Run 1 except the boundary pressure was 35 MPa instead of 31 MPa (see Table 6). As previously stated, one method of reservoir pressure control could be to produce brine from an aquifer at the same rate as CO_2 is injected. However, in the event the far-field reservoir pressure increases during injection, it could have an undesirable effect on the fracture length. Figure 44 shows the effect of a 35 MPa boundary pressure, leading to a fracture length of 880 m, longer than the 575 m with a 31 MPa boundary. A higher boundary pressure results in a smaller

pressure gradient *dP/dy* in the reservoir, decreasing flow out of the fracture and reducing the internal pressure gradient *dP/dx*.

The injection rate of the reservoir declined from 0.0225 m^2/s in Run 1 to 0.0152 m^2/s in this run. The Cranfield pilot storage data indicated an injection rate of around 0.0127 m^3/s into a 25 m tall storage reservoir (or $5*10^{-4}$ m^2/s) indicating the pressure gradient in that field case was smaller than in either Run 1 or Run 8. As was alluded to in Section 5.1, the injection rates calculated by COMSOL in this thesis are overestimates of truly attainable injection rates due to the larger pressure gradients (*dP/dy*) and neglect of relative permeability effects. For smaller pressure gradients in the formation (as in this run) it is apparent the equilibrium fracture length is significantly larger. Thus at realistic field pressure gradients, mobilities and injection rates the equilibrium fracture length would be longer.

Comparing the injectivity of Run 1 to 8 as per Equation 25, Run 1 had an injectivity of 0.0028 $m^3/s/MPa$ (per meter of fracture height) and Run 8 had an injectivity of 0.0038 $m^3/s/MPa$. Thus higher pressure at the outlet boundary had two effects: it increased the equilibrium length of the fracture, and it enhanced the injectivity of the reservoir but at a smaller total injection rate. The longer fracture created a larger surface area for fluid to enter the reservoir (53% more in Run 8 than in Run 1), but flow was driven by a smaller *dP/dy* (50% less in Run 8 than in Run 1). The ratio of injection rate in Run 8 to Run 1 was about 0.68; the ratio of the fracture length-pressure gradient product (X_f*dP/dy) for Run 8 to Run 1 was about 0.70. This indicates that injection rate scales with the pressure gradient times the fracture length (or surface area when extrapolated to

two dimensions by multiplying the length of the fracture times the reservoir height), as would be expected from Darcy's Law.

A longer fracture and a smaller injection rate led to a slower thermal front advancement rate in the fracture as well, as is seen in Figure 45. The thermal front did not reach the fracture tip after two days of injection; extrapolating the thermal front velocity the full ΔT would reach the tip in about 4.5 days.

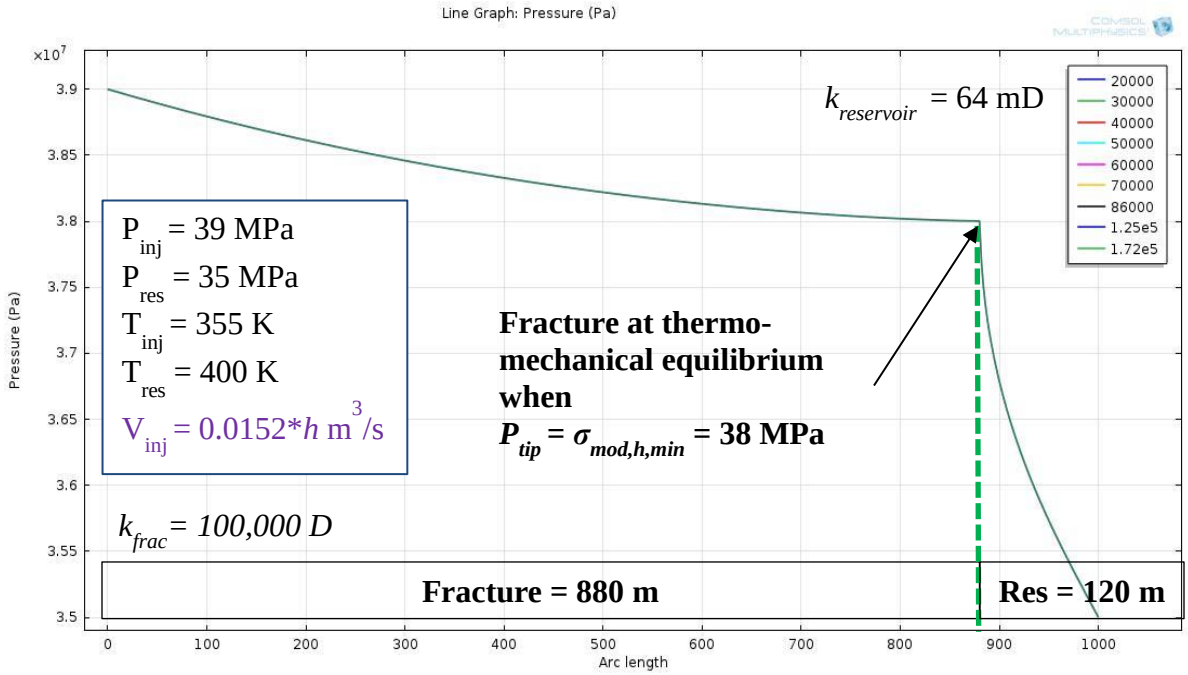

Figure 44: Pressure inside the fracture at the centerline and in the reservoir rock beyond the fracture tip in the same plane as the fracture, at the conditions of Run 8 (see Table 6). The legend indicates the elapsed time in seconds, up to two days of injection. The equilibrium fracture length in this run was 880 m, as compared to 575 m in Run 1 due to the higher boundary pressure, 35 MPa versus 31 MPa.

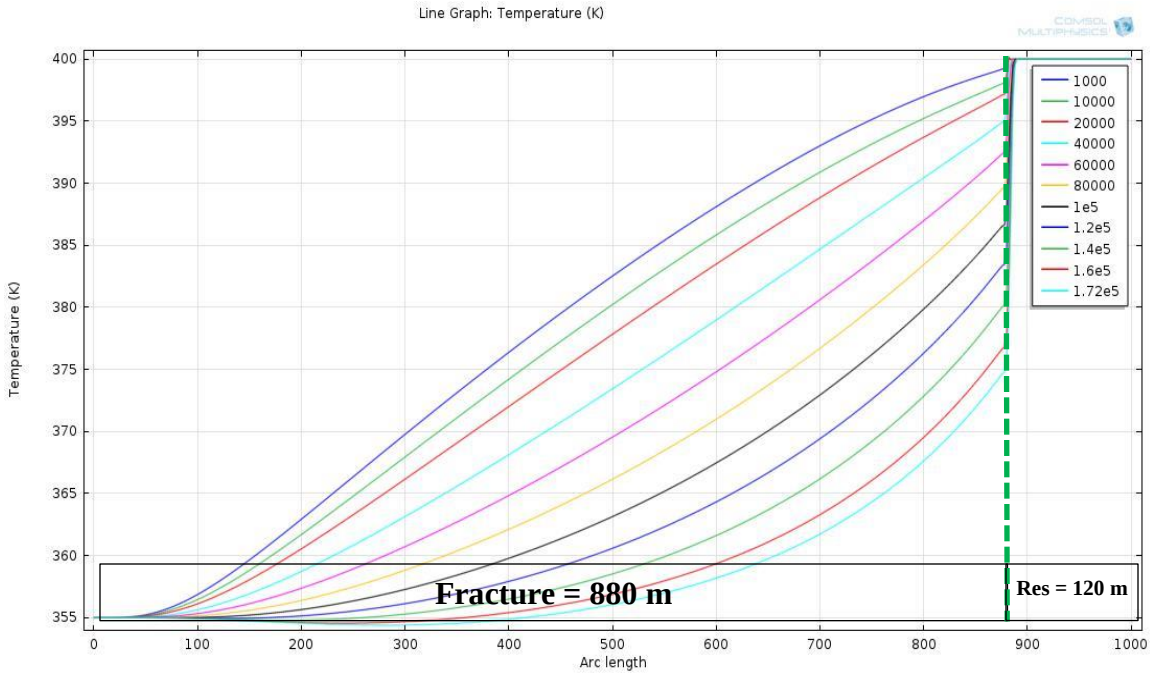

Figure 45: Temperature in the fracture at the centerline over two days of injection at the conditions of Run 8 (see Table 6). The result of a long fracture and low injection rate is a much slower thermal advancement, which is expected to reach the fracture tip in 4.5 days as compared to two days in Run 1. Relative to the lifetime of an injection well this is still quite fast.

5.9 Run 9: Boundary Sensitivity of 37 MPa

Run 9 was another sensitivity analysis on the boundary pressure, set to 37 MPa. A fracture length of 1000 m (equal to the length of the porous medium used in the simulation) would still have a pressure at the fracture tip greater than the fracture equilibrium pressure as illustrated in Figure 46 where the tip pressure was over 38.4 MPa at 900 m. In order to maintain a consistent domain size for all the runs, the equilibrium fracture length was simply stated as greater than 1000 m. The analytical solution for fracture equilibrium length gives 1408 m, confirming the predicted results from COMSOL. The analytical solution and its agreement with the numerical solution will be discussed in Section 5.12

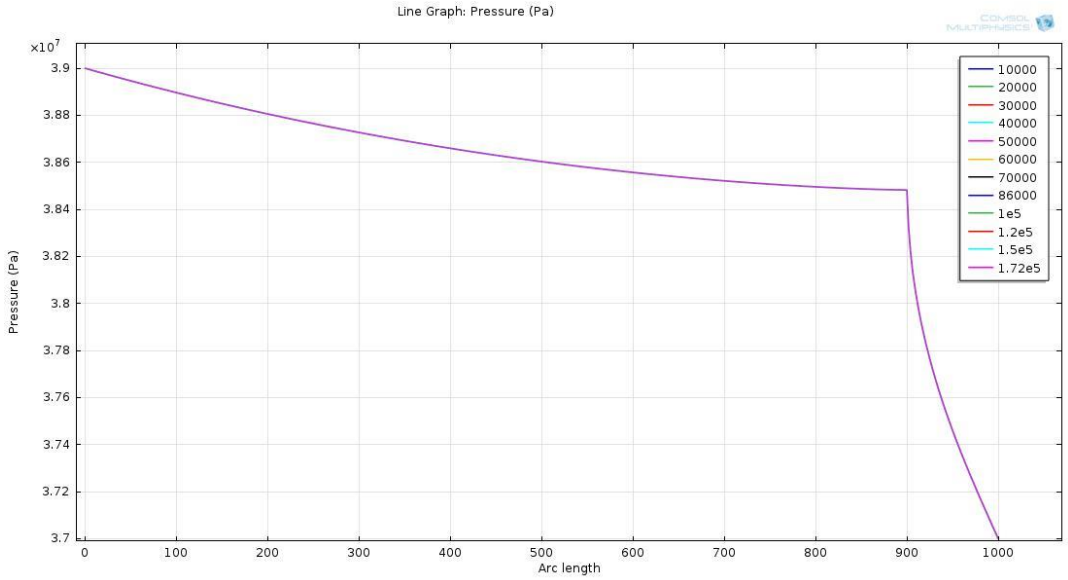

Figure 46: Pressure inside the fracture at the centerline and in the reservoir rock beyond the fracture tip in the same plane as the fracture, at the conditions of Run 9 (see Table 6). The legend indicates the elapsed time in seconds, up to two days of injection. The pressure in the fracture tip still exceeds 38 MPa, the criteria for equilibrium, at 900 m. Hence, for the reasons described in the text, the equilibrium fracture length is stated as > 1000 m.

5.10 Run 10: Variable Fluid Viscosity and Density in the System

Run 10 utilized the EOS written in Section 3.3, Equations 22 and 23, to enable COMSOL to calculate the viscosity and density of the injected fluid in the fracture and of the fluid originally in the reservoir. These properties vary with temperature and pressure, and time and location. The fluid heat capacity, thermal conductivity and all other system properties were constant and the same as in Run 1 (see Table 6). At the inlet to the fracture the fluid had a viscosity of about $7.3*10^{-5}$ Pa-s and density of 815 kg/m^3. The fluid originally in the reservoir had a viscosity of $5.4*10^{-5}$ Pa-s and density of about 580 kg/m^3. The intention of this run was to determine the relative mobility effect of a high

viscosity, high density injected fluid displacing a low-viscosity, low-density fluid from the reservoir when a smooth variation in viscosity and density exists.

As portrayed in Figure 8, the density of CO_2 in this system decreases by 30% from injection conditions to reservoir conditions. The viscosity will decrease by about 30% too. Therefore the assumption of constant viscosity and density as in the previous runs was not realistic, except at very late times of injection where the flood and thermal fronts have extended well beyond the fracture. Run 10 differed in that it is more representative of earlier time in a sequestration program. At early time CO_2 has invaded the storage reservoir and the flood front is larger than the temperature front, confocal to the fracture, i.e. the thermal front lags behind the flood front (see Figure 16). In this case, CO_2 ahead of the thermal front will be closer to reservoir temperature and pressure and therefore will have a lower viscosity and density than the fluid in the fracture at injection conditions.

The effect of a high viscosity fluid displacing a low viscosity fluid on the equilibrium fracture length was to shorten it, from 575 m to 490 m (see Figure 47). The viscosity of the fluid in the fracture was about $7.3*10^{-5}$ Pa-s and the viscosity in the reservoir was about $5.4*10^{-5}$ Pa-s. The mobility ratio M as described by Equation 24 is equal to unity when the viscosity of the fluid in the reservoir is equal to the viscosity of the fluid in the fracture, as in Run 1. When the viscosity of the fluid in the reservoir (μ_m) is less than in the fracture (μ_f) M is less than unity, and the effect of this viscosity difference was to shorten the equilibrium fracture length. Therefore fracture equilibrium length is proportional to the mobility ratio μ_m/μ_f and the pressure gradient dP/dx is

inversely proportional to the mobility ratio. In other words, when μ_m is less than μ_f the pressure gradient in the fracture increases. For the inverse case, a scenario where lower viscosity CO_2 is displacing higher viscosity brine, the equilibrium fracture length would consequently be longer.

The injection rate in Run 10 was 0.0228 m^3/s per meter of fracture height, as compared to 0.0225 m^3/s in Run 1- a negligible difference of less than 2%. However, this injection rate is flowing into a fracture 15% shorter, indicating a mobility ratio of less than 1 would enhance the injectivity of a storage reservoir per meter of fracture length.

The speed of the temperature front (as depicted in Figure 48) was about 15% slower, 353 m/day in this run versus 414 m/day in Run 1, which was attributable to the density difference between the runs. The density of the fluid in the fracture in Run 10 was about 13% greater, 815 kg/m^3 in this run versus 720 kg/m^3 in Run 1. Given the same heat capacity and thermal conductivity, an equivalent applied heat flux would predictably raise the temperature in the denser fluid more slowly.

Viscosity and density of CO_2 are strongly dependent on temperature and less on pressure. It is apparent from Figures 49-52 this is true as the density and viscosity profiles directly overlay the area of temperature change in the matrix, a thin region due to the short simulated interval of time.

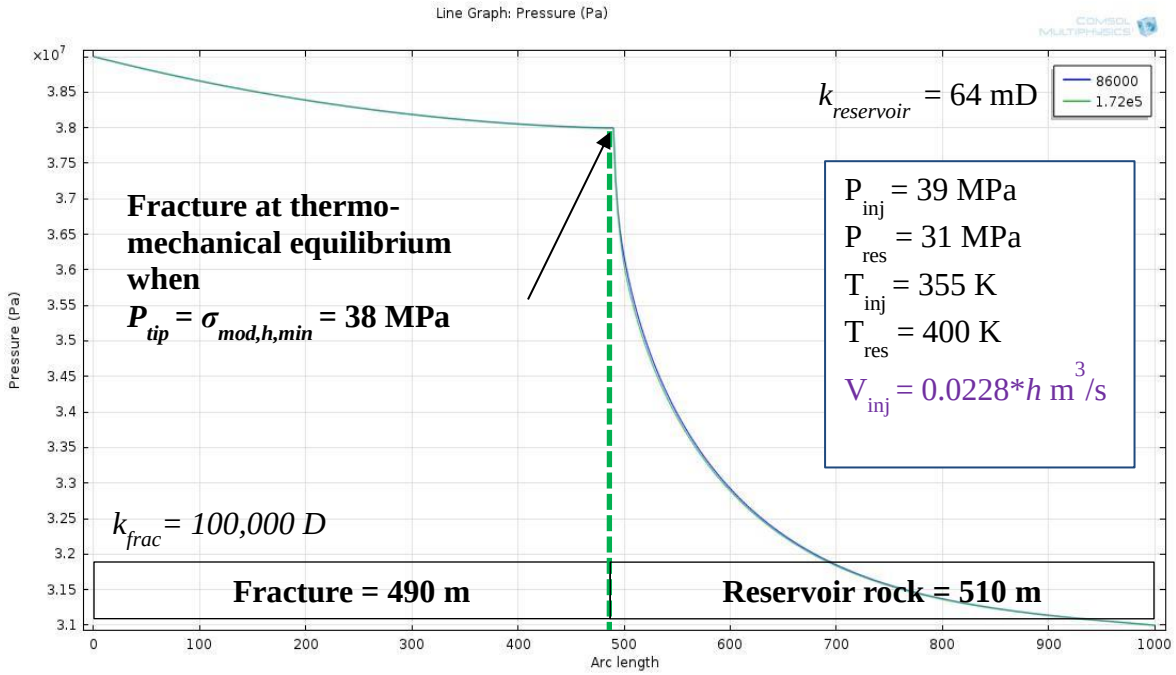

Figure 47: Pressure inside the fracture at the centerline and in the reservoir rock beyond the fracture tip in the same plane as the fracture, at the conditions of Run 10 (see Table 6). The legend indicates the elapsed time in seconds, up to two days of injection. The equilibrium fracture length is 490 m in this run, shorter than the 575 m fracture in Run 1 for the reasons described in the text. The injection rate is 0.0228 m^3/s per meter of fracture height, only marginally different from Run 1 (0.0225 m^3/s per meter of fracture height).

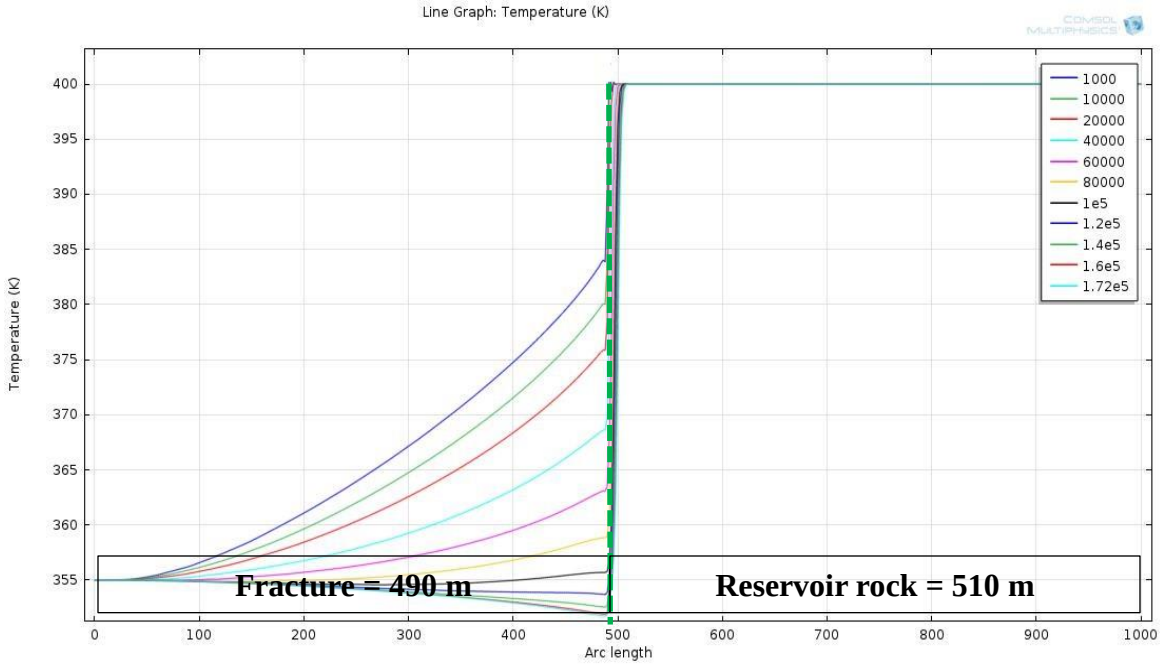

Figure 48: Temperature in the fracture at the centerline for two days of injection at the conditions of Run 10 (see Table 6). The thermal front reaches the fracture tip in about $1.2*10^5$ seconds, slower than in Run 1 due to the density difference of the fluid in the fracture (see text for more discussion).

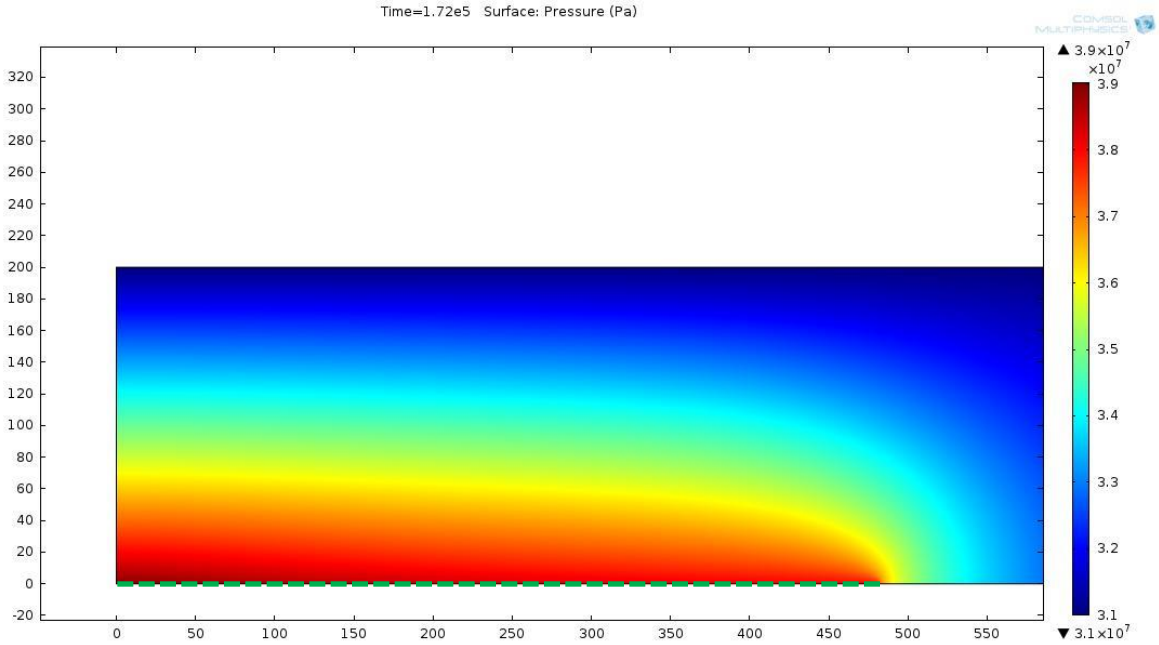

Figure 49: Pressure profile in the matrix at the conditions of Run 10 (see Table 6) at two days of injection. The pressure profile is constant due to the fixed geometry and pressure boundary conditions.

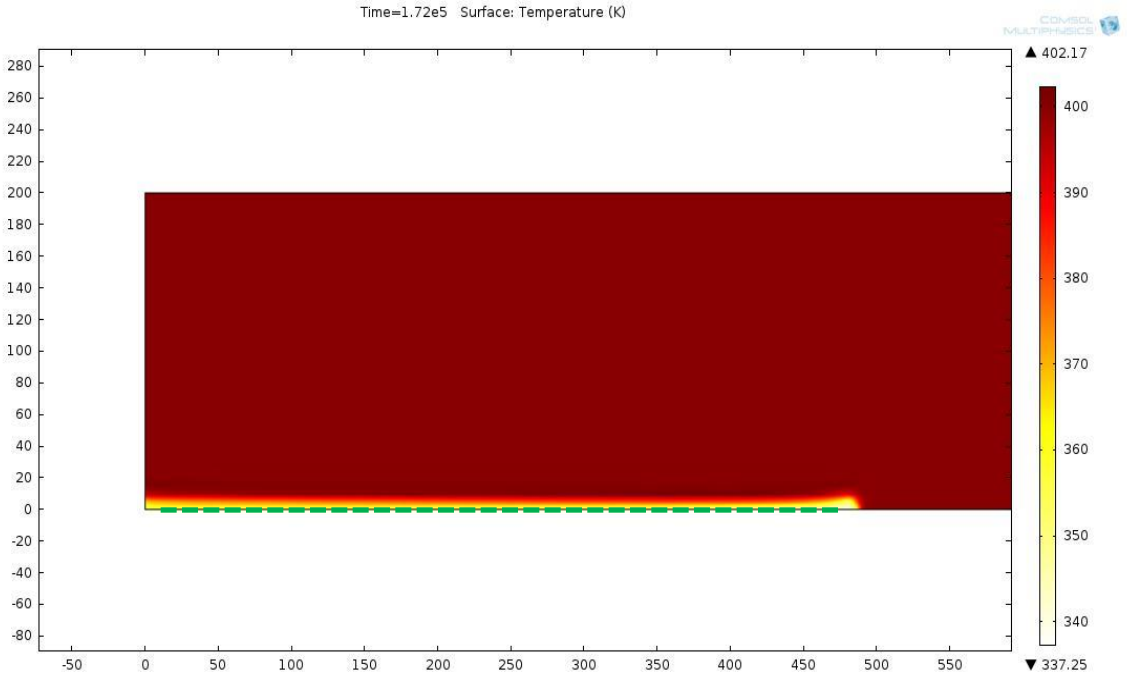

Figure 50: Temperature in the reservoir at two days of injection for the conditions of Run 10 (see Table 6). The thin invasion zone is due to the short simulation run time.

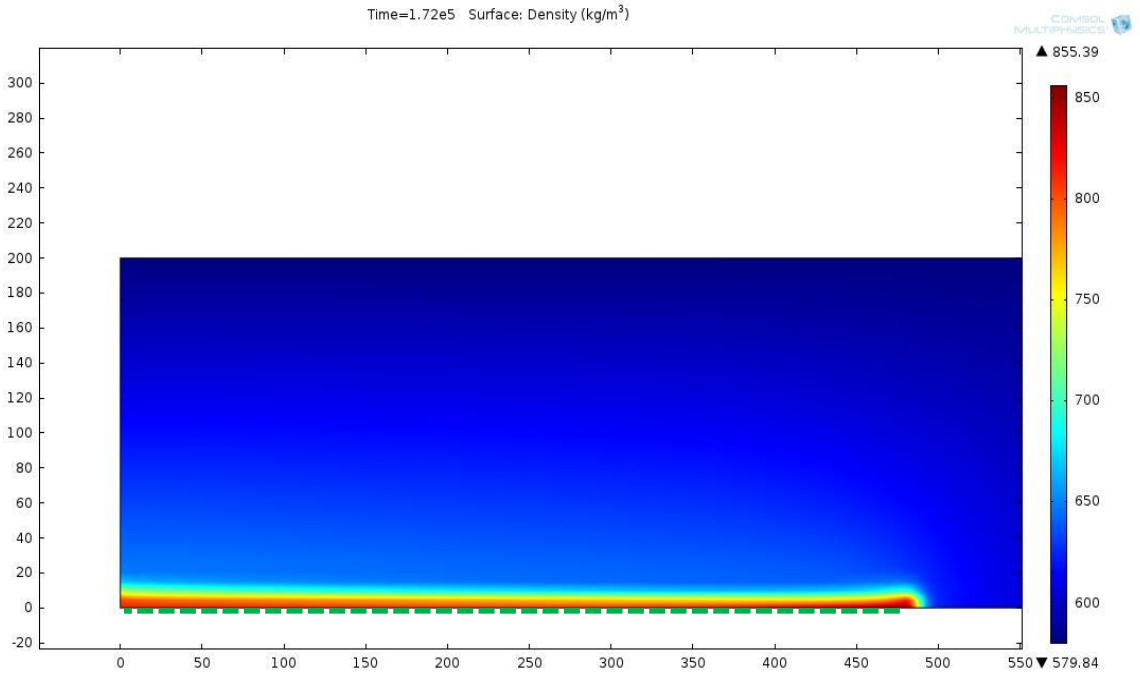

Figure 51: Density profile in the reservoir at two days of injection for the conditions of Run 10.

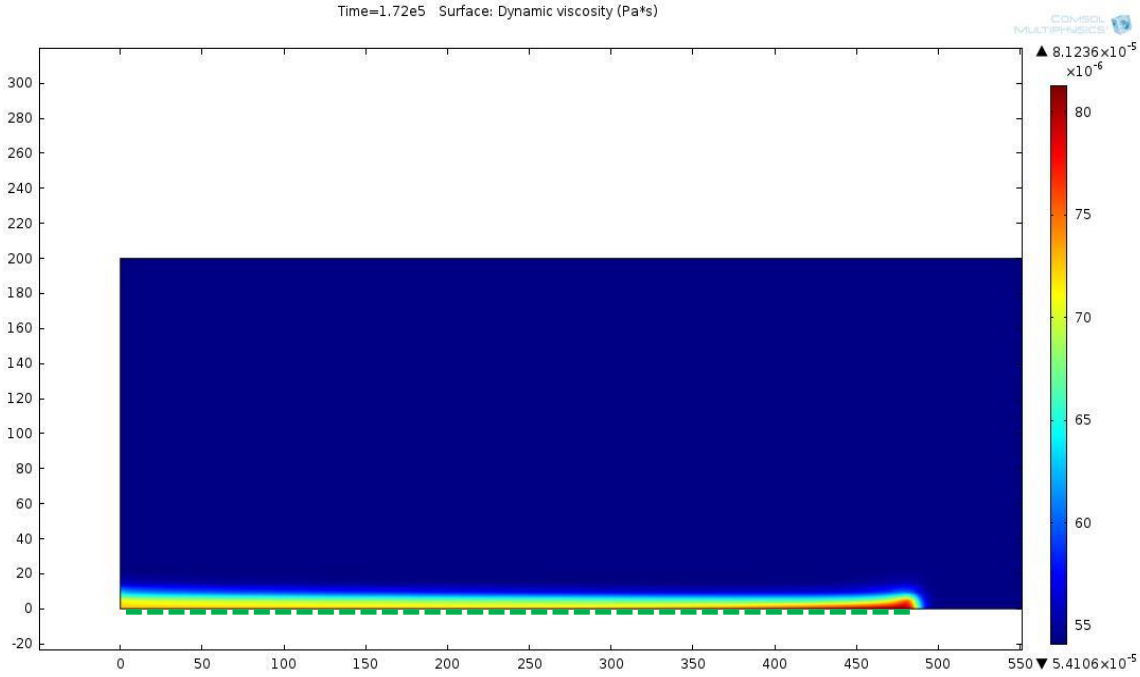

Figure 52: Viscosity profile in the reservoir at 2 days of injection for the conditions of Run 10. Viscosity is primarily a function of temperature, so the temperature profile can be inferred from this plot wherein the cold front has not propagated far into the matrix.

5.11 Run 11: Permeability Sensitivity using a 1000 mD Reservoir with Variable Fluid Viscosity and Density

The final run investigated the effect of a higher permeability reservoir on the equilibrium fracture length, combined with variable fluid properties, to determine if other unexpected phase behavior would be observed at higher flow rates. The fluid properties in the fracture and reservoir were calculated via the same method as in Run 10, using the EOS described in Section 3.3. The only difference between Run 10 and 11 was the 1000 mD reservoir rock in Run 11, versus 64 mD in Run 10. All other system properties were the same as in Run 10 (see Table 6). No results conflicted with previously observed trends. The fluid properties in the reservoir are depicted in Figures 56-58. The higher reservoir permeability led to a shorter fracture as shown in Figure 53 in this run (135 m) than in Run 10 (490 m). The same trend was observed in the higher reservoir permeability Run 6 compared to Run 1 where the fluid properties were constant everywhere in the system: 150 m versus 575 m.

The relative mobility effect of a high viscosity fluid displacing a low viscosity fluid (see Figure 58) was consistent with the length difference seen in Run 10 compared to Run 1 – it caused the equilibrium fracture length to decrease from 575 m to 490 m. Analogously, comparing Run 11 to Run 6, the relative mobility effect caused the fracture to decline from 150 m to 135 m.

The relative mobility effect also resulted in a higher injection rate in this run (0.146 m^3/s per meter of fracture height) compared to Run 6 (0.13 m^3/s per meter of fracture height), an 11% difference. The analogous difference in from Run 1 to Run 10

was only 2%, indicating the reservoir permeability does not cause injection rate to scale linearly with respect to the relative mobility of the fluids.

The higher fluid velocity into the higher permeability reservoir formed a larger zone of cooled rock as seen in Figure 56, displacing warm CO_2. As a result of a larger portion of the reservoir being filled with high viscosity fluid, the decrease in injection rate was 13% (from 0.146 m^3/s to 0.127 m^3/s per meter of fracture height) after two days of injection. The injection rate was converging on the rate seen in Run 6 where the viscosity of fluid everywhere in the system was a constant $6.36*10^{-5}$ Pa-s, albeit slightly lower here due to the higher viscosity of fluid in the fracture in Run 11 of $7.3*10^{-5}$ Pa-s. There was a negligible change in Run 10. If Run 10 had flowed for a longer period of time it is expected the injection rate would have fallen farther as more of the reservoir would be filled with high viscosity fluid. In summary, the relative mobility effect enhanced injection rate initially, but once the reservoir filed with fluid of the same viscosity as in the fracture, the injection rate declined to a value similar to those seen in previous runs where the viscosity was constant everywhere during the run.

The speed of the temperature front in the fracture as depicted in Figure 54 was consistent with that in Run 6: both conditions resulted in a speed of over 0.15 m/s due to the large injection rates.

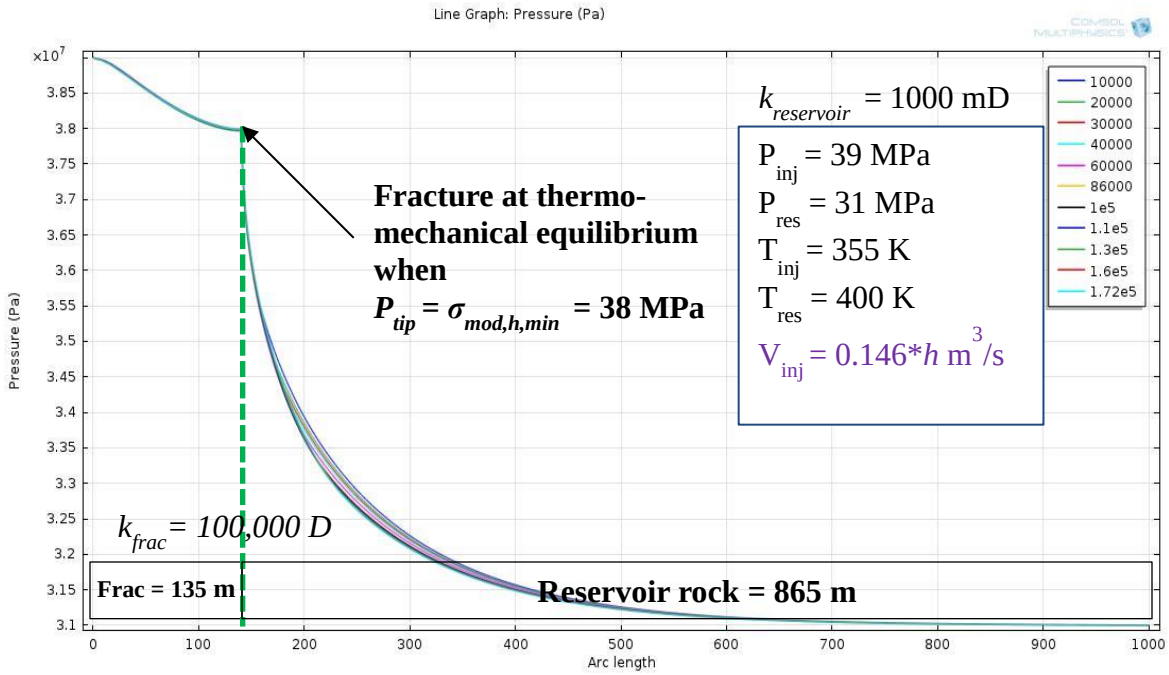

Figure 53: Pressure inside the fracture at the centerline and in the reservoir rock beyond the fracture tip in the same plane as the fracture, at the conditions of Run 11 (see Table 6). The legend indicates the elapsed time in seconds, up to two days of injection. The fracture length in this run was 135 m and the injection rate was 0.146 m^3/s per meter of fracture height.

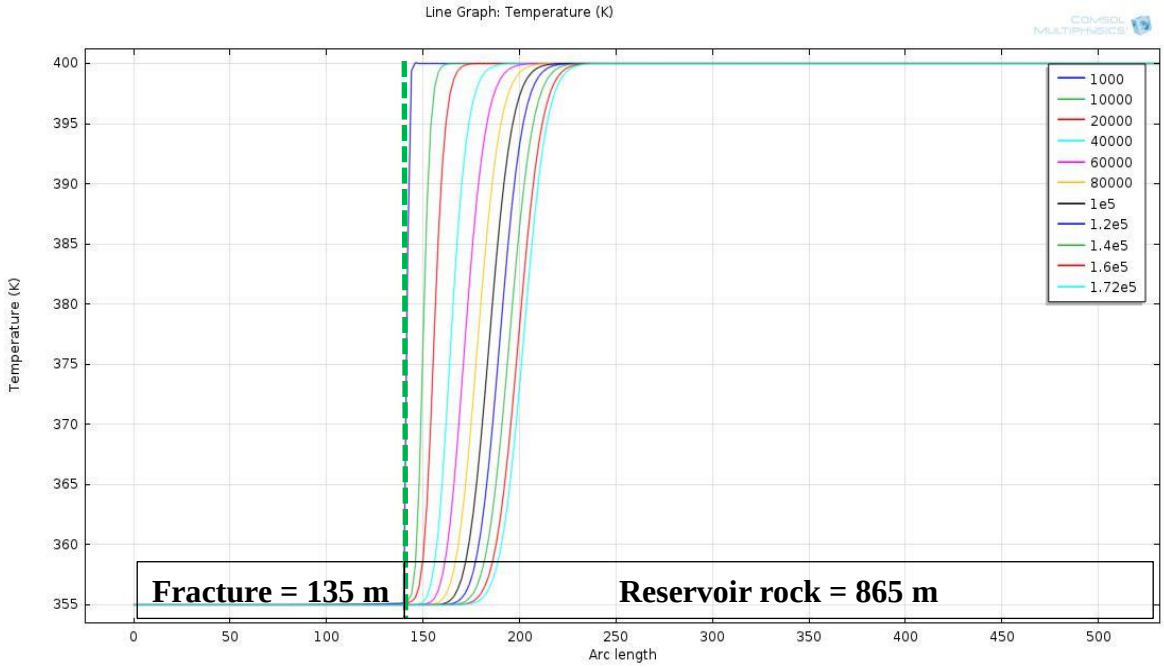

Figure 54: Temperature in the fracture at the centerline and extending into the reservoir ahead of the fracture tip in the same plane, for the conditions of Run 11 (see Table 6). The front extends 50m beyond the fracture tip at only 2 days of injection.

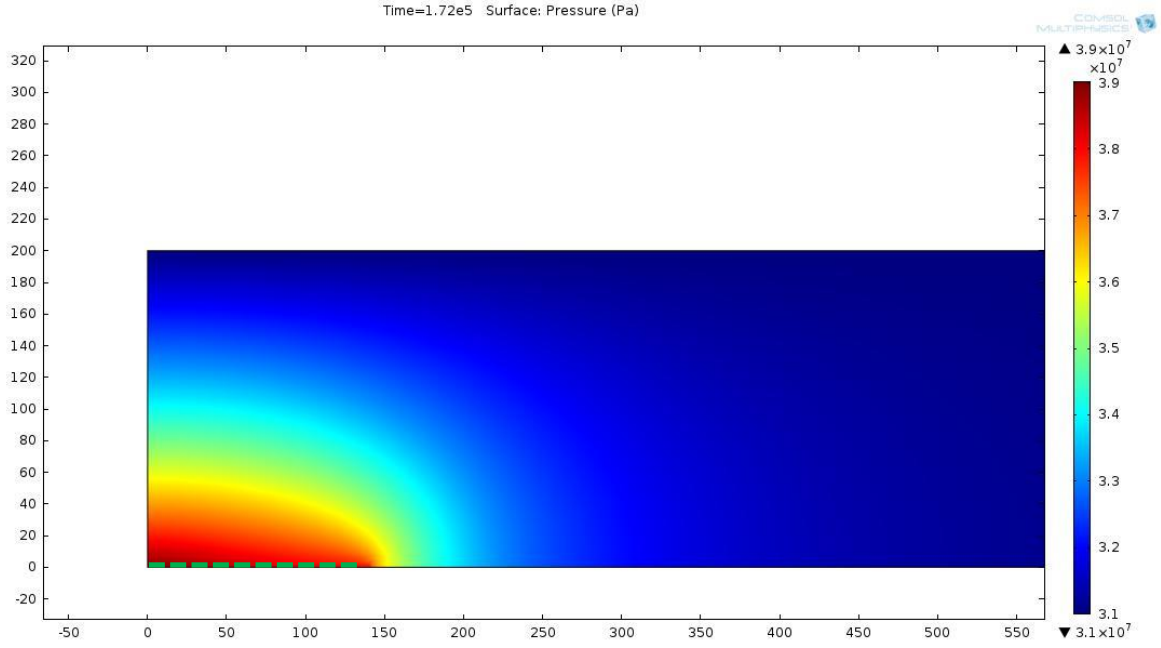

Figure 55: Pressure profile in reservoir at 2 days of injection for the conditions of Run 11. The fracture length is sensitive to the distance from the boundary and the pressure at that boundary. Because the domain geometry and boundary conditions are fixed this profile is static.

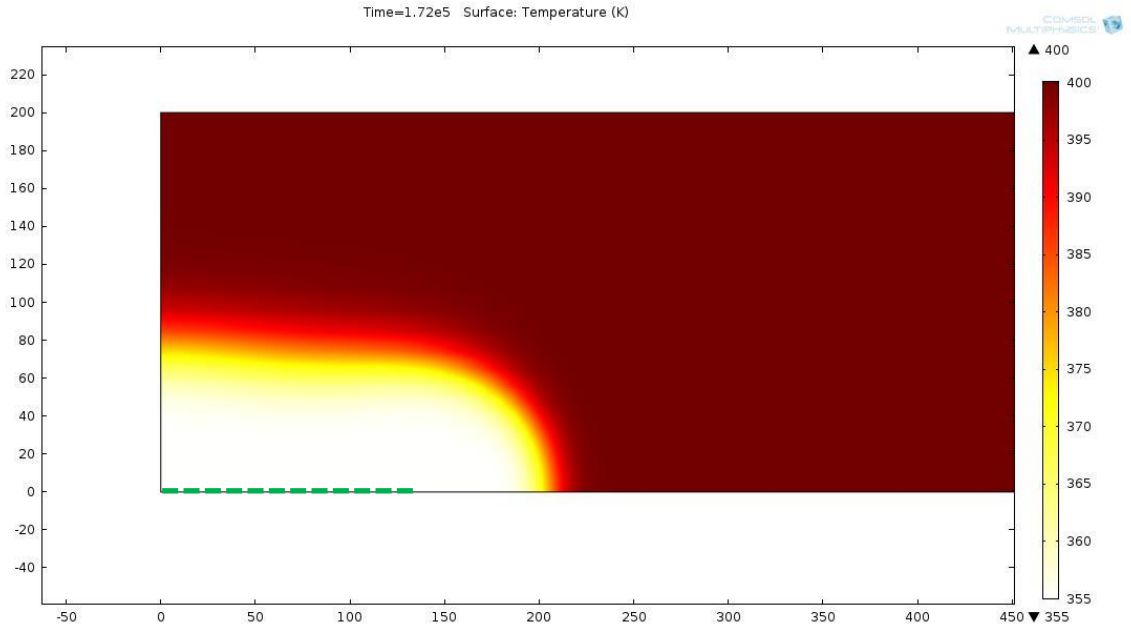

Figure 56: Diagram of the temperature profile in the matrix at 2 days of injection at the conditions of Run 11. The 1000 mD permeability of the reservoir allows much more flow out of the fracture than the 64 mD reservoir, and because the temperature front is convection dominated the cold front progresses rapidly into the reservoir: 50 m beyond the fracture tip at two days of injection.

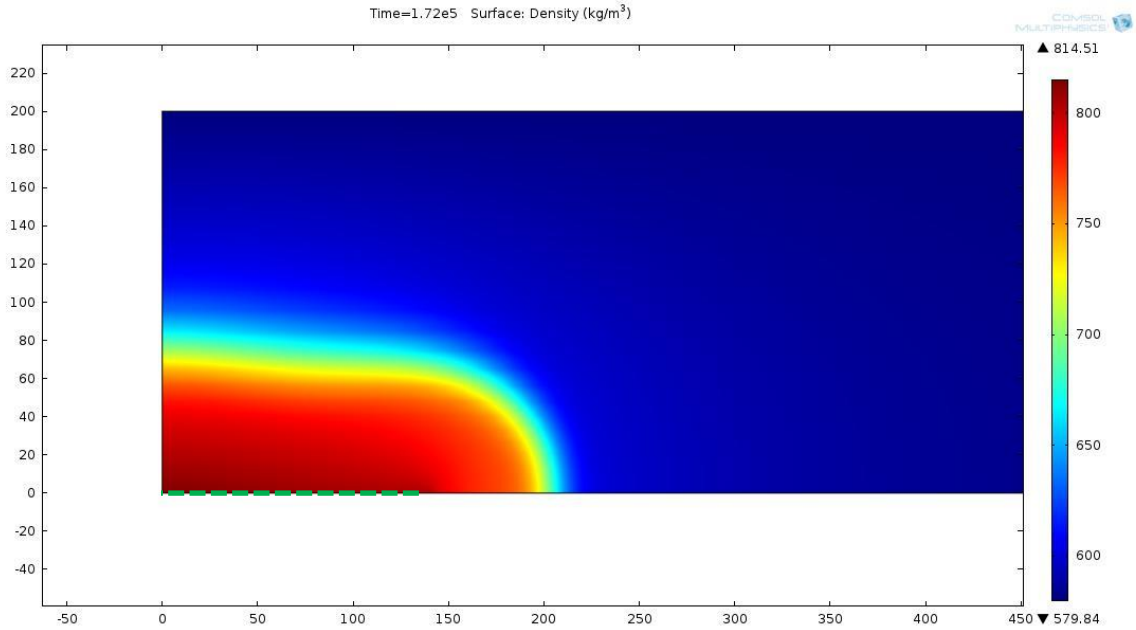

Figure 57: Density profile of the fluid in the reservoir at 2 days of injection for the conditions of Run 11. Density is more strongly a function temperature than pressure but it is more sensitive to pressure than viscosity.

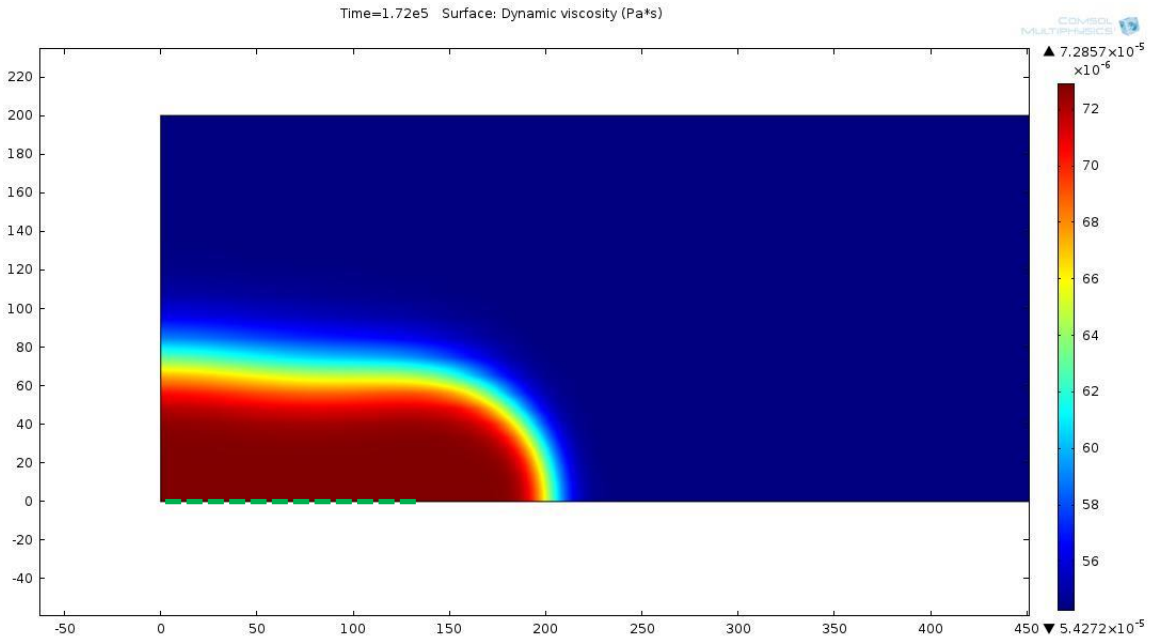

Figure 58: Viscosity profile in the reservoir at 2 days of injection for the conditions of Run 11. Viscosity is strongly influenced by temperature so very closely resembles the temperature front. Notice the large viscosity difference between the fluid injected and the in-situ fluid, which leads to relative mobility effects on the fracture length, as discussed in the text above.

5.12 Analytical Solution for Equilibrium Fracture Length Compared to COMSOL Solution

The steady-state nature of the fracture geometry at equilibrium lent itself to an analytical solution for fracture length based on one dimensional conservation of mass of fluid flowing through the fracture and into the reservoir. This equation is:

$$X_f^2 = \frac{9wL_y}{2}\left[\frac{P_2 - P_{tip}}{P_{tip} - P_b}\right]\left[\frac{k_f}{k_m}\frac{\mu_m}{\mu_f}\right] \tag{26}$$

$$P_2^2 + \left(P_{tip} - 3P_b\right)P_2 - \left(P_{inj}P_{tip} + P_{tip}^2 - P_{inj}P_b - 2P_{tip}P_b\right) = 0 \tag{27}$$

wherein X_f is the length of one wing of a bi-wing fracture, L_y is the distance perpendicular from the fracture to the boundary at pressure P_b, w is the fracture width, P_{tip} is the pressure in the fracture tip equal to $\sigma_{mod,h,min}$, k is the permeability of the fracture (f) and

reservoir (m), μ is the viscosity of the fluid in the fracture and reservoir, P_{inj} is the injection pressure and P_2 is a dummy variable. The derivation of this equation can be found in the Appendix. Figure 59 qualitatively shows the fracture equilibrium length versus the variables in Equation 26.

Table 7 provides a comparison of the analytical solutions for fracture lengths using the variables from all the runs made in COMSOL. There is good agreement between these two methods. Equation 26 is also useful to understand the effect of each system variable on the fracture length. It explains the impact of the relative mobilities of the fluids of different viscosities, and even can be used to predict how a fracture length may change for other types of reservoir injection. Other scenarios could be cold CO_2 injected into a hot, brine-filled reservoir, cold water injected into an oil-filled reservoir, cold CO_2 injected into a hot CO_2-filled reservoir. The COMSOL model is still necessary to calculate the heat transfer in the system, i.e. to determine whether the cool fluid reaches the fracture tip in a period of time that is short relative to the long duration of CO_2 injection in a storage reservoir.

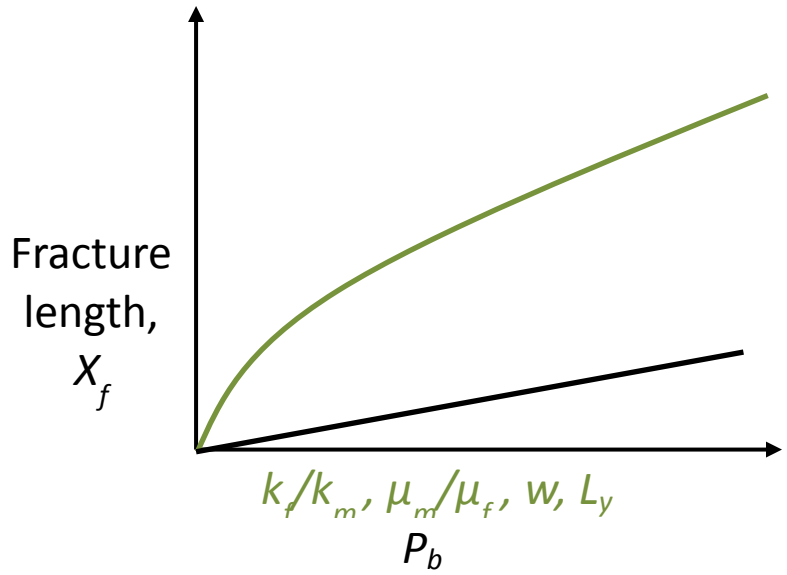

Figure 59: Fracture equilibrium length versus the system variables as described in Equation 26. The green line represents the relationship between fracture length and the variables in green on the x-axis. The black line represents the relationship between X_f and the variable in black on the x-axis. This graph assumes fixed injection, fracture tip and boundary pressures.

Case	Frac length [m]	Analytical frac length [m]	Error [%]
Run 1	575	583	**1.39%**
Run 2	575	583	**1.39%**
Run 3	575	583	**1.39%**
Run 4	575	583	**1.39%**
Run 5	575	583	**1.39%**
Run 6	150	145	**3.33%**
Run 7	160	184	**15.00%**
Run 8	880	881	**0.11%**
Run 9	>1000	1408	**---**
Run 10	490	493	**0.7%**
Run 11	135	123	**8.89%**

Table 7: Comparison of the analytical solution for fracture length in Equation 26 to the COMSOL simulation results.

In Table 8 are the analytical solutions for equilibrium fracture lengths for a variety of cases that might be encountered in the field. The reservoir and fracture parameters are the same as in the base case, Run 1. Comparing the different runs, the equilibrium fracture length is likely to change over time during CO_2 storage. Initially, a warm aquifer containing brine with higher viscosity than the injected CO_2 will result in a fracture around 1000 m long (row 1 of Table 8). Then as the brine is displaced by warm CO_2 the fracture will shrink to about 490 m (row 4 of Table 8, or Run 10). After a large portion of the reservoir cools after being filled with injected CO_2 the fracture will grow to about 575 m (Run 1 of Table 7). At that point the area around the fracture will contain a fluid of nearly the same properties as the fluid in the fracture as they are most strongly temperature dependent, and reservoir temperature is close to the fracture temperature. The fracture will then remain at that length unless the average reservoir pressure changes. To describe this progression in runs, first is the extra case "Cold CO_2 into Hot Water" (see Table 8), second is Run 10, and third is Run 1.

Extra Cases	Fracture Viscosity [Pa-s]	Reservoir Viscosity [Pa-s]	Analytical Fracture Length [m]
Cold CO_2 into Hot Water	7.50E-05	2.26E-04	**1011**
Cold Water into Viscous Hot Oil	3.56E-04	2.00E-02	**4364**
Cold Water into Low Viscosity Hot Oil	3.56E-04	1.10E-03	**1023**
Cold CO_2 into Hot CO_2	7.50E-05	5.24E-05	**493**
Cold Water into Hot Water	3.56E-04	2.26E-04	**464**

Table 8: Extra field cases and the resulting fracture lengths calculated using Equation 26.

Lastly, multiple COMSOL simulations were not performed at a constant injection rate and across a range of viscosity to determine how this might alter the fracture length. The result of such scenarios can be extrapolated from the runs already made. Injection rate is inversely proportional to viscosity at constant injection and reservoir pressure, so to achieve the same rate with a high viscosity fluid as with a low viscosity fluid the injection pressure must be higher. Because the injection pressure must be higher to achieve the desired rate, the fracture would have to be longer to achieve the required pressure drop from inlet to tip, because the tip pressure must equal $\sigma_{mod,h,min}$ as previously discussed.

For example in Run 1 the fluid viscosity was $6.36*10^{-5}$ Pa-s, the injection pressure was 39 MPa, the injection rate was 0.0209 m^3/s per meter of fracture height and the equilibrium fracture length was 583 m. These values were calculated using Equations 26-28. If the fluid viscosity is increased to $2.9*10^{-4}$ Pa-s (the viscosity of water used in Run 2 for both injected and reservoir fluids) and all other system parameters are the same as in Run 1 (see Table 6), then the injection pressure would have to increase to 48 MPa and the fracture length to 1740 m to achieve the same injection rate. Alternatively, if the viscosity is increased only moderately to $7*10^{-5}$ Pa-s, the injection pressure must be 39.2 MPa and the equilibrium fracture length 640 m to achieve the same injection rate of 0.0209 m^3/s per meter of fracture height. Figure 60 shows the pressure profile calculated by COMSOL in the fracture for this case with the higher injection pressure and higher viscosity fluid. It illustrates the equilibrium criteria similar to Run 1, at a longer equilibrium fracture length but with the same injection rate as in Run 1. Figure 61 shows

the relationship between injection pressure and viscosity, and fracture equilibrium length and viscosity for a fixed injection rate.

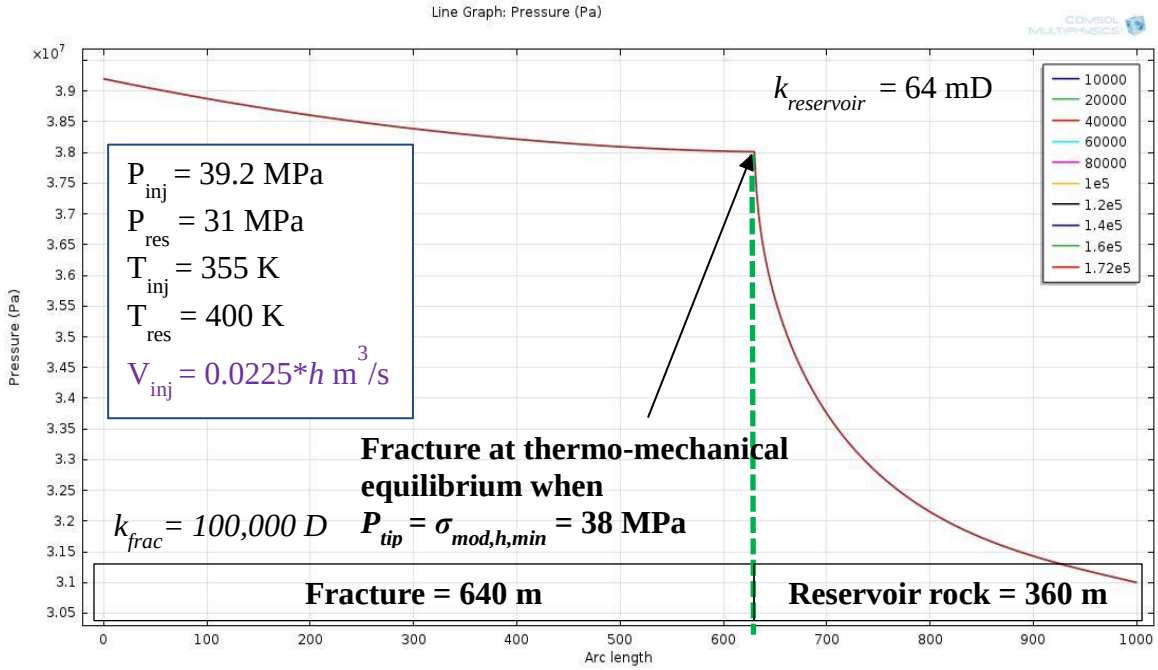

Figure 60: Pressure profile in the fracture at the centerline and in the reservoir beyond the fracture tip using a fluid viscosity of $7*10^{-5}$ Pa-s, but with all other system parameters the same as in Run 1 (see table 6). In order to achieve the same injection rate as in Run 1 (0.0225 m^3/s per meter of fracture height), the injection pressure must be 39.2 MPa, and this causes the fracture equilibrium length to extend to 640 m instead of 575 m as in Run 1.

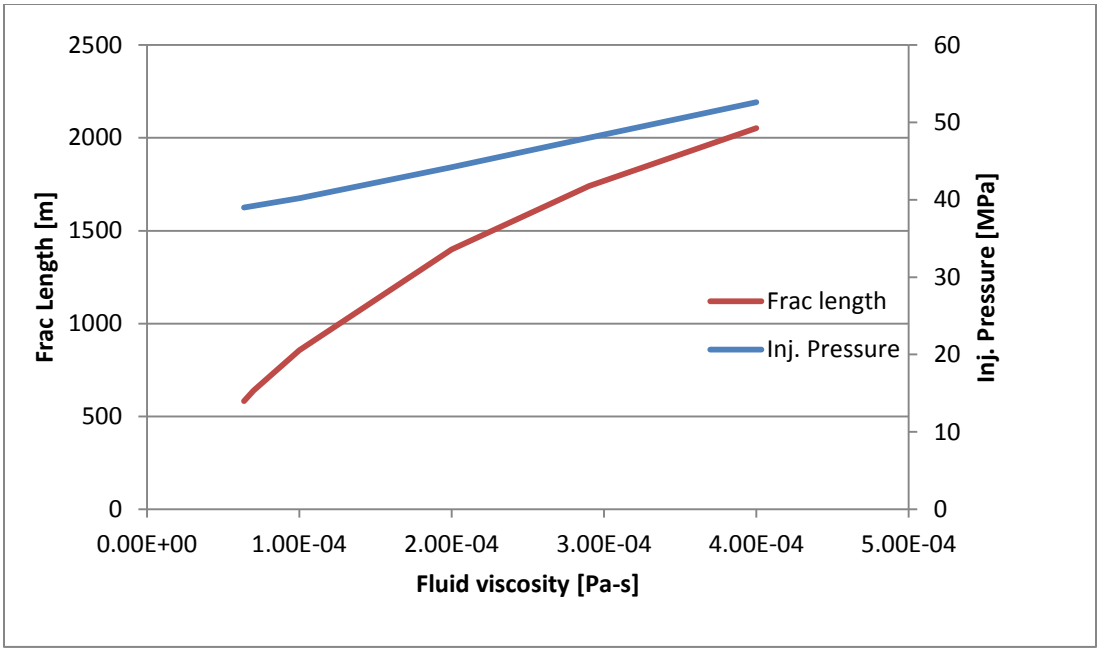

Figure 61: Injection pressure (P_{inj}) and fracture equilibrium length (X_f) plotted against fluid viscosity where the system has only one viscosity for both injected and reservoir fluids at a fixed injection rate (0.0209 m^2/s) as in the example above. All other conditions were the same as in Run 1 (see Table 6). The relationship between the injection pressure and viscosity is linear, while the relationship between fracture equilibrium length and viscosity is a second order polynomial, for a fixed injection rate, boundary pressure and system geometry. These data were calculated using Equations 26-28.

5.13 Analytical Solution for Injection Rate Compared to COMSOL Solution

Using the same one dimensional approximation for fluid flow as in the previous section to derive a fracture equilibrium length equation, an analytical solution for the injection rate of the system was also derived. This equation is:

$$A_{inj} = \frac{X_f}{3L_y}\frac{k_m}{\mu_m}\left(P_{inj} - P_b\right) + \frac{3w}{2X_f}\frac{k_f}{\mu_f}\left(P_{inj} - P_2\right) \qquad (28)$$

wherein the variables are the same as those used in Equation 26 with the addition of the injection rate A_{inj} in m^2/s, that is the injection rate per meter of fracture height. Table 9 shows the comparison of the analytical solution to the COMSOL simulations. There is

good agreement between the two methods except when the fracture lengths are short. Short fractures cause the flow into the reservoir to be more radial, and therefore not well characterized by a 1D linear flow equation such as Equation 28. This discrepancy can be seen comparing Figures 50 and 56. Otherwise, for the long fractures, the analytical solution produces good estimates of injection rate, similar to the COMSOL results.

Case	Injection rate: COMSOL [m^2/s]	Injection rate: analytical [m^2/s]	Error [%]	Analytical frac length [m]
Run 1	0.0225	0.0209	**7.11%**	583
Run 2	0.0049	0.0046	**6.12%**	583
Run 3	0.0014	0.00135	**3.57%**	583
Run 4	0.0226	0.0209	**7.52%**	583
Run 5	0.0225	0.0209	**7.11%**	583
Run 6	0.13	0.084	**35.38%**	145
Run 7	0.008	0.0066	**17.50%**	184
Run 8	0.0152	0.0147	**3.29%**	881
Run 9	---	0.0103	**---**	1408
Run 10	0.0228	0.0207	**9.21%**	493
Run 11	0.127	0.083	**34.65%**	123

Table 9: Comparison of the analytical solution for injection rate per meter of fracture height to the COMSOL simulation results using Equation 28. The largest errors were seen for the runs with the shortest fracture lengths. This was due to the one-dimensionality assumption of Equation 28 that is not a good representation of the true flow field when the fractures are short, which cause more radial flow in the reservoir.

Equation 19 describes a constant thermal retardation factor for a thermal front lagging behind a flood front assuming constant velocity, 1D flow through a porous medium, neither of which apply to flow down a fracture. In the case of a cold fluid traveling down a fracture and flowing into a hot reservoir, as in the simulations in this thesis, fluid flow is in two dimensions, and the velocity of the fluid in the fracture decreases from a maximum at the fracture inlet to near zero at the tip. Therefore a constant thermal retardation factor may not describe the velocity of the thermal front in the fracture relative to the velocity of fluid flow in the fracture. However, the thermal front velocity in the fracture is primarily controlled by the injection rate into the reservoir.

The travel time of the thermal front to the fracture tip from the inlet versus the travel time of a particle of fluid from the inlet to the fracture tip for Runs 1-8 are shown in Figure 62. The thermal front velocity is much smaller than the fluid velocity. This is because heat is conducted into the fluid in the fracture in two directions, parallel and perpendicular to the fracture, slowing the progress of the thermal front at injection temperature. Conduction in the perpendicular direction is even greater near the fracture tip where the fluid velocity is slower.

The impact of these forces depends on the reservoir permeability as well. Injection rate increases as the reservoir permeability increases (with constant inlet and outlet boundary pressures), and the amount of heat conduction into the fracture depends on the size of the cold fluid bank outside the fracture, which is a thin region when the reservoir permeability is low or the injection rate is low, but which grows with time.

Hence, in these simulations the velocity of the thermal front is transient, depending on the size of the cold fluid bank outside the fracture.

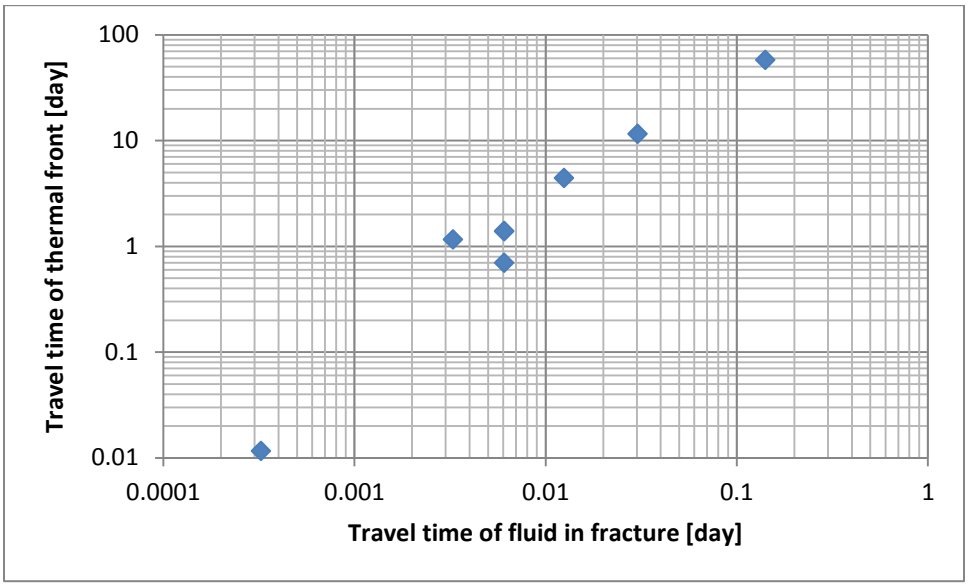

Figure 62: Travel time of thermal front to fracture tip versus travel time of fluid to fracture tip for all runs where the fluid had constant properties (i.e. all but Runs 9, 10 and 11).

In a realistic CO_2 sequestration reservoir, the injection rate would likely be smaller than the injection rates calculated by COMSOL as previously discussed. This would lead to slower thermal fronts in the fracture, possibly 10 to 100 times slower as per the trend seen in Figure 62. The consequence of a slower thermal front is slower propagation of a thermoelastic fracture, however the equilibrium fracture length would remain unchanged.

Chapter 6: *Summary and Conclusions*

6.1 Summary of Results

This thesis proposed a method of calculating a thermoelastic fracture equilibrium length based on some simplifying assumptions about the CO_2 storage reservoir and fracture geometry. The model encompassed two dimensions for a constant width fracture of constant properties adjacent to a reservoir domain of constant properties (e.g. permeability, porosity, thermal conductivity, etc.). Fluid was injected into this system, and the simulator calculated single phase flow and energy transport in the system. This yielded thermal front movement down the fracture and into the reservoir, and the pressure gradients in the fracture and reservoir which quickly approached steady-state due to the constant boundary conditions.

The model enabled comparison of the competing convective and conductive heat transport, and the conservation of momentum in a thermally transient system. Various cases were run to determine the relative effects of reservoir permeability, fracture permeability, fluid heat capacity, viscosity and density, displacement with a viscosity contrast, and reservoir boundary pressure on final fracture length. Lastly, an analytical solution of the fracture length was derived and proposed that predicted lengths of good agreement with the full reservoir simulator.

A concise relationship of the variables controlling fracture length can be found in Equation 26. Variables that increase fluid flow from the fracture decrease its length. These are higher reservoir permeability, lower boundary pressure, and an in-situ reservoir fluid of lower viscosity than the fluid injected. When the in-situ and injected fluid have

the same viscosity their magnitude is irrelevant to fracture length. However, a difference in viscosity between the injected fluid and in-situ fluid will cause a longer or shorter fracture than the single viscosity case, depending on their ratio. Fracture length is proportional to μ_m/μ_f and k_f/k_m as per Equation 26. Low fracture permeability also limits fracture length as increased resistance to flow results in a larger pressure gradient in the fracture (dP/dx). The effect of the boundary pressure can vary with its magnitude or its distance perpendicularly from the fracture – dP/dy. Increasing dP/dy enhances fluid flow out of the fracture shortening the fracture. Due to the prescribed boundary conditions in the simulations of constant pressure, the fluid density had no effect on the fracture length.

Runs performed with different fluid viscosities had no effect on fracture length - as long as the viscosity in the fracture was equivalent to that in the reservoir - but viscosity did alter the injection rate of the reservoir. Lower viscosity fluids resulted in higher injection rates for the same fracture length. Injection rate was a function of the permeabilities of the fracture and reservoir, in direct proportionality, and of the fracture length. It increased with larger fracture permeability, and again with larger reservoir permeability.

Temperature front velocity in the fracture is most strongly controlled by injection rate, reservoir permeability, and heat capacity. In general, the temperature front in the fluid at the injection temperature traveled to the fracture tip within days due to the very large injection rates in these simulations. The injection rate of a real storage reservoir would likely be 10 to 100 times smaller than the rates achieved in these simulations. Therefore the speed of the thermal front in a real injection induced fracture would likely

be much slower than what observed in these simulations, on the order of 10 to 100 times smaller. Slower thermal fronts in fractures in real storage reservoirs would still result in rapid fracture propagation relative to the lifetime of an injection well, reaching their equilibrium length within a few weeks to a few months.

The cold temperature front extending into the reservoir reduced conduction of heat into the fracture from the reservoir, maintaining low temperature in the fracture. This effect was more noticeable when the reservoir permeability was larger allowing a thicker bank of cold fluid to form around the fracture. The thick cold fluid banks maintained their low temperature in the reservoir for the duration of the runs, hence it is expected cooling of the reservoir to nearly injection temperature will occur for as long as injection continues. At low injection rates like those expected in a real storage reservoir, the velocity of the fluid in the fracture is smaller and the cold fluid bank outside the fracture would be grow much more slowly. Therefore the thermal front speed in the fracture would be smaller too. This indicates the temperature front velocity in the fracture is controlled primarily by the injection rate, which (depending on reservoir permeability) controls the size of the cold fluid bank and the amount of conduction that can warm the fluid in the fracture.

Heat capacity of the fluid also had a noticeable impact on the velocity of the temperature front in the fracture, with larger heat capacities providing larger velocities. Similarly, higher density fluids resulted in faster thermal fronts.

The method in this thesis did not solve fracture propagation, but specified a fracture length that would exist at equilibrium. Knowing the temperature front velocity is

high in a fracture, the temperature at a fracture tip would always be very nearly the injection temperature so the difference between the reservoir and fluid temperature at the tip would be at a maximum. This temperature difference would provide a maximum thermoelastic stress reduction on the minimum horizontal principal stress as long as the shape of the temperature front was close to circular, which is the necessary shape factor for thermoelastic fracture propagation.

The thermoelastic stress reduction will spread into the reservoir with the cold fluid front, but at the fracture tip there is an absolute lower limit to the modified minimum horizontal stress, so the spreading thermoelastic stress reduction will not cause the fracture to continue to grow. It was shown the thermoelastic stress reduction on the fracture propagation pressure can be large enough for fractures to grow at internal pressures well below the nominal fracture pressure.

Fracture propagation will cease once friction and mass transfer out of the fracture cause the fluid pressure in the fracture to fall to the modified minimum horizontal Earth stress at the tip. The pressure gradients in realistic storage reservoirs controlling mass transfer out of the fracture would be smaller than in the simulations in this thesis, and thus would increase the equilibrium fracture length. However, the permeability of injection-induced fractures may be smaller in a realistic reservoir due to the possibility of small net pressure in the fracture. Even with a small fracture permeability and large pressure gradient in the reservoir (as in Run 7), the equilibrium fracture length was still around 150 m. Thus injection-induced fractures in real storage reservoirs with small pressure gradients are likely to extend multiple hundreds of meters before reaching

equilibrium. The injection rate would also be lower than what is predicted by the simulation.

6.2 Field Considerations while using the Model

The primary purpose of this thesis was to determine the competing physical phenomena that govern thermoelastic fracture growth. The implementation of this model is recommended in fields that are planned to have multiple wells, particularly injection and production wells as fractures tend to grow toward regions of decreased pore pressure. Typical injection-production well patterns are depicted in Figure 63. This thesis demonstrated it is possible for thermoelastic fractures to grow over 1000 m in length in a 64 mD reservoir if pressure gradients are extremely large. A typical 5-spot pattern on 160 acre spacing will have wells about 1600 m apart. If the reservoir permeability is low enough an injection-induced fracture could intersect a production well from an injection well. Another common well spacing is 40 acre spacing which would place wells about 380 m apart. This is also a length a thermoelastic fracture could reach. Therefore designing well spacing and patterns based on this model requires good reservoir characterization, specifically geomechanical characterization.

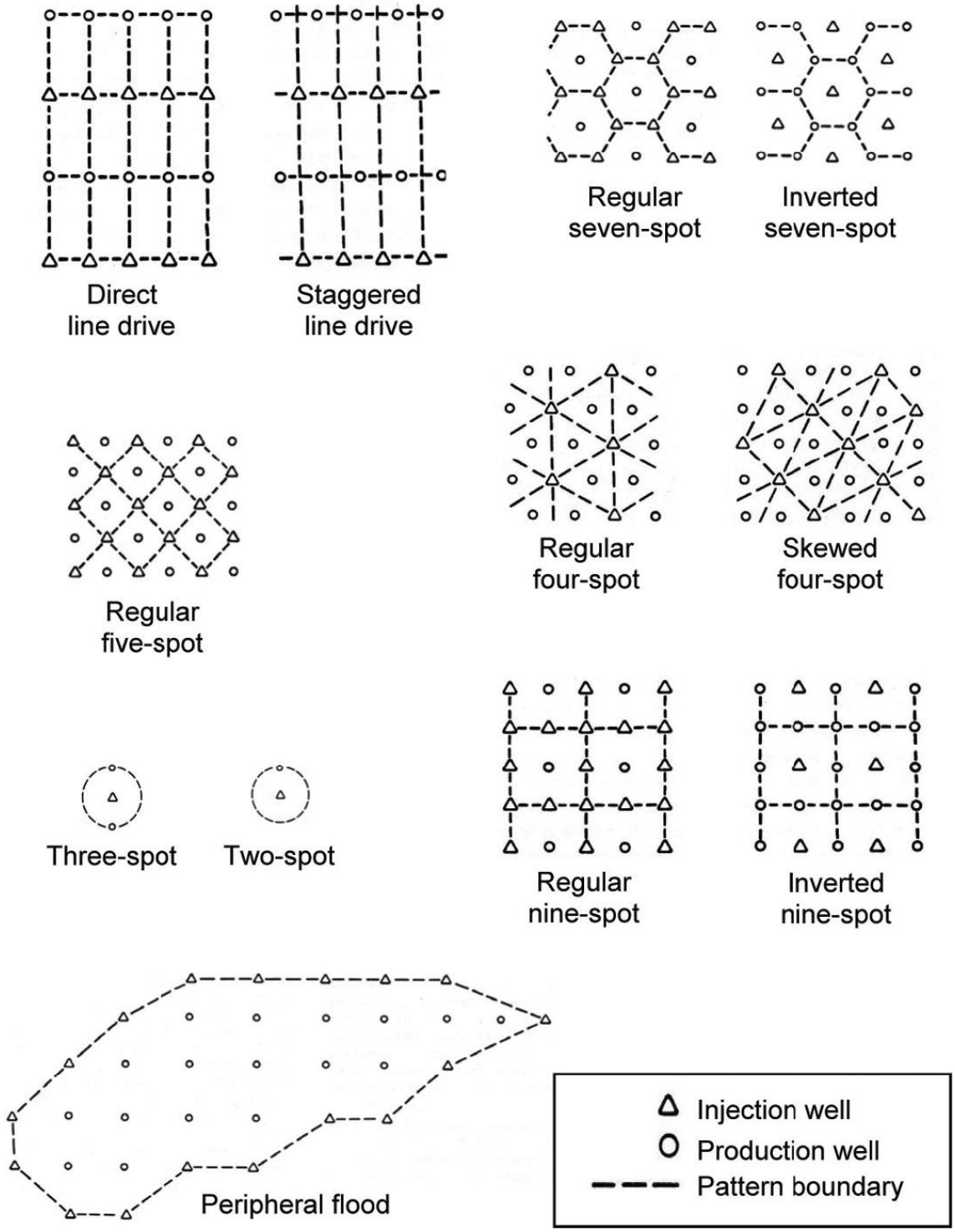

Figure 63: Common waterflood well patterns. CO_2 sequestration will also likely involve multiple wells which could be impacted by long thermoelastic fractures [38].

Formation testing to quantify the minimum horizontal stresses and directions in the target reservoir and overburden is critical in predicting whether a fracture will be height bounded and in which direction it will grow. Typical stress contrasts observed in the field are around 1000 psi or 7 MPa. Thermoelastic stresses are on the same order of magnitude at around 4.5 MPa. If, for example, the storage reservoir has an original $\sigma_{h,min,target}$ of 42.5 MPa, and the overburden composed of impermeable shale has a $\sigma_{h,min,over}$ of 49.5 MPa, then the readily established $\sigma_{mod,h,min,target}$ is about 38 MPa. As shown in this thesis, heat transfer is convection dominated; therefore the thermoelastic stress reduction in the target reservoir will spread rapidly, however the thermoelastic stress effect will not spread into the overburden as quickly because it must do so only via conduction.

Assuming the injection pressure into the target reservoir is equal to or slightly above the $\sigma_{mod,h,min,target}$, the early safety factor describing the margin between the injection pressure and the overburden fracture pressure will then be about 1.3 ($\sigma_{h,min,over}$ divided by the injection pressure). However, at late time heat conduction out of the overburden will have cooled that layer, possibly reducing the $\sigma_{mod,h,min,over}$ to about 45 MPa. This results in a safety factor of only 1.18. The risk of compromising a storage formation seal could be real if the reservoir is not pressure managed, meaning it increases over time. An operator could think he must increase the BHP to maintain his injection rate, in which case the safety factor quickly disappears. This thesis has demonstrated it is definitely possible for a fracture to be contained vertically, but extensive formation testing and thermal calculations need to be performed, and the rock layers characterized,

so proper operational procedures can be implemented to contain injected fluids given the low safety factors.

Knowing the reservoir boundary pressures (controlling the *dP/dy* gradient) and temperatures are also critical as final fracture length is very sensitive to these parameters, as discussed earlier. If multiple wells are injecting and producing from the same reservoir, characterizing any changes in pressure profiles throughout the formation is needed to predict whether fractures will shorten or grow due to the poroelastic changes.

More work also needs to be done to characterize the 3D shape of injection-induced fractures. Very little experimental evidence exists to accurately predict their shape. A proxy used in this work was the fracture permeability, but the correlation between 3D geometry and permeability is not well understood. The reservoir-conditions mechanical rock properties need to be tested in the storage formation to predict how the crack will open.

6.3 Future Work

The biggest limitation of the model developed in this thesis was the 2D setup. By neglecting vertical fracture growth, 1) the length of the fractures calculated herein are probably overestimated, and 2) 3D heat conduction may become significant at late times when the flood front of injected CO_2 is deep into the reservoir and traveling at low velocity. At that point, the rate of heat conduction will approach the rate of convection, arresting the thermal front advance. Future work should include this third dimension in a method similar to that used in the EFRAC-3D fracture simulator previously introduced, for use in the geomechanical and heat transfer calculations.

Another component to add to this simulator is poroelasticity effects, whereby the Earth stress regime changes with pore pressure. In reality, increasing reservoir pressure would also increase the minimum principal horizontal stress which would force the fracture to close, (poroelastic stress effect from Equation 12). More research needs to be done to determine the rate at which the reservoir pressure increases and Earth stress increases to determine their relative effects on fracture length. If the average reservoir pressure is not constant, the growing reservoir pressure will also apply backpressure to the fracture which has been demonstrated to increase the fracture length. The relative rates of change are not yet well understood, but hypothetical scenarios could be run using the COMSOL model. The poroelastic effects are also different on a local scale in near-fracture flooded region versus a global scale where the fluid in the reservoir is the original brine and at a lower pressure than in the flooded region. The mechanics of an elastic porous media and the variation in the stress regime with respect to pore pressure variation would merit attention.

Finally, it would be useful to test real storage formations for the presence of thermoelastic fractures and compare those results with theoretical fracture size. This may not be possible until new technologies are developed to test fracture size deep into a formation.

Appendix

Analysis of Injection Data from the Cranfield CO_2 Pilot Storage Project

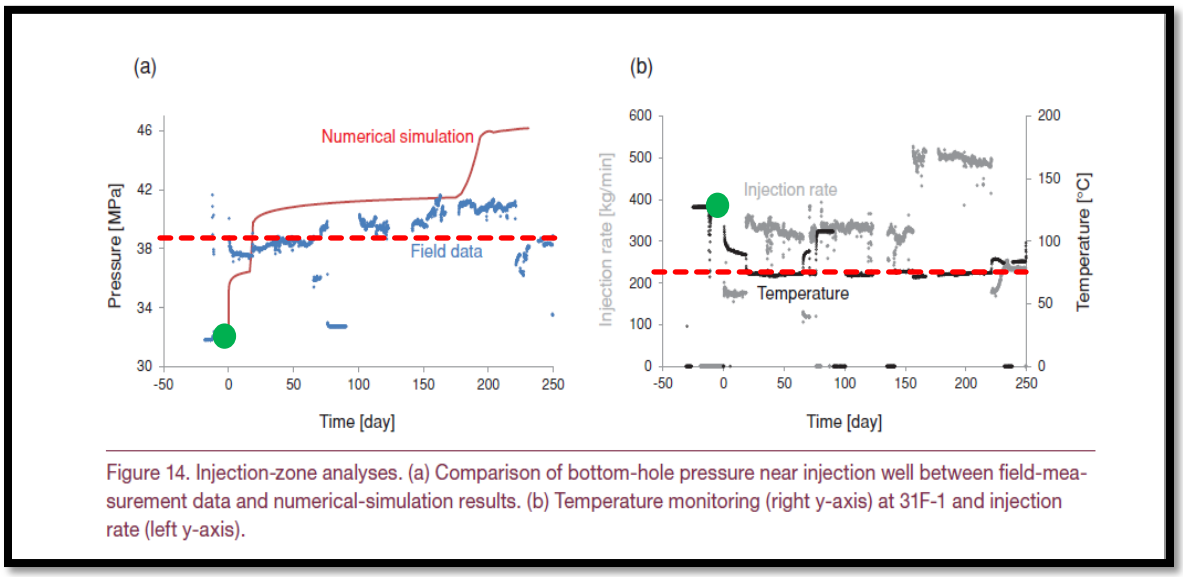

Figure 14. Injection-zone analyses. (a) Comparison of bottom-hole pressure near injection well between field-measurement data and numerical-simulation results. (b) Temperature monitoring (right y-axis) at 31F-1 and injection rate (left y-axis).

Figure 24: Graphs of recorded bottomhole temperature and pressure in a Cranfield CO_2 injection well. The numerical simulation refers to work performed by researchers at the UTBEG. The green dots represent the initial conditions in the reservoir before any injection, and the red dashed lines represent the bottomhole injection conditions used in this thesis.

The graphical data show hardly any pressure increase (BHP stays around 38 MPa) when the injection rate was nearly doubled from 175 kg/min to 330 kg/min (after 20 days). This indicates a fracture must have formed and grew with the increase in injection rate, at about 38 MPa propagation pressure. When the injection rate was stepped up again to 500 kg/min (at 150 days), the BHP rises only to about 41MPa and levels off– again indicating the presence of a fracture. The induced fracture would have most likely grown rapidly with this large jump in injection rate, and per the model stated, would lengthen to the point where the pressure at the tip is equal to the thermoelastically modified minimum horizontal stress.

Developing the Analytical Solution for the Fracture Equilibrium Equation and Injection Rate Equation (Equations 26, 27 & 28)

The analytical solutions for fracture equilibrium length and injection rate were derived from a 3-bin approximation of a fracture of constant width in a reservoir with the same boundary, pressure, and geometry conditions as those used in this thesis. Fluid flow was assumed to be one dimensional and steady state. The unknowns of the problem were then fracture length, injection rate (in m^2/s in this solution), and a dummy variable P_2. The result was a system of three equations, whereby the quadratic equation to evaluate P_2 must be solved first, then the equation for fracture length, and then the equation for injection rate.

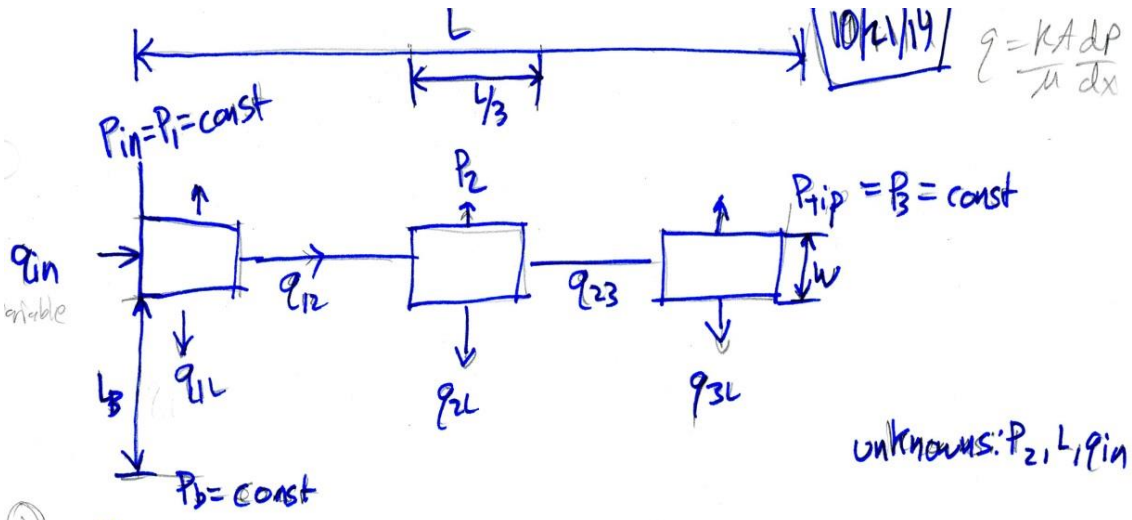

10/21/14

$q = \frac{KA}{\mu}\frac{dP}{dx}$

unknowns: P_2, L, q_{in}

(1) $q_{in} = 2q_{1L} + q_{12} = 2\frac{L}{3}\cdot h\frac{(P_1-P_b)}{L_B}\cdot\frac{K_m}{\mu_m} + w\cdot h\frac{(P_1-P_2)}{L/3}\frac{K_f}{\mu_f}$

(2) $q_{12} = 2q_{2L} + q_{23} = 2\frac{L}{3}h\frac{(P_2-P_b)}{L_B}\cdot\frac{K_m}{\mu_m} + wh\frac{(P_2-P_3)}{L/3}\frac{K_f}{\mu_f}$

(3) $q_{23} = q_{3L} = 2\frac{L}{3}h\frac{(P_3-P_B)}{L_B}\cdot\frac{K_m}{\mu_m}$

7

$$q_{11} = \frac{2Lh}{3}\frac{(P_1-P_B)}{L_B}\cdot\frac{K_m}{\mu_m} + \frac{wh(P_1-P_2)}{L/3}\cdot\frac{K_f}{\mu_f}$$

$$q_{12} = \frac{2Lh}{3}\frac{(P_2-P_B)}{L_B}\frac{K_m}{\mu_m} + \frac{wh(P_2-P_3)}{L/3}\frac{K_f}{\mu_f}$$

$$q_{23} = \frac{2Lh}{3}\frac{(P_3-P_B)}{L_B}\frac{K_m}{\mu_m}$$

$$\frac{wh(P_1-P_2)}{L/3}\frac{K_f}{\mu_f} = \frac{2Lh}{3}\frac{(P_2-P_B)}{L_B}\frac{K_m}{\mu_m} + \frac{wh(P_2-P_3)}{L/3}\frac{K_f}{\mu_f}$$

$$\frac{wh(P_2-P_3)}{L/3}\frac{K_f}{\mu_f} = \frac{2Lh}{3}\frac{(P_3-P_B)}{L_B}\frac{K_m}{\mu_m}$$

$$3wh(P_2-P_3)\frac{K_f}{\mu_f} = \frac{2hL^2}{3}\frac{(P_3-P_B)}{L_B}\frac{K_m}{\mu_m} \Rightarrow L^2 = 9w\frac{(P_2-P_3)}{(P_3-P_B)}\frac{K_f}{\mu_f}\cdot\frac{\mu_m}{K_m}\frac{L_B}{2}$$

$$3w(P_1-P_2)\frac{K_f}{\mu_f} = \frac{2L^2}{3}\frac{(P_2-P_B)}{L_B}\frac{K_m}{\mu_m} + 3w(P_2-P_3)\frac{K_f}{\mu_f}$$

$$\frac{9w}{2}\frac{K_f}{\mu_f}\left[(P_1-P_2)-(P_2-P_3)\right] = L^2\frac{(P_2-P_B)}{L_B}\frac{K_m}{\mu_m} \Rightarrow \frac{9L_Bw}{2}\frac{K_f}{\mu_f}\frac{\mu_m}{K_m}\frac{\left[(P_1-P_2)-(P_2-P_3)\right]}{P_2-P_B} = L^2$$

2

$$L^2 = \frac{q_{LBw}}{2}\left(\frac{P_2-P_3}{P_3-P_B}\right)\frac{K_f}{\mu_f}\cdot\frac{\mu_m}{K_m}$$

$$L^2 = \frac{q_{LBw}}{2}\frac{K_f}{\mu_f}\frac{\mu_m}{K_m}\frac{\left[(P_1-P_2)-(P_2-P_3)\right]}{P_2-P_B}$$

$$\frac{P_2-P_3}{P_3-P_B} = \frac{(P_1-P_2)-(P_2-P_3)}{P_2-P_B} \Rightarrow (P_2-P_3)(P_2-P_B) = \underbrace{\left[(P_1-P_2)-(P_2-P_3)\right]}_{P_1-2P_2+P_3}(P_3-P_B)$$

$$P_2^2 - P_3P_2 + P_3P_B - P_BP_2 = P_1P_3 - 2P_2P_3 + P_3^2 - P_1P_B + 2P_2P_B - P_3P_B$$

$$P_2^2 = P_1P_3 - P_2P_3 + P_3^2 - P_1P_B + 3P_2P_B - 2P_3P_B$$

$$P_2^2 + P_3P_2 - 3P_BP_2 = P_1P_3 + P_3^2 - P_1P_B - 2P_3P_B$$

$$P_2^2 + (P_3 - 3P_B)P_2 - (P_1P_3 + P_3^2 - P_1P_B - 2P_3P_B) = 0$$

$$X = \frac{-B \pm \sqrt{B^2-4AC}}{2A}$$

$$\dot{m}_{inj} = \frac{1}{2}\left[\frac{2L}{3L_B}(P_1-P_B)\frac{K_m}{\mu_m} + \frac{3w(P_1-P_2)}{L}\frac{K_f}{\mu_f}\right]$$

3

Bibliography

1. Aschehoug, M., and C. S. Kabir. "Real-time Evaluation of Carbon Dioxide Production and Sequestration in a Gas Field." *SPE Reservoir Evaluation & Engineering* May (2013): 134-43. Print.
2. Bachu, Stefan. "Screening and Ranking of Sedimentary Basins for Sequestration of CO2 in Geological Media in Response to Climate Change." *Environmental Geology* 44 (2003): 277-89. Print.
3. Bear, J. *Hydraulics of Groundwater*. New York: McGraw-Hill, 1979. Print.
4. Beavers, Gordon S., and Daniel D. Joseph. "Boundary Conditions at a Naturally Permeable Wall." *Journal of Fluid Mechanics* 30 (1967): 197-207. Print.
5. Blanton, T. L., and J. E. Olson. "Stress Magnitudes from Logs: Effects of Tectonic Strains and Temperature." *SPE Reservoir Evaluation & Engineering* 2.1 (1999): 62-68. Print.
6. Bock, Bert, et al. *Economic Evaluation of CO2 Storage and Sink Enhancement Options*. TVA Public Power Institute, 2003. Print.
7. Cheng, Ping. *Heat Transfer in Geothermal Systems*. Academic Press, Inc., 1978. Print. Vol. 14 of *Advances in Heat Transfer*.
8. Clean Air Task Force. *The Carbon Capture and Storage Imperative*. By John Thompson et al. Boston. 2010. Print.
9. Clifford, P. J., P. J. Berry, and Hongren Gu. "Modeling the Vertical Confinement of Injection-Well Thermal Fractures." *SPE Production Engineering* Nov (1991): 377-83. Print.
10. Crouch, S.L., and A.M. Starfield. *Boundary Element Methods in Solid Mechanics*. N.p.: George Allen & Unwin, 1983. Print.
11. Detienne, J. L., et al. "Thermally Induced Fractures: A Field-Proven Analytical Model." *SPE Reservoir Evaluation and Engineering* Feb (1998): 30-35. Print.
12. Detournay, Emmanuel, and Alexander H.D. Cheng. "Fundamentals of Poroelasticity." Chapter 5. *Analysis and Design Method*. N.p., 1193. 113-71. Print. Vol. II of *Comprehensive Rock Engineering: Principles, Practice and Projects*.
13. Economides, Michael, and Kenneth Nolte. *Reservoir Stimulation*. 3rd ed. Wiley, 2009. Print.
14. Ettehadtavakkol, Amin, Larry W. Lake, and Steven L. Bryant. "CO2-EOR and Storage Design Optimization." *International Journal of Greenhouse Gas Control* 25 (2014): 79-92. Print.
15. Gidley, J.L., et al. *Recent Advances in Hydraulic Fracturing*. 1990. Print. SPE Monograph 12.
16. Gringarten, A.C., H.J. Ramey, and R. Raghavan. "Unsteady-state Pressure Distributions Created by a Well with a Single Infinite-Conductivity Fracture." *SPE Journal* August (1974): 347-60. Print.

17. Haimson, Bezalel, and Charles Fairhurst. "Initiation and Extension of Hydraulic Fracturs in Rocks." *SPE Third Conference on Rock Mechanics* (1967): 310-18. Print.
18. Hasan, A.R., and C.S. Kabir. "Aspects of Wellbore Heat Transfer during Two-phase Flow." *SPE Production & Facilities* Aug. 1994: 211-16. Print.
19. Howard, George C., C.R. Fast, and R.D. Carter. "Optimum Fluid Characteristics for Fracture Extension." *Drilling and Production Practices* API ser. (1957): 261-70. Print.
20. Hustedt, B., et al. "Induced Fracturing in Reservoir Simulations: Application of a New Coupled Simulator to Waterflooding Field Examples." *SPE ATCE* (2006): n. pag. Print.
21. Iverson, William. "Log-Derived Stress in Anisotropic Formations." *The Log Analyst* Sept. 1996: 33-40. Print.
22. Kamal, Medhat M., comp. *Transient Well Testing*. 2009. Print. SPE Monograph Ser. 23.
23. Katahara, Keith. "Estimation of In-situ Stress Profiles from Well-Logs." *SPWLA 37th Annual Logging Symposium* (1996). Print.
24. Kim, Seunghee, and Seyyed Abolfazl Hosseini. "Above-zone Pressure Monitoring and Geomechanical Analyses for a Field-scale CO2 Injection Project in Cranfield, MS." *Greenhouse Gases Science and Technology* (2013): 81-98. Print.
25. Kovscek, A. R. "Screening Criteria for CO2 Storage in Oil Reservoirs." *Petroleum Science and Technology* 20 (2007): 841-66. Print.
26. Luo, Zhiyuan, and Steven Bryant. "Influence of Thermo-Elastic Stress on CO2 Injection Induced Fractures During Storage." *SPE International Conference on CO2 Capture, Storage and Utilization* (2010): n. pag. Print.
27. Mayerhofer, M. J., and M. J. Economides. "Fracture-Injection-Test Interpretation: Leakoff Coefficient vs. Permeability." *SPE Production & Facilities* Nov. 1997: 231-36. Print.
28. Michael, K., et al. "Geological Storage of CO_2 in Saline Aquifers- A Review of the Experience from Existing Storage Operations." *IJGGC*: n. pag. Print.
29. Morales, R. H., et al. "Detection of a Formation Fracture in a Waterflooding Experiment." *Journal of Petroleum Technology* Oct. (1986): 1113-21. Print.
30. Nordgren, R. P. "Propagation of a Vertical Hydraulic Fracture." *Society of Petroleum Engineers Journal* 253 (1972): 306-14. Print.
31. Oreskes, Naomi. "The Scientific Consensus on Climate Change." *Science* 3 Dec. 2004: 1686. Print.
32. Parkhurst, David L., and C.A.J. Appelo. "User's Guide to PHREEQC (Version 2)--A Computer Program for Speciation, Batch-Reaction, One-Dimensional Transport, and Inverse Geochemical Calculations." *USGS PHREEQC V.3*. United States Geological Survey. Web. 10 May 2014. <http://wwwbrr.cr.usgs.gov/projects/GWC_coupled/phreeqc/html/final.html>.

33. Perkins, T. K., and J. A. Gonzalez. "The Effect of Thermoelastic Stresses on Injection Well Fracturing." *Society of Petroleum Engineers Journal* (1985): 78-88. Print.
34. Perkins, T. K., and L. R. Kern. "Widths of Hydraulic Fractures." *Journal of Petroleum Technology* Sept (1961): 937-49. Print.
35. Pollack, Henry, Suzanne Hurter, and Jeffrey Johnson. "Heat Flow from the Earth's Interior: Analysis of the Global Data Set." *Reviews of Geophysics* 31.3 (1993): 267-80. Print.
36. Prats, M. "Effect of Vertical Fractures on Reservoir Behavior- Incompressible Fluid Case." *Society of Petroleum Engineers Journal* June (1961): 105-17. Print.
37. Ribeiro, Lionel H., and Mukul M. Sharma. "A New Three-Dimensional Compositional Model for Hydraulic Fracturing with Energized Fluids." *SPE ATCE* (2012). Print.
38. Rose, S.C., J.F. Buckwalter, and R.J. Woodhall. *The Design Aspects of Waterflooding*. Vol. 11. SPE, 1989. Print. Monograph Ser.
39. Saripalli, K. Prasad, Steven Bryant, and Mukul Sharma. "Role of Fracture Face and Formation Plugging in Injection Well Fracturing and Injectivity Decline." *SPE/EPA Exploration and Production Conference* (1999). Print.
40. Settari, A. "Simulation of Hydraulic Fracturing Process." *Society of Petroleum Engineers Journal* Dec. (1980): 487-500. Print.
41. Settari, A., and G. M. Warren. "Simulation and Field Analysis of Waterflood Induced Fracturing." *SPE/ISRM Rock Mechanics in Petroleum Engineering* (1994): 435-45. Print.
42. Smith, M. B., et al. "High-Permeability Fracturing: 'Carter' Fluid Loss of Not." *SPE International Symposium and Exhibition on Formation Damage Control* (2004). Print.
43. Sneddon, I. N., and M. Lowengrub. *Crack Problems in the Classical Theory of Elasticity*. New York: John Wiley & Sons, 1969. Print.
44. Sneddon, I.N. "The Distribution of Stress in the Neighbourhood of a Crack in an Elastic Solid." *Proceedings of the Royal Society of London* (1946): 229-60. Print.
45. Somerton, W. H., and G. D. Boozer. "Thermal Characteristics of Porous Rocks at Elevated Temperatures." *Journal of Petroleum Technology* June (1960): 77-81. Print.
46. Somerton, Wilbur H. "Some Thermal Characteristics of Porous Rocks." *Petroleum Transactions, AIME* (1958): 375-78. Print.
47. Suri, Ajay, Mukul M. Sharma, and Ekwere J. Peters. "Estimates of Fracture Lengths and Injection Profile in an Injection Well by History Matching Bottom Hole Pressures." Proc. of SPE Western Regional Meeting, May 2010, Anaheim, CA, USA. Print.
48. Svendsen, A. P., et al. "Thermally Induced Fracturing of Ula Water Injectors." *SPE Production Engineering* Nov (1991): 384-90. Print.
49. *University of Texas Well Injectivity Decline Simulator*. The University of Texas, 2009. Print. Vol. 7.1 of *Guide to Using UTWID*.

50. Valko, P., and M. Economides. "Fluid Leak-off Delineation in High-permeability Fracturing." *SPE Production Operations Symposium* Oklahoma City, Oklahoma ser. (1997). Print.
51. Van den Hoek, P.J. "A Simple and Accurate Description of Non-linear Fluid Leak-off in High-Permeability Fracturing." *SPE Annual Technical Conference and Exhibition* (2000). Print.
52. Van den Hoek, P.J., et al. "Simulation of Produced Water Reinjection under Fracturing Conditions." *SPE European Petroleum Conference* (1996): 269-83. Print.
53. Van Oort, Eric, and Richard Vargo. "Improving Formation-Strength Tests and Their Interpretation." *SPE Drilling & Completion* (2008): 284-94. Print.
54. Zoback, Mark D. *Reservoir Geomechanics*. N.p.: Cambridge University Press, 2010. Print.